KfK 3346
März 1983

LWR Fuel Rod Behavior in the FR2 In-pile Tests Simulating the Heatup Phase of a LOCA

Final Report

E. H. Karb, M. Prüßmann, L. Sepold, P. Hofmann, G. Schanz
Hauptabteilung Ingenieurtechnik
Institut für Material- und Festkörperforschung
Projekt Nukleare Sicherheit

Kernforschungszentrum Karlsruhe

K E R N F O R S C H U N G S Z E N T R U M K A R L S R U H E

HAUPTABTEILUNG INGENIEURTECHNIK
INSTITUT FÜR MATERIAL- UND FESTKÖRPERFORSCHUNG
PROJEKT NUKLEARE SICHERHEIT

KfK 3346

LWR Fuel Rod Behavior in the FR2 In-pile Tests Simulating the Heatup Phase of a LOCA

(Final Report)

E.H. Karb
M. Prüßmann
L. Sepold
P. Hofmann
G. Schanz

Kernforschungszentrum Karlsruhe GmbH., Karlsruhe

Kernforschungszentrum Karlsruhe GmbH
ISSN 0303-4003

Abstract

This is the final report on the results of the FR2 In-pile Experiments on LWR (Light Water Reactor) fuel rod behavior. The tests were to investigate the possible influence of a nuclear environment on fuel rod failure mechanisms. Unirradiated and irradiated (2,500 to 35,000 MWd/t_U) PWR-type test fuel rods as well as electrically heated fuel rod simulators were exposed to temperature transients simulating the second heatup phase of a LOCA (Loss-of-Coolant Accident). Rod internal overpressure combined with elevated cladding temperatures caused the rod claddings to balloon and rupture. The burst data (burst temperature, burst pressure, and burst strain) of the nuclear test rods did not indicate differences from results obtained with electrically heated fuel rod simulators, and did not show an influence of burnup.

The fuel pellets in previously irradiated rods, already cracked during normal reactor operation, fragmented after having lost their radial support by the cladding when this deformed radially. In the ballooned region the fuel particle dislocation usually led to a complete loss of pellet shape. Consequently, fuel particle movement into the ballooned region from sections above resulted in significant reductions of the pellet stack height. The fuel pellet fragmentation and the particle dislocation, however, did not affect the cladding deformation process during the relatively fast transients investigated in this program.

From the test results and the evaluation of the posttest examaninations it is concluded that there is no influence of a nuclear environment on the fuel rod failure mechanisms during a LOCA. Thus, results on the cladding behavior during LOCA conditions obtained with electrically heated fuel rod simulators may be considered representative of the behavior of real fuel rods.

LWR-Brennstabverhalten in der Aufheizphase eines LOCA, Ergebnisse aus den FR2-In-pile-Versuchen (Abschlußbericht)

Zusammenfassung

Diese Veröffentlichung stellt den Abschlußbericht über die Ergebnisse der FR2-In-pile-Experimente zum LWR (Leichtwasserreaktor) - Brennstabverhalten dar. Die Versuche sollten zeigen, ob es einen Einfluß der nuklearen Einflußgrößen auf die Mechanismen des Brennstabversagens gibt. Zu diesem Zweck wurden unbestrahlte und bestrahlte (2500 bis 35000 MWd/t_u) Versuchsstäbe ebenso wie elektrisch beheizte Brennstabsimulatoren Temperaturtransienten ausgesetzt, wie sie in der sog. zweiten Aufheizphase eines LOCA (Loss-of-Coolant Accident) als denkbar angesehen werden. Der innere Überdruck der Stäbe im Zusammenspiel mit den erhöhten Stabtemperaturen während der Aufheizung führten zum Aufblähen der Hüllrohre (Ballooning) und zum Bersten.

Die Berstdaten, wie Bersttemperatur, Berstdruck und Berstdehnung, ergaben keine Unterschiede zwischen den Ergebnissen aus Versuchen mit echten Nuklearstäben und denen mit elektrisch beheizten Brennstabsimulatoren. Auch zeigten sie keinen Einfluß des Abbrandes.

Die Brennstofftabletten der vorbestrahlten Stäbe, die während der Vorbestrahlung (Normalbetrieb) in üblicher Weise gerissen waren, zerfielen nach der radialen Dehnung der Hülle in Bruchstücke, wobei im Bereich großer Hülldeformation die Tablettenstruktur meist verloren ging. Durch Nachrutschen von Brennstoffteilchen aus den darüberliegenden Stababschnitten ergab sich dabei eine z.T. deutliche Verkürzung der Brennstoffsäule. Diese Brennstoffumverteilung hatte bei den relativ schnellen LOCA-Transienten keinen Einfluß auf den Deformationsvorgang.

Im Hinblick auf die Zielsetzung kann zusammenfassend der Schluß gezogen werden, daß ein Einfluß der nuklearen Bedingungen auf die Mechanismen des Brennstabversagens beim LOCA nicht zu erwarten ist. Damit können Versuche mit elektrisch beheizten Brennstabsimulatoren als repräsentativ für Nuklearstabtests unter LOCA-Bedingungen angesehen werden.

Contents

Figures

Page

Tables

1. Introduction

Fuel rod behavior during a loss-of-coolant accident (LOCA) in a light-water reactor (LWR) after a break of a main coolant line has been the subject of extensive analytical and experimental research because of its potential to reduce the effectiveness of the emergency core cooling by fuel rod deformation.

Most of the experiments have been performed out-of-pile with electrically heated fuel rod simulators /1,2,3,4/. However, since some parameters cannot be simulated adequately out-of-pile, experiments in a nuclear environment have been necessary.

Therefore, an in-pile experimental program was performed as part of the Nuclear Safety Project's Fuel Behavior Program at the Kernforschungszentrum Karlsruhe (KfK), Federal Republic of Germany /5,6/. In a test loop of the FR2 research reactor unirradiated as well as irradiated single fuel rod samples, and some electrically heated fuel rod simulators were exposed to transients simulating the second heatup phase of a LOCA in a pressurized-water reactor (PWR) after a double ended break of a main coolant inlet line. In the course of this reference accident the second heatup phase has the highest probability of fuel failure because of the relatively long time the cladding is at high temperature while the internal overpressure causes elevated cladding stresses.

This paper as a final report, after a brief description of experimental program, hardware, and procedures, gives the results of the transient tests, of the posttest examinations, and of the posttest calculations, and summarizes the results of the program. Finally, conclusions with respect to the test objectives are drawn and discussed.

2. Objectives and test program

The objectives of the FR2 in-pile tests /6,8-11/ were

- to provide qualitative and quantitative information on possible effects of a nuclear environment on the mechanisms of fuel rod failure

under LOCA conditions already known from out-of-pile tests with electrically heated fuel rod simulators, and

- to identifiy possible additional failure mechanisms.

The nuclear environment is primarily characterized by the heat generation in UO_2 fuel and the energy transfer from the fuel to the cladding depending on the condition of the fuel. Consequently, burnup was selected the main parameter of the test program. Table 1 shows, that after two test series (A and B) with unirradiated rods, the majority of the tests (series C to G 2/3) was performed with rods previously irradiated to burnup values ranging from 2,500 to 35,000 MWd/t_u. As a second parameter, rod internal pressure was varied between 25 and 125 bars at steady state temperature. This pressure range was chosen larger than that expected during the lifetimes of PWR rods. Heatup rates varied between 6 and 20 K/s. Eight reference tests with electrically heated rod simulators (series BSS) were conducted in the in-pile loop unter conditions identical with those of the nuclear tests.

Table 1: Test matrix of the FR2 in-pile tests on fuel rod behavior

Type of Tests	Test Series	Number of Rods Irradiated	Number of Tests	Target Burnup (MWd/t_u)	Range of Internal Pressure at Steady State Temperature (bar)
Calibration, Scoping	A	—	5	—	25-100
Unirradiated Rods (Main Parameter: Internal Pressure)	B	—	9	0	55-90
Irradiated Rods (Main Parameter: Burnup)	C	6	5	2500	25-110
	E	6	5	8000	25-120
	F	6	5	20000	45-85
	G1	6	5	35000	50-90
	G2/3	6	5	35000	60-125
Electrically Heated Fuel Rod Simulators (Main Parameter: Internal Pressure)	BSS	—	8	—	20-110

3. Experiment design and conduct

3.1 Experiment design

The tests were performed in the DK loop of the FR2 research reactor (Fig.1) which provided the desired thermal hydraulic conditions. The loop was originally designed to test steam-cooled fuel rod samples and was operated with superheated steam as coolant /6/. During the steady state phase of the test (see section 3.5), the loop was operated at a pressure of 60 bars, a steam temperature of about 300°C, and a coolant mass flow of 120 kg/h. The loop was particularly suitable for experiments on fuel rod failure (cladding rupture) because it was equipped with condensation and filter systems for retaining fission products and retarding noble gases.

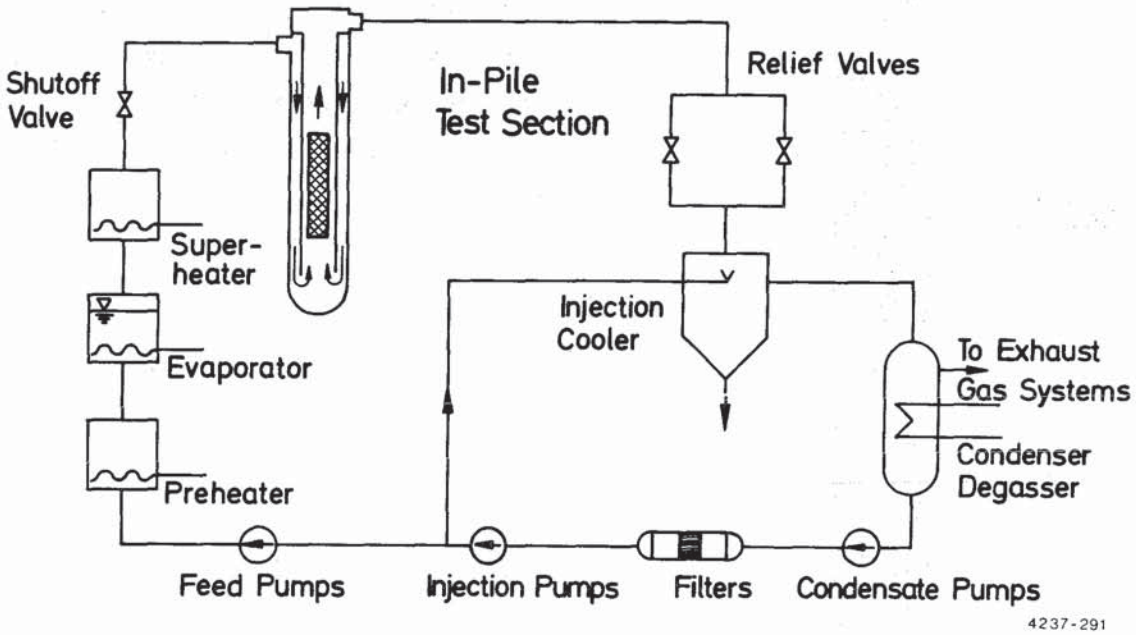

Figure 1: Simplified flow scheme of the DK loop, operated with superheated steam, in the FR2 reactor

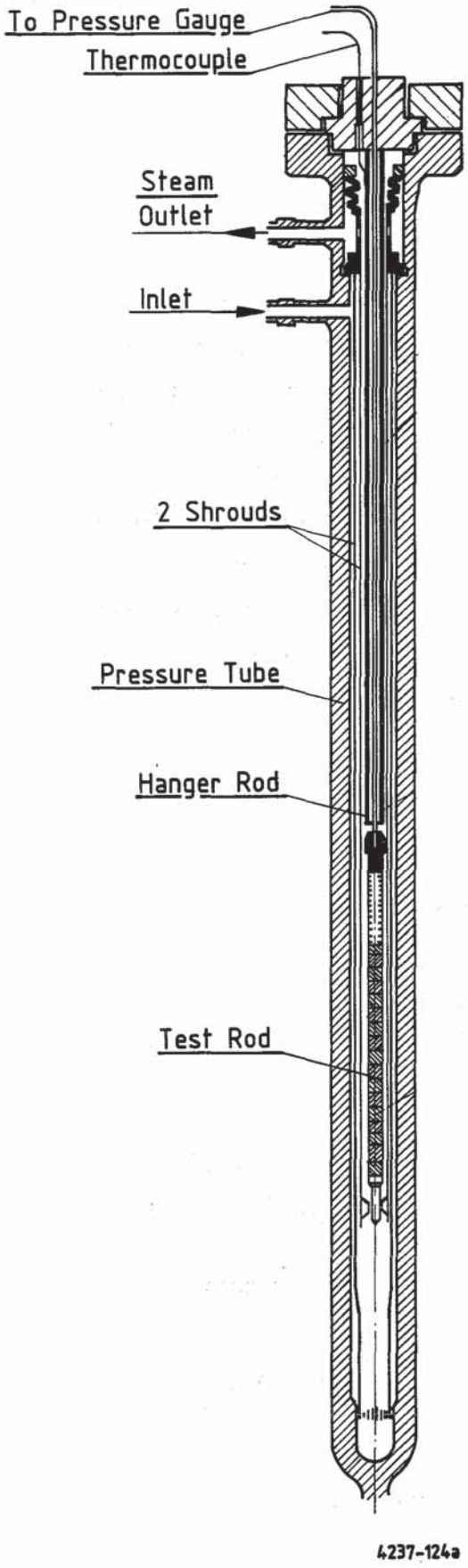

The test specimens were contained in the in-pile test section which comprised several shrouds and a thick-walled pressure tube (Fig.2).

The inlet and outlet connections of the pressure tube to the loop system were both located at the upper end of the test section. The flow reversed its direction at the bottom of the pressure tube and moved up past the test rod. Each test rod was mounted to a hanger rod to provide structural support for the rod and for the test rod instrumentation. For the preirradiated rods the rod assembly and instrumentation were done under remote handling conditions, in the hot cell of the FR2 reactor.

Figure 2: In-pile test section of the DK-loop in the FR2 reactor (simplified)

3.2 Test rod dimensions

The nuclear test rod is illustrated in Fig. 3. Its radial dimensions (Table 2: nominal data) were identical to those of a fuel rod of a German 1300 MW_e PWR. The active fuel length was 50 cm, approximately equal to the axial distance between spacer grids of fuel elements in a reactor. The U-235 enrichment of 4.7% used in the test rod fuel was slightly higher than that of PWR fuel. Two different gap sizes were used for the tests with nuclear rods.

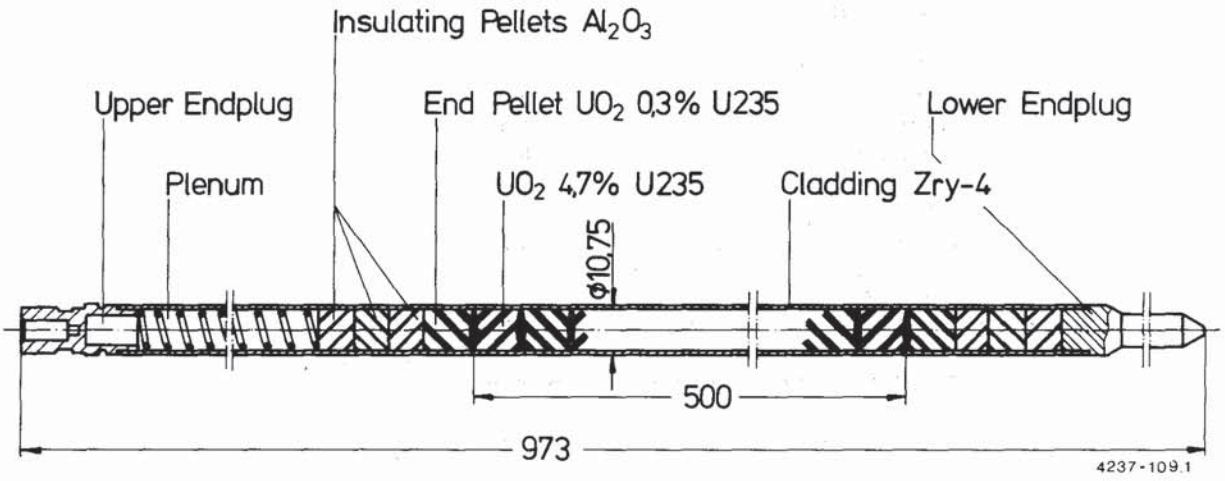

Figure 3: Test fuel rod design

In test series G3 (35000 MWd/t_u burnup) and for comparative reasons in the B3 series (no burnup) the cold diametral gap size of the rods was reduced from nominal 190 to 150 μm in order to compensate for the lack of cladding creep during irradiation in the low coolant pressure environment of the FR2 reactor.

The test rod had only an upper fission gas plenum compared with the two plena of a German PWR rod.

Table 2: Nominal test fuel rod data

Cladding	
Material	Zircaloy-4
Outside diameter, mm	10.75
Inside diameter, mm	9.3
Wall thickness, mm	0.725
Fuel pellets	
Material	UO_2
Diameter (nominal gap), mm	9.11
Diameter (small gap), mm	9.15
Length, mm	11
Enrichment (active zone), %	4.7
Enrichment (end pellets), %	0.3
Height of pellet stack (active zone), mm	500
Density, g/cm³	10.35
Theoretical density, %	94.4
Insulating pellets	
Material	Al_2O_3
Diameter, mm	9.15
Length, mm	8
Void Volumes	
Dishing per pellet, mm³	16
Gap Volume (nominal gap), cm³	1.57
Total plenum volume (incl. pressure transducer), cm³	28.12
Fillgas composition	100 % Helium

The size of the test rod plenum volume, including the internal volume of the pressure measuring system (section 3.3), was chosen to equal the total void volume of both plena in a PWR rod. An analytical comparison of time-dependent cladding deformation of the test fuel rod and a full-length PWR rod, both exposed to the same LOCA transient, showed the best agreement for identical plenum volume sizes.

The characterization of each fuel rod, i.e. cladding and fuel characterization, is provided in Table 8, Appendix A.

During the fabrication of the fuel rods the cladding and fuel dimensions were recorded. In the center region of the active length (150 to 350 mm from the bottom of the active zone) the outside diameter and the wall thickness of the cladding were measured by an ultrasonic technique.

The data were recorded every 18° on the azimuth and in axial planes 15 mm apart. From the measurements of outside diameter and wall thickness the inside diameter was calculated.

In the center region, also the fuel pellet dimensions and density were determined. With the pellet diameter and the cladding inside diameter the actual mean gap size of the individual rod was calculated.

The length of the plenum was measured from X-ray photographs of the assembled fuel rod.

The cladding dimensions of the electrically heated fuel rod simulators were determined in the same way as for the nuclear rods. Cladding dimensions and heated length were indentical to those of the nuclear test rod. The plenum volume of the simulator (25 cm^3) was designed to approximately equal that of the test fuel rod by using a lower plenum and an annulus of about 60 cm above the upper end of the pellet stack as an upper plenum.

The interior of the rod simulator (annular alumina pellets, heater, and insulation) is illustrated in Fig. 4. The basic design of the simulator was adopted from the electrical heater used in the REBEKA test program* /22/. More detailed information on the design of the simulator used in the FR2 in-pile program is provided in /12/.

3.3 Test rod instrumentation

Fuel rod instrumentation was designed to measure cladding temperature and internal pressure.

Cladding surface thermocouples (chromel-alumel, Inconel 600 sheathed, 1mm diameter) were resistance spot-welded to the outer rod surface at six different axial elevations and azimuthal positions. To avoid formation of eutectics between zirconium and components of the TC sheath material at elevated temperatures, a 30 to 35 mm long platinum tube was swaged onto the thermocouple sheath /13/.

---

*REBEKA single rod and bundle out-of-pile experiments performed at KfK.

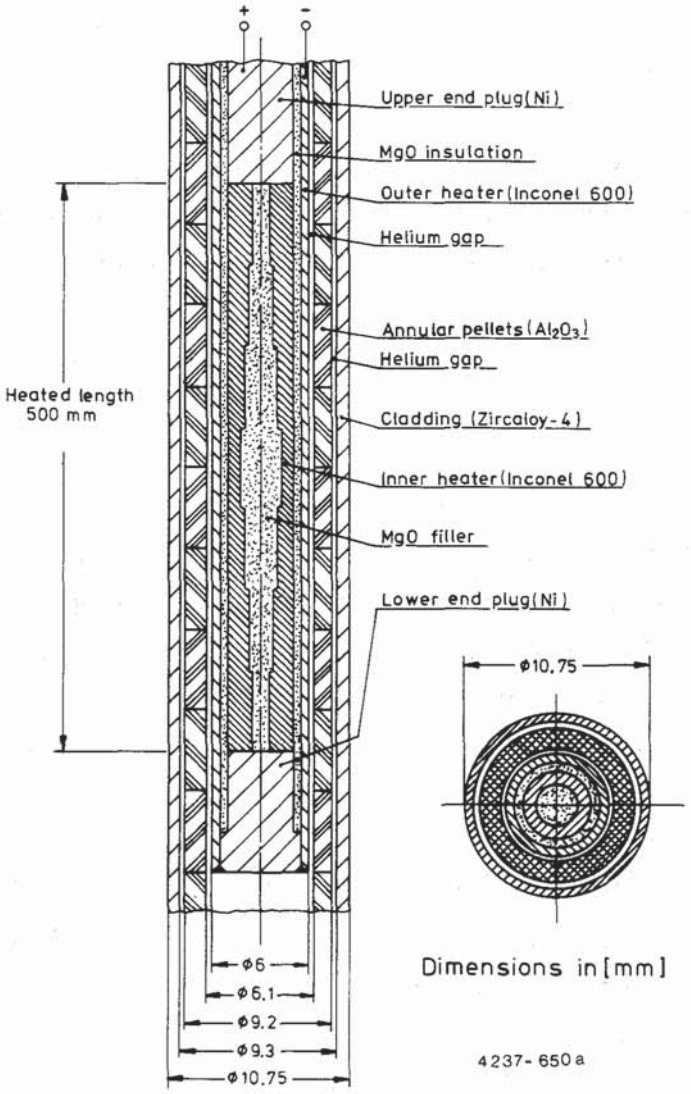

Figure 4: Electrically heated fuel rod simulator design, heated section (not to scale)

In addition, best welding results were accomplished with platinum material. Two different versions of the TC attachment were used, version A and version B (Fig.5).

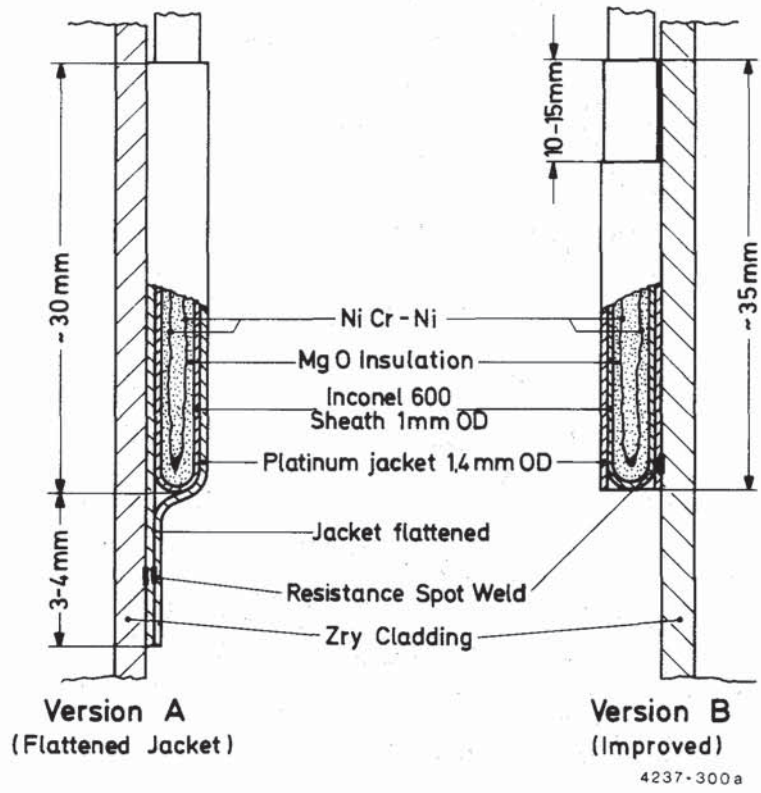

Figure 5: Cladding thermocouple design (schematic)

In general, the surface-mounted TCs show lower temperatures than the real wall temperatures during steady-state and transient operation. The deviations were determined in calibration tests with electrically heated fuel rod simulators without cladding deformation (BSS 5 and 7 for version A and BSS 11 and 14 for version B) by comparing the readings of the clad surface TCs with those of TCs embedded in the cladding. The deviations and the scatter (uncertainty), both resulted to be a function of the rod power rate. The mean values were used as correction for the measured temperatures. Deviation and uncertainty were much smaller for TC version B as compared with version A. At the nominal power of 40 W/cm for the nuclear rods it was 75 ± 35 K for TC version A, and 10 ± 10 K for version B (Fig.6). These correction values had to be added to the TC readings (see also Appendix C).

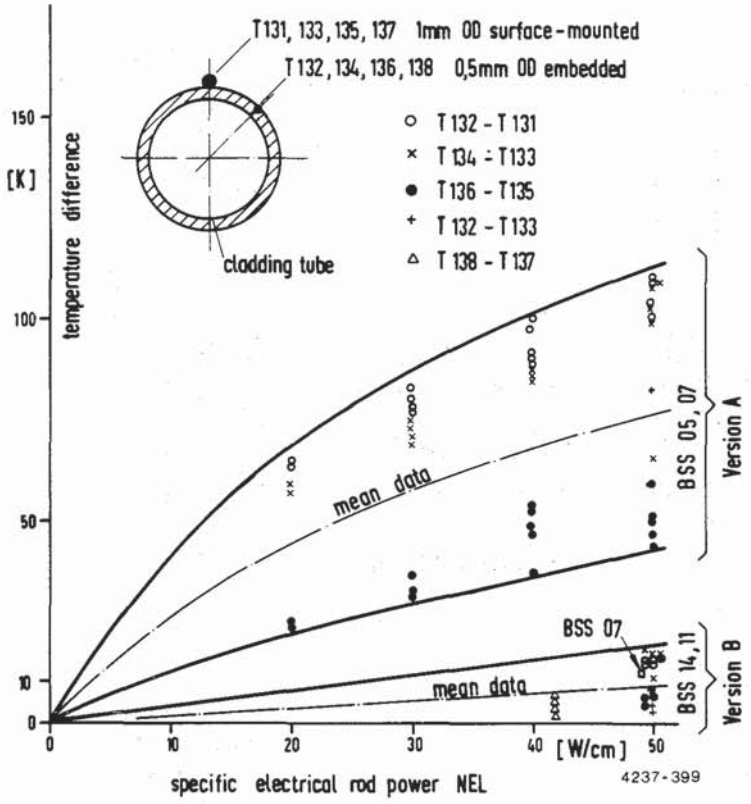

Figure 6: Temperature differences between embedded and surface-mounted TCs vs. rod power during the transient test, obtained by simulator tests without cladding deformation, as a basis for the correction of TC measurements

In addition to the continuous measurement of the cladding temperature an estimation of the local maximum temperature by the investigation of the cladding microstructure (section 6.1) was performed at thermocouple elevations - for the purpose of comparison with the measurements - and at cross sections at the position of maximum circumferential strain in the rupture plane. Also by the microstructural evaluation the azimuthal temperature differences at maximum temperature, especially in the rupture plane, could be determined (section 4.2).

Internal rod pressure was measured dynamically by a strain-gauge type pressure transducer, which was connected to the plenum by a tube approximately 5 m long with an inside diameter of 1.6 mm. This tube was coupled to the test rod plenum in a way that no fission gas produced during the preirradiation could escape from the interior of the rod (see Fig.7).

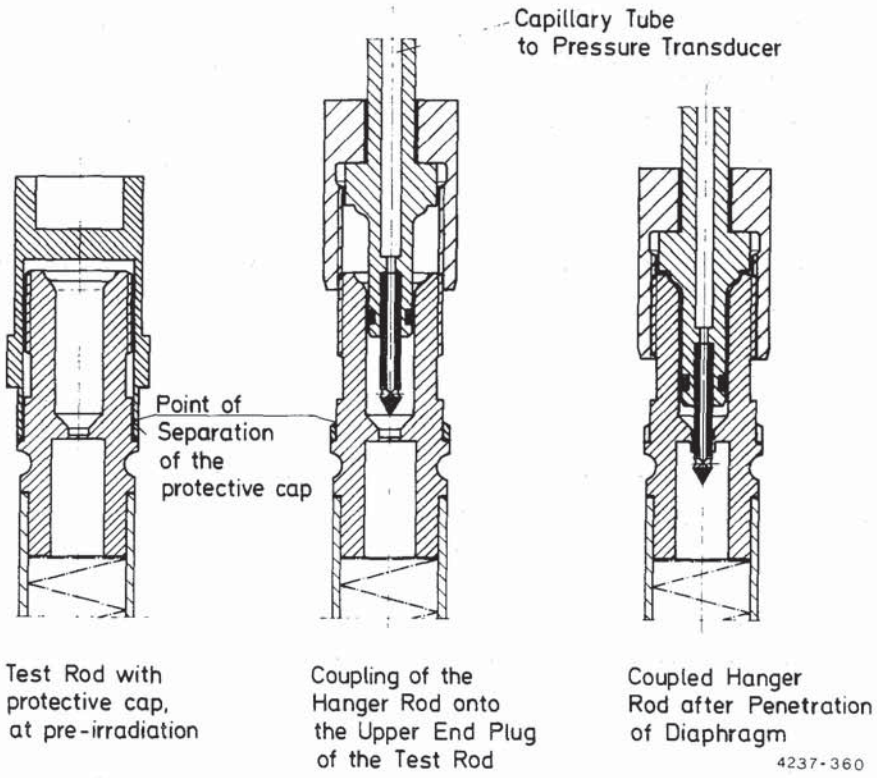

Figure 7: On the measurement of the rod internal pressure and the coupling of the test rod onto the hanger rod under remote control

The signal delay caused by this connecting tube was determined experimentally to be less than 10 ms for rapid depressurization. Dynamic measurement of the internal rod pressure was used for leak detection during steady state operation and indicated the deformation history during the transient, in particular the instant of burst.

The uncertainty is estimated to be about ± 1 bar in the pressure range of 50 to 100 bars (The total range of the pressure transducer was 0 to 175 bar).

3.4 Test rod preirradiation

The nuclear test rods were initially filled with 0.3 MPa helium at room temperature and preirradiated in bundles of six rods in fuel element positions of the FR2 research reactor.

The conditions for the test rod irradiation in the FR2 reactor are listed in Table 3 and compared with average values of a commercial PWR. Coolant pressure and coolant temperature were lower in the FR2 reactor.

Table 3: Irradiation conditions of the test rods in FR2 and of PWR rods in a commercial reactor

		Test rod in FR2	PWR rod
Coolant inlet temperature	(°C)	60	290
Coolant pressure	(bar)	2,4	155
Linear rod power	(W/cm)	200-450	200-450
Initial rod pressure (cold)	(bar)	3	22.5

This resulted in lower cladding temperature and lower fuel surface temperatures of the test rods in the FR2 reactor compared with a PWR rod. Fuel centerline temperature of the test rod was almost as high as in a PWR rod. No creep of the cladding toward the fuel due to external overpressure did occur in the FR2 test rods. There were more scrams and shutdowns in the FR2 research reactor than in a commercial PWR.

After each FR2 operation cycle of about 40 days there was a shutdown of 10 to 15 days. During the period of shutdown the positions of a number of fuel elements were changed in the FR2 core. A typical operation history is given with Fig. 8 for test series F, showing the FR2 operation cycles but no shutdowns. The irradiation histories of all test series are listed in Table 9, Appendix A, including the total number of shutdowns (planned and unscheduled).

Inspite of the differences in the irradiation conditions between the test rod in the FR2 reactor and a PWR rod, the typicality of the test fuel rods is believed to be sufficient. This was confirmed by visual comparisons of fuel crack patterns (section 5.1).

After irradiation, five rods of each bundle were instrumented for transient testing and the remaining rod was reserved for the radiochemical burnup analysis, the fission gas analysis (section 7.2), and the investigation of the post-irradiation fuel condition (see section 5).

The burnup of the test rods was determined by (a) the thermal balance during the reactor operation and (b) by the radiochemical analysis.

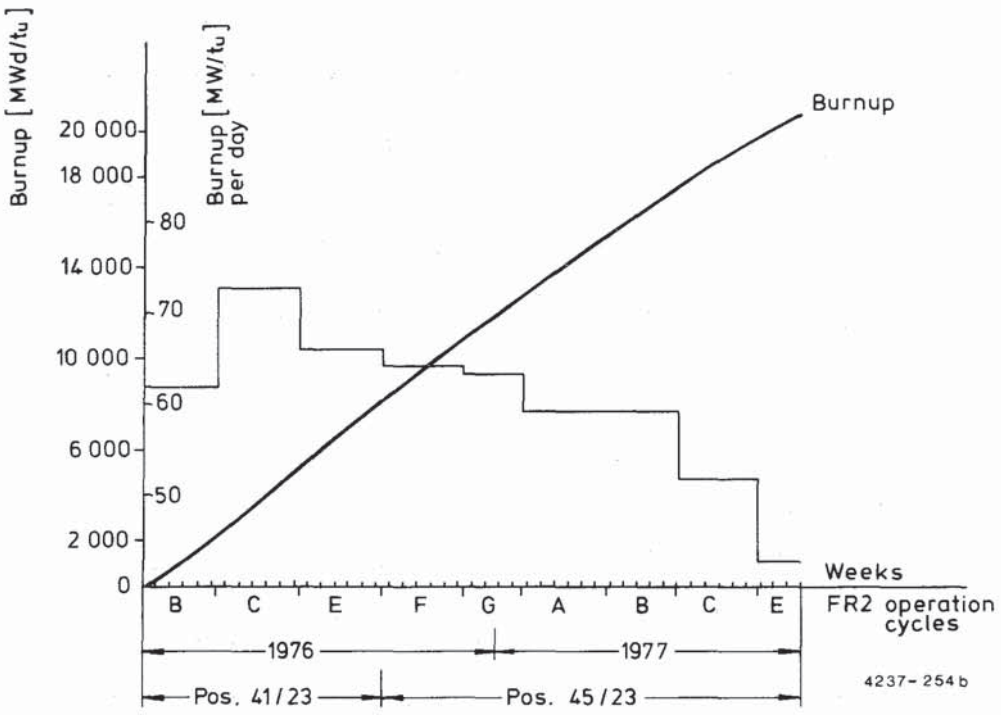

Figure 8: Preirradiation history of test series F, burnup 20000 MWd/t_u

The axial burnup profiles determined from the radiochemical samples of test series C, E, F, G1, and G2/3 are given in Fig. 9, the average data are listed in Table 4 for both methods of burnup determination.

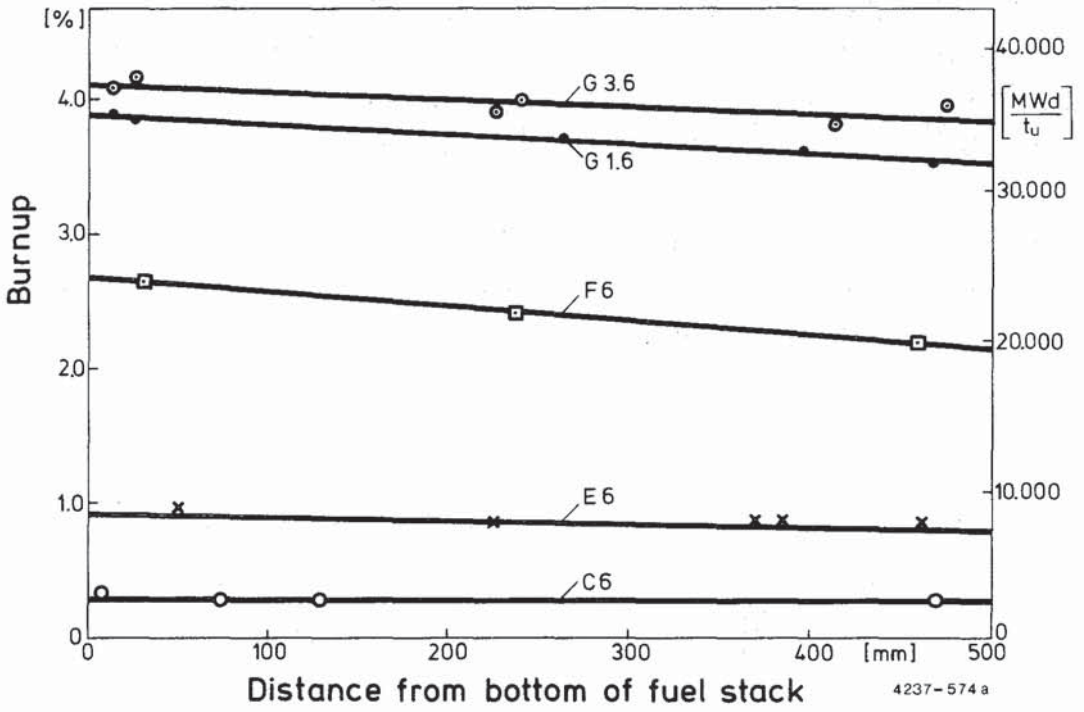

Figure 9: Axial burnup profiles of the preirradiated rods

The visual inspection within the post-irradiation examination of the test rods did not reveal any damages or rod bending. Thus, the test rods were appropriate for uses in the subsequent LOCA transient tests.

Table 4: Burnups achieved by irradiation in the FR2 reactor

Test series	Burnup from thermal balance (MWd/t_u)	Burnup from radiochemical analysis[a),b)] (at-%)	(MWd/t_u)
C	2400	0,28	2560
E	7900	0,88	8000
F	20650	2,4	21910
G1	36000	3,7	33780
G2/3	34000	4,0	36520

a) axial average
b) 1 at-% ≙ 9130 MWd/t_u

3.5 Experiment conduct

Each test began with a steady state phase, during which the rod was pressurized to the desired level at steady state temperature by adding helium to the fission gas generated during preirradiation. Also during this phase instrumentation calibration, rod power determination, and axial flux profile measurements were performed. The test rod was then exposed to a standard temperature history derived from licensing calculations for a PWR fuel rod during a LOCA (a double-ended break of the cold leg pipe). The transient in the test loop was initiated by interruption of the loop coolant flow and system depressurization. This was done by rapidly closing the coolant shutoff valve and simultaneously opening a relief valve with a large cross section downstream of the test section (Fig.1).

The coolant flow rate past the test rod decreased to zero and the system pressure to approx. 0.1 bar within 8 to 10 s. During the subsequent heatup phase, the test rod power was kept constant until the target cladding temperature of approximately 1200 K was reached. At that temperature, the rod power was rapidly reduced by reactor scram. After the turnaround point as the result of the reactor scram, when the cladding temperature had decreased to approx. 1000 K, the steam inlet valve ("shutoff valve") was opened again, the coolant mass flow reactivated and a quenching effect took place. In the tests which were run without quenching (C1 through C4, F4, G1.2 through G1.4 and all tests of series G2/3) the rod temperature continued to drop as it had started from the turnaround point until the coolant temperature level was reached. A schematic representation of the test procedure is given in Fig. 10. Depending on the linear rod power rate the heatup phase lasted in most cases between 50 and 100 seconds, and with the exception of the first 8 to 10 seconds, the cladding outer surface was exposed to an atmosphere of stagnant superheated steam with a rather low density (pressure 0,1 bar).

To increase the steam supply for possible cladding oxidation, three of the tests with nuclear rods (B 1.6, B 3.1, B 3.2) were performed with an additional steam flow past the test rod during the transient after the isolation of the in-pile test section from the steam generating components by the shutoff valves (Fig.1).

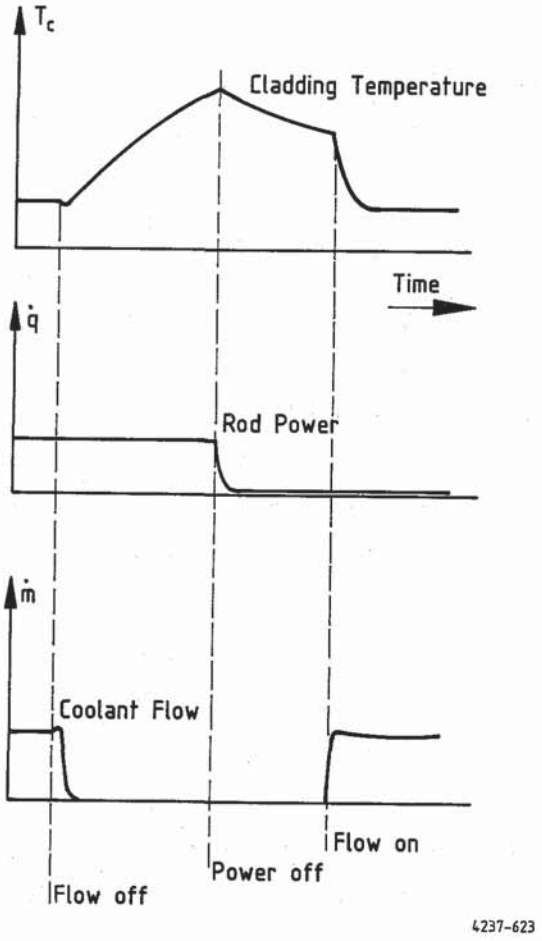

Figure 10: Test procedure, schematic

This was accomplished by bypassing the shutoff valve with a small tube from the start of the transient until the quenching. The mass flow through the bypass was 0.3 to 0.5 kg/h. As this flow had a pronounced influence on the cladding heatup rate during the first 10 to 20 seconds of the transient, the operation of the bypass was discontinued for further tests. The additional steam supply did not lead to higher oxygen uptake of the rods compared to the remainder of the specimens (see section 6.2).

Cladding deformation and burst were monitored during each test by means of the cladding temperature and internal rod pressure traces. Typical traces are illustrated in Fig. 11. The six cladding thermocouples (designated 131 through 136) located at six different axial positions showed little difference, i.e., a rather flat temperature profile, until major deformation began. This was indicated by the change from pressure increase to decrease at 36 s.

When the fuel-cladding gap enlarged drastically by radial expansion close to or at the moment of burst, all thermocouples showed a temperature drop; thermocouples 131 and 132, which were located in the ballooned section, showed the most pronounced drop. Heatup continued until the power was reduced at about 80 s. At 160 s quenching was initiated, causing the cladding temperature to drop rapidly to coolant temperature level.

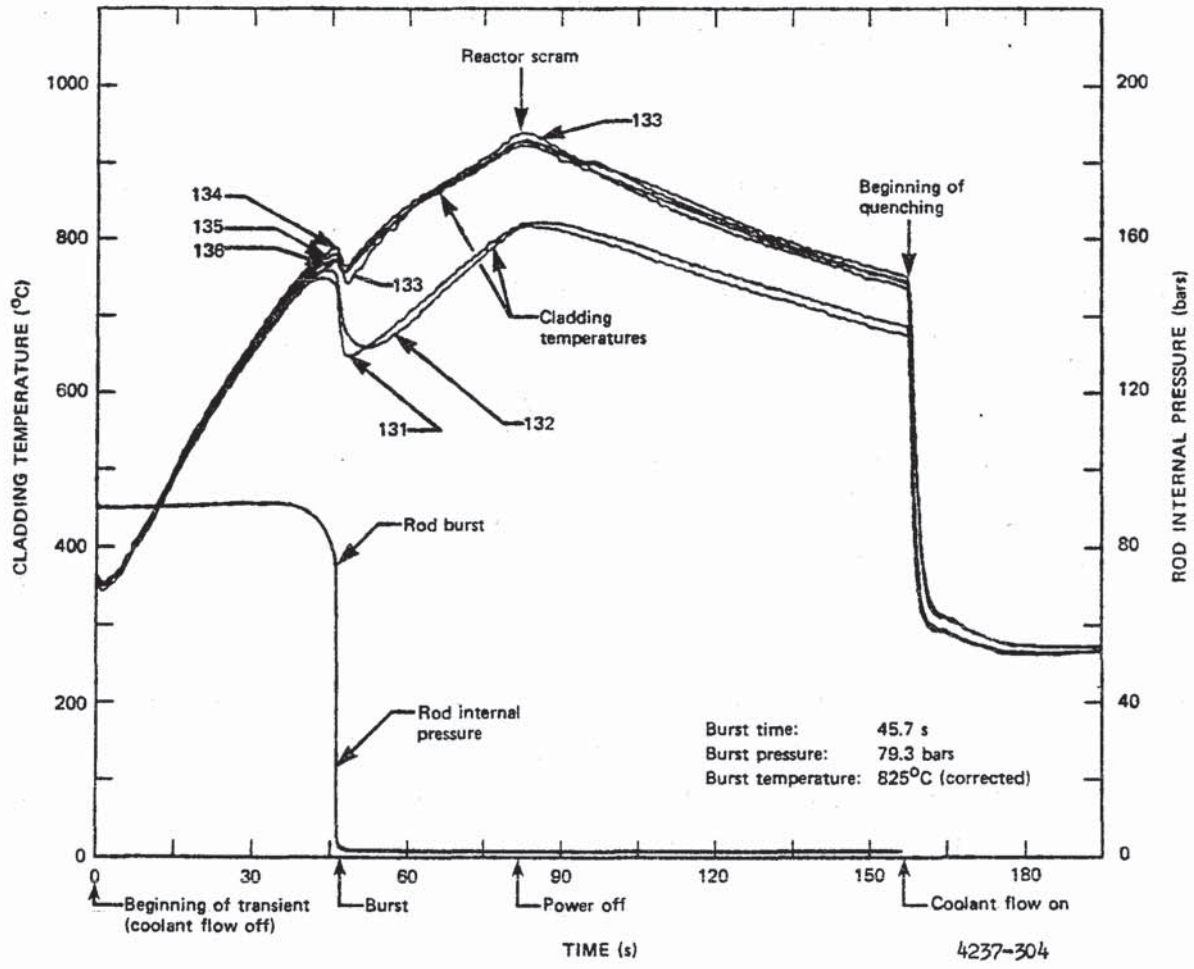

Figure 11: Typical temperature and pressure histories; measured data of test B 3.1

3.6 Test rod power

According to the test conduct a constant rod power was needed until the target rod temperature was achieved.

In order to meet the standard cladding temperature history, calculated for a high rated PWR rod during the reference accident, a local maximum rod power rate of 40 W/cm was needed in the axial center region of the nuclear rod. For the electrically heated simulator a different nominal power rate, 50 W/cm, was needed because it contained different materials, and hence different heat capacities had to be taken into account. The nominal power rates were determined by calculations using the WALHYD-2D computer code.*

The determination of the rod power is generally no problem for electrically heated fuel rod simulators. The power of a nuclear rod is governed by the local fission neutron flux and by the inventory of fissionable material.

Since the fission neutron flux could not be measured directly, and since for previously irradiated rods the concentration of fissionable material usually was not yet known at the time of the transient test, three different indirect methods for power determination were used, based upon

a) enthalpy balance of the coolant passing the test rod

b) measurement of neutron flux near the in-pile tube and total power of reactor fuel elements surrounding the in-pile tube

c) measured heatup rate of test rod cladding.

(a) Coolant mass flow and temperature rise were measured and combined with the specific heat of the coolant to the integral rod power. Possible error sources - besides the measurement uncertainties - were radial heat exchange and coolant bypass flow.

(b) The energy output of the reactor fuel elements surrounding the in-pile tube and the neutron flux profile in the vicinity of the in-pile tube were measured. These data were converted to an average test rod power rate using a conversion factor determined by reactor physics calculations, which took into account the nominal burnup. These calculations

* Calculations performed by D. Steiner, IKE Stuttgart at Stuttgart University

assumed the test rod power to be proportional to the power produced in pertinent axial sections of the surrounding reactor fuel elements. Main error sources: Calculation of conversion factor, uncertainty of burnup, basic assumption of proportionality between rod power and fuel element power.

(c) The test rod power could be determined by a comparison between measured and calculated heatup rates based on the local cladding temperature histories during the transient. The uncertainty in the determination of the heatup rate from the thermocouple readings was low (+ 1 K/s). Main error sources: The computer code calculation which provided the relation between heatup rate and rod power, and the influence of azimuthal differences of cladding temperature.

The axial neutron flux profiles measured for method (b) were normalized and combined with the normalized axial profiles of fissionable material determined by radiochemical analysis to establish a normalized axial power profile of each test rod, as shown schematically in Fig. 12.

Methods (a) and (b) were used during steady-state operation, (c) was a posttest method only. The posttest method based on the heatup rate was considered to be the most confidential one. Table 10, Appendix A, provides detailed information of each test on the power determination by the temperature rise of thermocouples and the enthalpy balance.

4. Results of fuel rod deformation and burst

The burst data, i.e., burst temperature, burst pressure, and maximum circumferential strain at the rupture location, are the main basis for comparison with other tests, particularly with out-of-pile tests. With respect to the potential for significant blockage of coolant channels the axial deformation profile is of great importance, too.

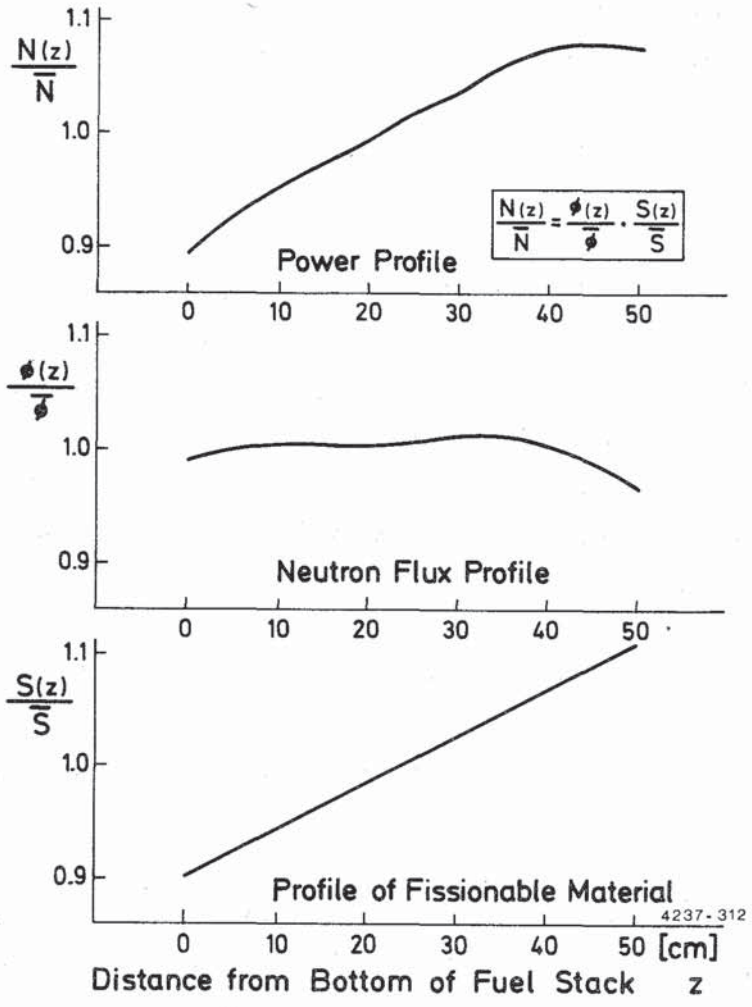

Figure 12: Procedure for the evaluation of the axial power profile of preirradiated rods (normalized), Test F4 as example.

4.1 Appearance of the ruptured regions

During the heatup phase, the pressurized rods suffered deformation over the entire heated length, ballooned locally, and ruptured within the ballooned section /12, 15-20/. With two exceptions all rods burst at the location of maximum strain. The ruptured regions of an unirradiated rod, an irradiated rod, and a rod simulator are presented in Fig. 13. The burst shapes of the three types of rods are similar, and the cross sections of the burst locations do not indicate an influence of irradiation. The only apparent difference is the fragmentation of the irradiated fuel, which is described in Section 5.

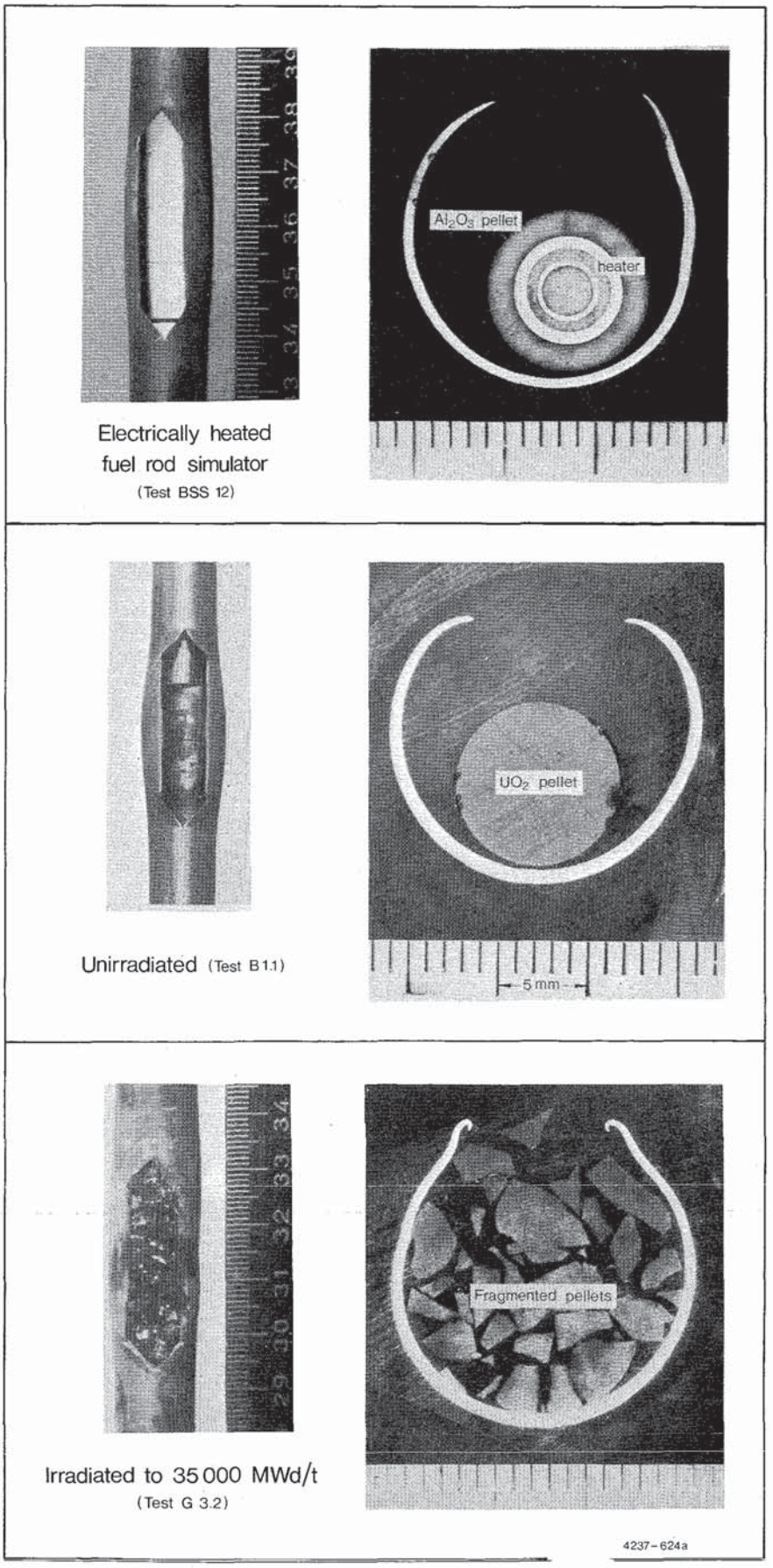

Figure 13: Views and cross sections of rupture regions of fuel rods and rod simulators.

4.2 Burst data

The burst data of the nuclear rods and of the electrically heated rod simulators are listed in Table 5. The statistics of the burst data and heatup rates derived from the data of Table 5 are given in Table 6.

Table 6: FR2 In-pile statistics

Test type (No. of burst rods)	Heatup rate (K/s)		Engineering Burst stress (MPa)		Engineering Burst strain (%)		Rod Internal Volume Change (%)	
	Average	Stand.dev.	Average	Stand.dev.	Average	Stand.dev.	Average	Stand.dev.
Unirradiated (12 rods)	11.5	3.4	37.1	11.4	41.6	12.6	52.2	20.9
Irradiated (24 rods)	11.3	2.0	36.8	16.4	42.2	12.1	51.4	18.0
Electrically heated rod simulators (7 rods)	12.4	0.2	38.2	21.1	37.9	12.3	53.7	34.4

The average values of the burst stress, burst strain, and rod internal volume change are about the same for unirradiated, irradiated rods, and rod simulators.

Burst temperature, burst pressure, and burst strain used in the evaluation of the FR2 in-pile tests are defined as follows:

Burst temperature is the temperature of the cladding at the burst location at the time of burst, and was determined by interpolation between two thermocouples or extrapolation from the thermocouple closest to the burst location. Using this method, azimuthal temperature variations could not be taken into account. With the microstructural evaluation of the cladding temperature it is generally possible to determine the temperature at any given angular position. This method, however, could not be directly applied to the burst temperature because the results were available for the maximum cladding temperature only (see section 6.1).

Burst pressure is the rod internal pressure at the beginning of the fast pressure drop, i.e., when the pressure decrease rate $\Delta p/\Delta t$ exceeds 10 bar/s. The pertinent time after initiation of the transient is called the burst time.

Burst strain is defined as the largest circumferential strain $\Delta U/U_o$ within the ruptured section,

where

$\Delta U = U_1 - U_o$ = increase in circumference

$U_o = \pi\ d_o$ = initial cladding circumference,

with d_o = initial outer cladding diameter.

Since the burst strain was the maximum total circumferential elongation of the rod in almost each test, generally no distinction is made between these two terms in this report.

Burst stress is defined as "engineering hoop stress", given by the equation

$$\sigma_B = p_B \cdot \frac{D_{i,o}}{2 \cdot t_o}$$

where p_B = burst pressure

$D_{i,o}$ = initial cladding inner diameter

t_o = initial wall thickness of the cladding.

The evaluated uncertainties of the burst data are listed in Table 7.

Table 7: Uncertainties of the burst data

Parameter	Max. Uncertainty	Remarks
Burst temperature*		
α) nuclear rods	± 70 K ± 45 K	TC Version A TC Version B
β) rod simulators	± 80 K	TC Version B
Burst pressure	± 1,5 bar	
Burst strain	± 4 %	Percentage of measured strain

* Details see Appendix C

Burst temperature is plotted versus burst pressure in Fig. 14, for all of the data. No difference was found between the burst data from unirradiated rods and from rods irradiated to different burnups, or between the burst data from nuclear rods and rod simulators. Furthermore, burst pressures and burst temperatures measured during the in-pile tests lie within the data band obtained from numerous out-of-pile experiments with electrically heated fuel rod simulators performed at KfK and other laboratories and from other in-pile tests (Fig. 15).

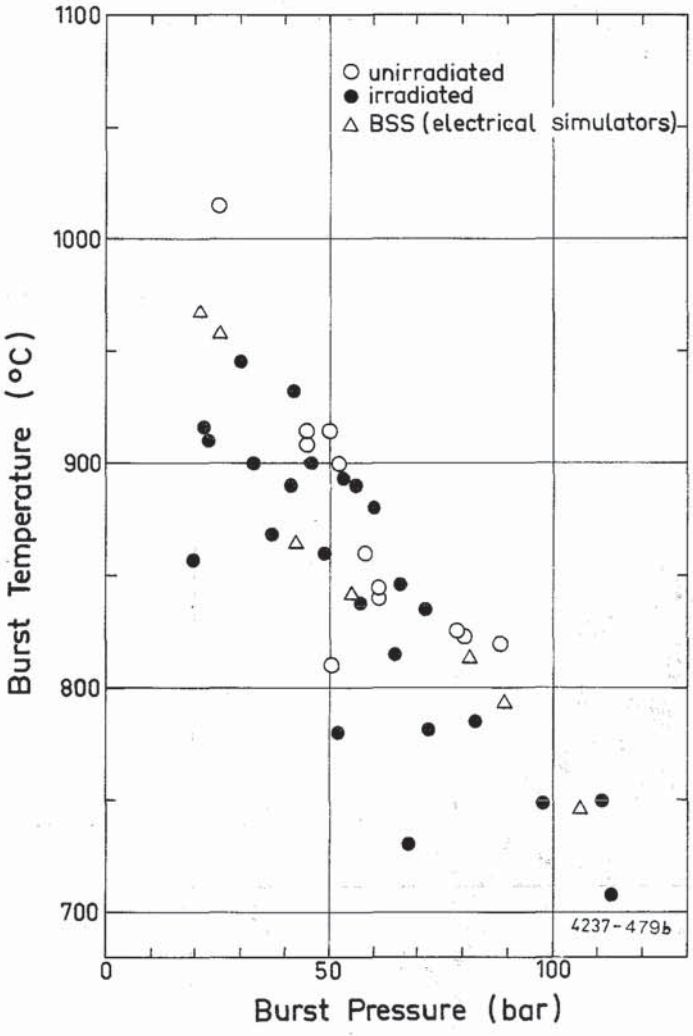

Figure 14: Burst temperature vs. burst pressure

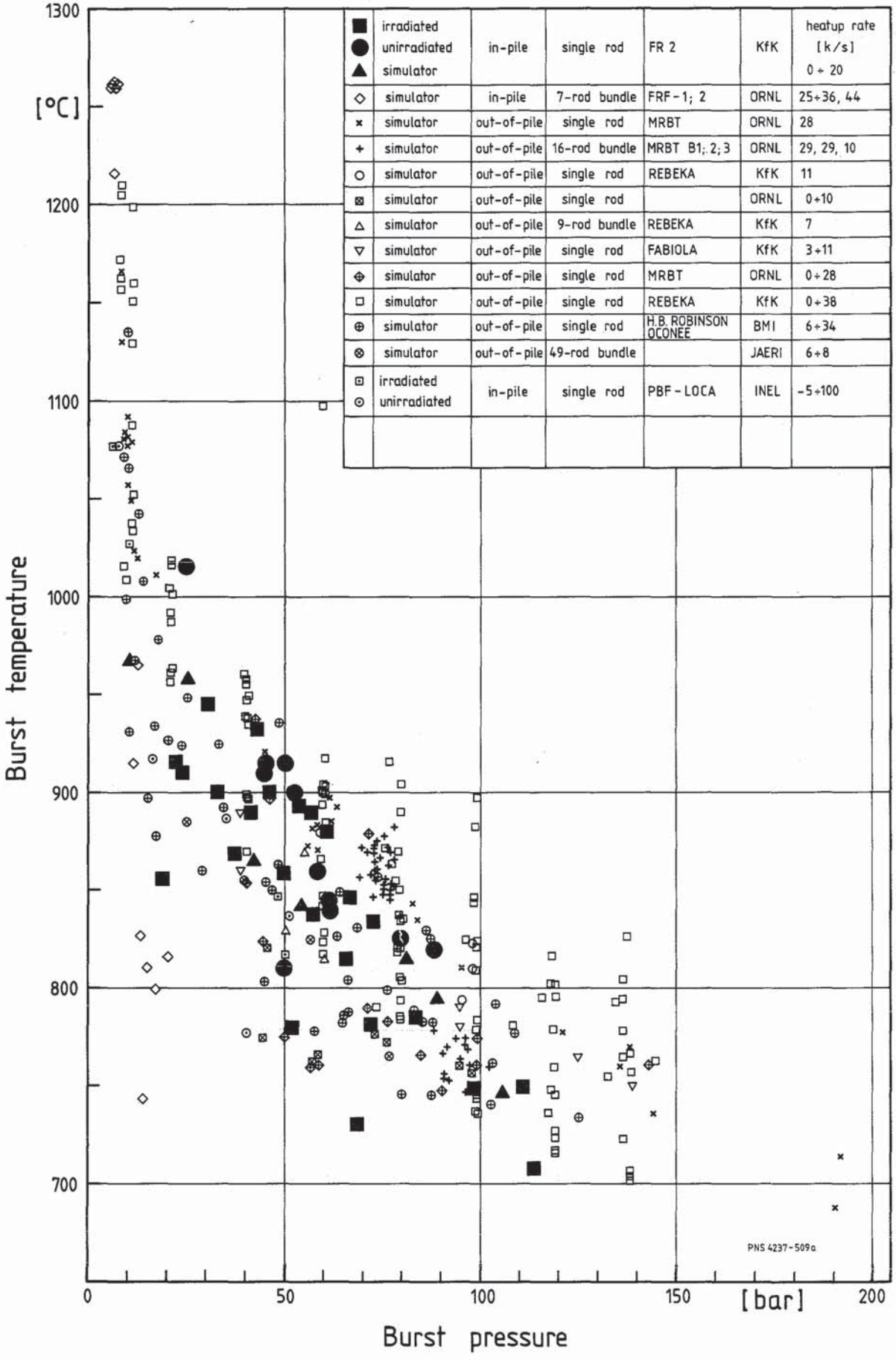

■ irradiated ● unirradiated ▲ simulator	in-pile	single rod	FR 2	KfK	heatup rate [k/s] 0 ÷ 20
◇	simulator	in-pile	7-rod bundle	FRF-1; 2	ORNL	25÷36, 44
×	simulator	out-of-pile	single rod	MRBT	ORNL	28
+	simulator	out-of-pile	16-rod bundle	MRBT B1; 2; 3	ORNL	29, 29, 10
○	simulator	out-of-pile	single rod	REBEKA	KfK	11
⊠	simulator	out-of-pile	single rod		ORNL	0÷10
△	simulator	out-of-pile	9-rod bundle	REBEKA	KfK	7
▽	simulator	out-of-pile	single rod	FABIOLA	KfK	3÷11
◈	simulator	out-of-pile	single rod	MRBT	ORNL	0÷28
□	simulator	out-of-pile	single rod	REBEKA	KfK	0÷38
⊕	simulator	out-of-pile	single rod	H.B. ROBINSON OCONEE	BMI	6÷34
⊗	simulator	out-of-pile	49-rod bundle		JAERI	6÷8
⊡ irradiated ⊙ unirradiated	in-pile	single rod	PBF-LOCA	INEL	-5÷100

Figure 15: Burst temperature of zircaloy tubes from various LOCA-type experiments

In Fig. 16 maximum circumferential strain $\Delta U/U_0$ is plotted versus burst temperature. Again, the FR2 in-pile results from unirradiated rods, irradiated rods, and rod simulators are indicated by different symbols. The results do not show an influence of irradiation on burst strain. For all the data from out-of-pile tests using indirect cladding heating and from in-pile experiments available in the literature /1-3, 21-25/, $\Delta U/U_0$ is plotted versus burst temperature in Fig. 17. The FR2 in-pile test results basically correspond with the maximum deformation found in the other experiments.

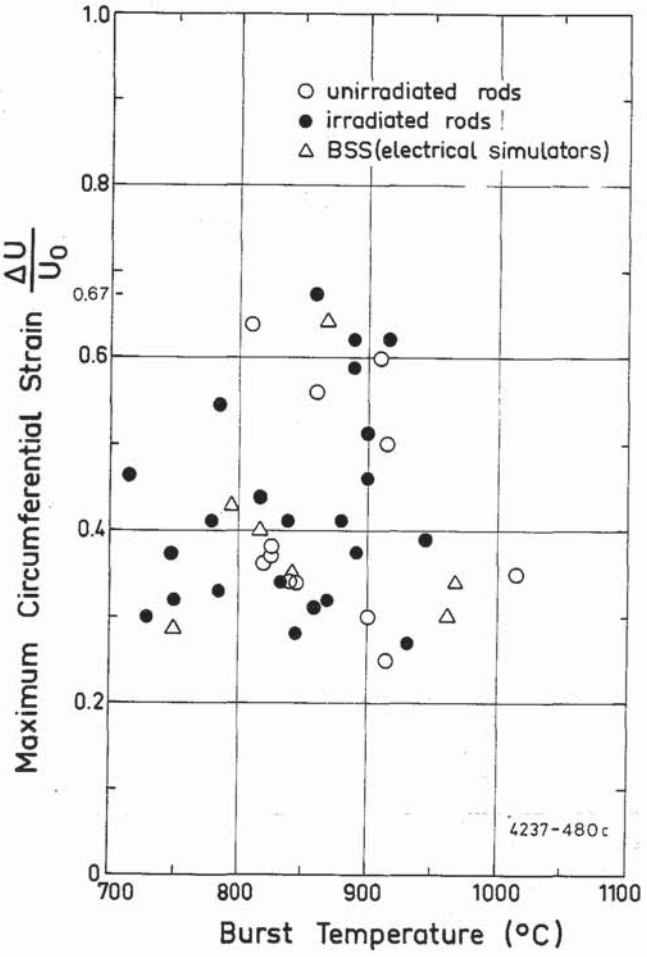

Figure 16: Maximum circumferential elongation vs. burst temperature

The burst strain data of the FR2 in-pile tests lie between 25 and 67%. The 67% limit was reached when the deforming rod touched the shroud, as a deforming rod in a PWR bundle would touch its undeformed neighbors at 66%.

The shroud may have restricted the expansion of some samples. However, the majority of the rods burst at strains of 40% or less, i.e., before the cladding did touch the shroud more than locally. The relatively low strains may be due in part to axial constraint but probably result mainly from azimuthal temperature differences. The influence of the cladding azimuthal temperature distribution on burst strain has been demonstrated in out-of-pile experiments /1,14,22,23,26/. Pronounced cladding temperature differences substantially decrease the circumferential burst strain.

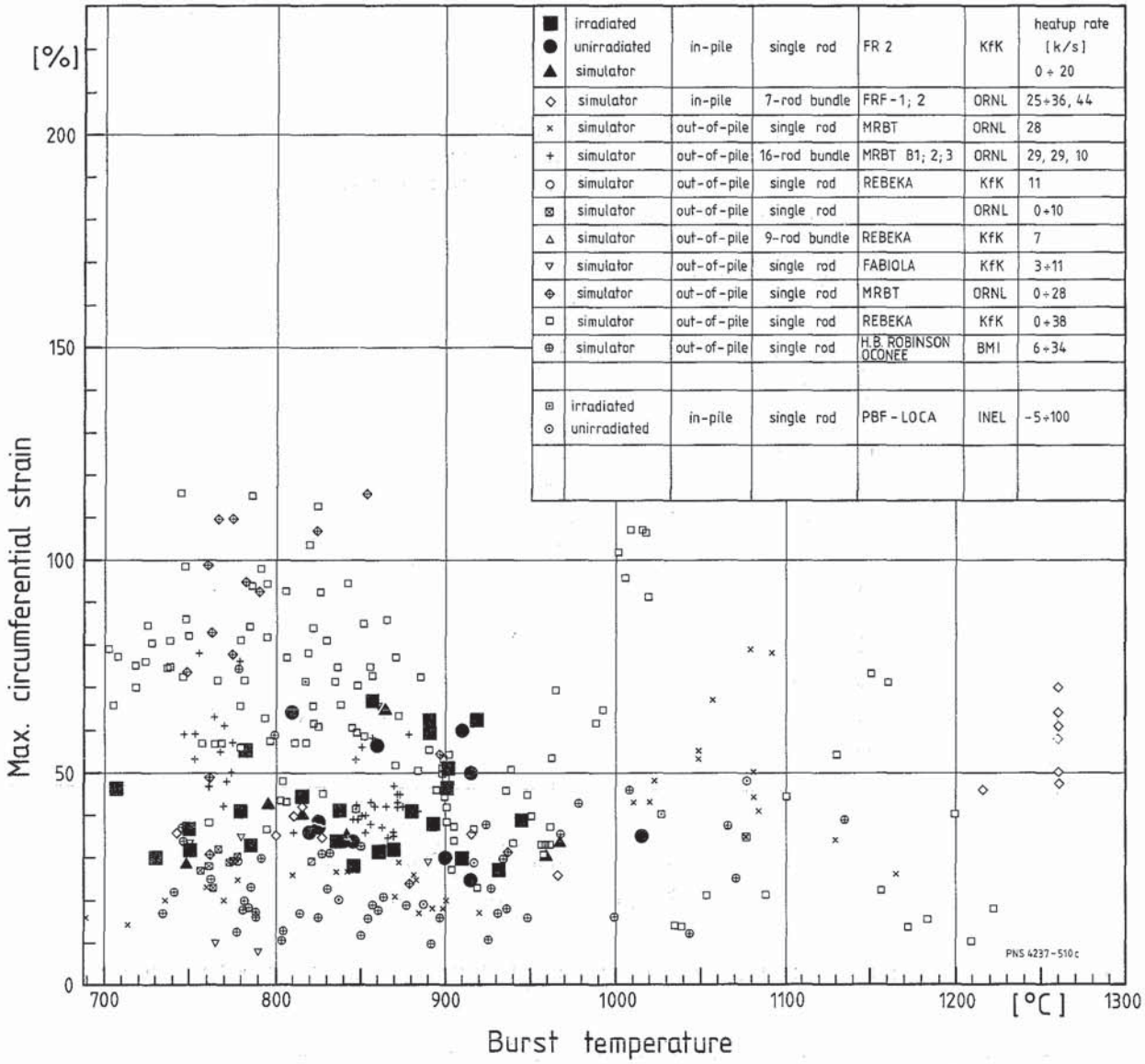

■ irradiated ● unirradiated ▲ simulator	in-pile	single rod	FR 2	KfK	heatup rate [k/s] 0 ÷ 20
◇	simulator	in-pile	7-rod bundle	FRF-1; 2	ORNL	25÷36, 44
×	simulator	out-of-pile	single rod	MRBT	ORNL	28
+	simulator	out-of-pile	16-rod bundle	MRBT B1; 2; 3	ORNL	29, 29, 10
○	simulator	out-of-pile	single rod	REBEKA	KfK	11
⊠	simulator	out-of-pile	single rod		ORNL	0÷10
△	simulator	out-of-pile	9-rod bundle	REBEKA	KfK	7
▽	simulator	out-of-pile	single rod	FABIOLA	KfK	3÷11
⊕	simulator	out-of-pile	single rod	MRBT	ORNL	0÷28
□	simulator	out-of-pile	single rod	REBEKA	KfK	0÷38
⊕	simulator	out-of-pile	single rod	H.B. ROBINSON OCONEE	BMI	6÷34
⊡ irradiated ⊙ unirradiated	in-pile	single rod	PBF-LOCA	INEL	-5÷100

Figure 17: Burst strain compiled from various LOCA experiments

Except for test B 1.7 the azimuthal temperature differences during the transient could not be measured directly. In test B 1.7 four thermocouples were welded at the same axial location (5 cm below the upper end of the fuel stack) and 90° apart. The rupture of the cladding occurred approx. 20 cm below the instrumented section. So the influence of TC attachments and TC leads on the rod deformation were excluded on one hand. On the other hand the measured azimuthal temperature variations of approx. 40 K during steady-state as well as during the transient were strictly valid for the TC plane only. They could not be extrapolated to the burst plane.

For the majority of the tests the azimuthal temperature differences were determined for the maximum cladding temperature at the rupture elevation by microstructural evaluations. By this posttest method, which is described in section 6.1, azimuthal temperature variations between 0 and 100K were found.

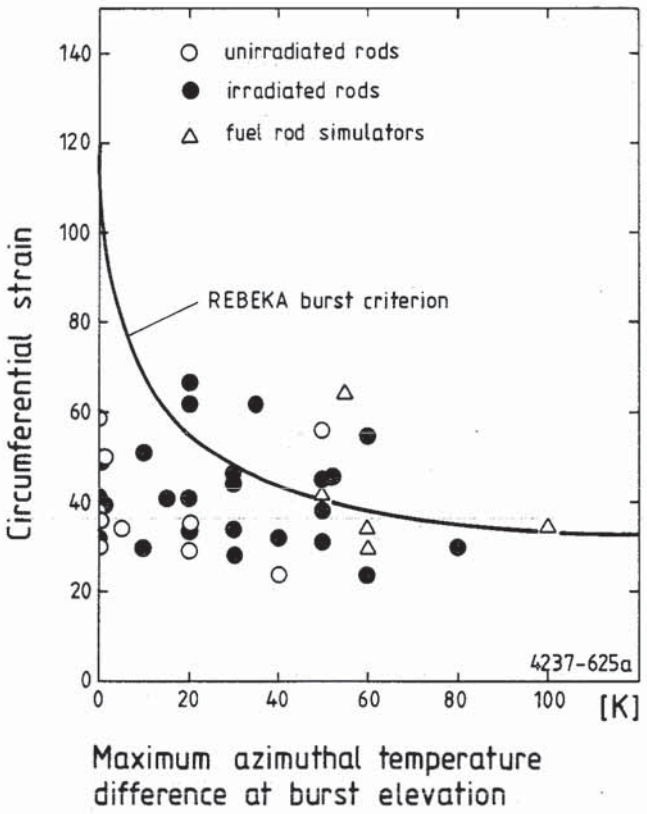

Figure 18: Local circumferential strain versus maximum azimuthal temperature difference in the rupture region derived from the posttest determination of the maximum cladding temperature in cross-sectional samples at different angular positions

In Fig. 18 the circumferential strain, i.e., the local strain of cross-sectional samples in the rupture region, is plotted versus the maximum azimuthal temperature difference evaluated from the microstructure of the cladding material. The given data - as already said above - are strictly valid for the time at peak temperature only. So, they cannot directly be applied to the time of deformation or burst, particularly because the temperature at the fracture tip did generally not result in the highest value at the time after burst compared with other angular positions of the cladding circumference. The data, however, are to give the magnitude of the possible maximum temperature variations during the deformation.

In comparison with the REBEKA burst criterion /26/ in this figure no systematic disagreement is apparent between the in-pile and out-of-pile (REBEKA) results. In addition the figure shows, that both the unirradiated and previously irradiated fuel rods exhibited similar azimuthal temperature differences.

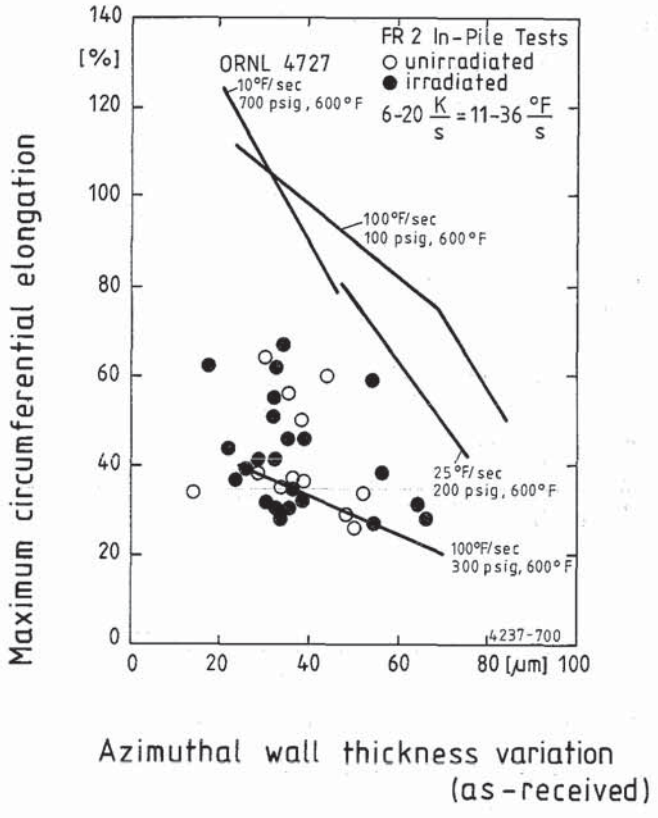

Figure 19: Circumferential elongation vs. azimuthal wall thickness variation; comparison between FR2 in-pile results and ORNL out-of-pile data

Plotting of the burst strain versus the initial wall thickness variation of the cladding circumference (Fig. 19) resulted in a similar relationship as described in /27/. The initial wall thickness variation, however, is only one parameter to influence the burst strain. The azimuthal temperature difference during the deformation process is considered to be the most important one.

No effect of the heatup rate on the burst data could be observed. However, the range of heatup rates covered with these tests was rather small. If there is an influence of the heatup rate it seems to be smaller than the data scatter of the test results.

4.3 Cladding deformation axial profiles

The cladding deformation profile was determined by measuring the rod diameter using a spiral technique and by evaluating the circumference of cross section photographs from the ruptured region. A typical spiral profile is given with Fig. 20. Generally the rod can be divided into three regions with regard to the axial deformation profile:

(1) Regions outside the rupture area with negligible ovality of the cladding ($D_{max} - D_{min} < 50\ \mu m$),

(2) Regions close to the rupture area with distinguishable ovality, and

(3) the rupture region.

Also from the spiral profile it was learned that each test rod exhibited deformation over the entire heated length (500 mm) and that the deformation profile was influenced locally by the thermocouples. Usually the local diameter change due to the TC influence $\Delta d/d_o$ (d_o = initial cladding outer diameter) resulted in 1 to 3%.

The position of ballooning and maximum strain was usually at or close to the position of maximum rod power (see Fig. 24d).

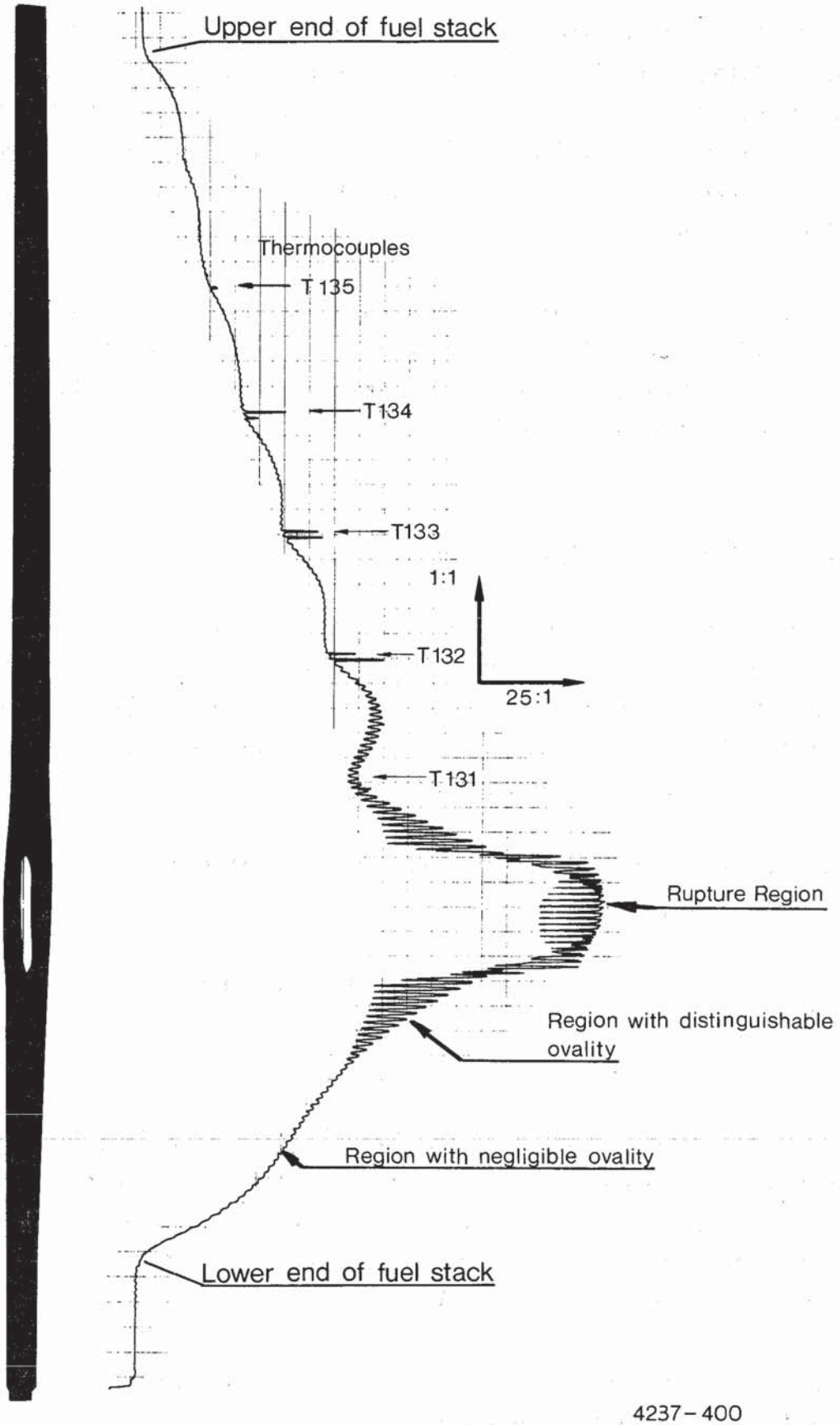

Figure 20: Typical spiral profile; posttest measured rod diameters of test A2.2

However, the relatively flat power profile in most of the tests may have allowed other parameters, e.g., wall thickness, fuel eccentricity, increase of cladding mass and heat transfer surface area by TC leads, to have influenced the position of maximum strain.

The axial profile of the cladding strain in the rupture region is depicted in Fig. 21 for all tested rods and the values are given in detail in Table 12, Appendix A. From the diagram it can be learned that the deformation profile is not flat in the rupture region but pronounced. A difference between the maximum strain and the strain at either end of the crack is apparent. So, even under the flat power profiles of most tests of series A and B, a distinct maximum of deformation within the rupture region was obtained.

The cladding deformation profiles were used to calculate the rod internal volume increase due to cladding circumferential expansion. The volume increase values (which are a measure of the axially averaged circumferential strain) are given in Table 5 for both the nuclear tests and the simulator tests. In Fig. 22 relative volume increase is plotted versus relative internal pressure change $\Delta p/p_{max}$ for the nuclear test rods and the rod simulators. The solid line approximating the data points represents a correlation between relative volume increase and relative pressure change which was analytically developed from a simple two-volume model using the general gas law. The atypical deformation of rod E5 which did not actually burst but lost its fillgas through a crack over a period of several seconds, was not calculated correctly by this simple model.

With Test Rod E5 a cladding deformation extending to the 67% limit at a length of about 10 cm was obtained. The posttest neutron radiograph of this rod (Fig.23) exhibits the deformation shape and the pronounced rod bending above the ballooned region due to the shroud blockage created by the balloon of the test rod. A radial extension of the ballooning above 67% was prevented by the shroud surrounding the test rod such that the cladding had to continue its ballooning into the axial direction. However, the relationship between the average strain and the maximum circumferential elongation was not different for E5 in comparison with the other tests.

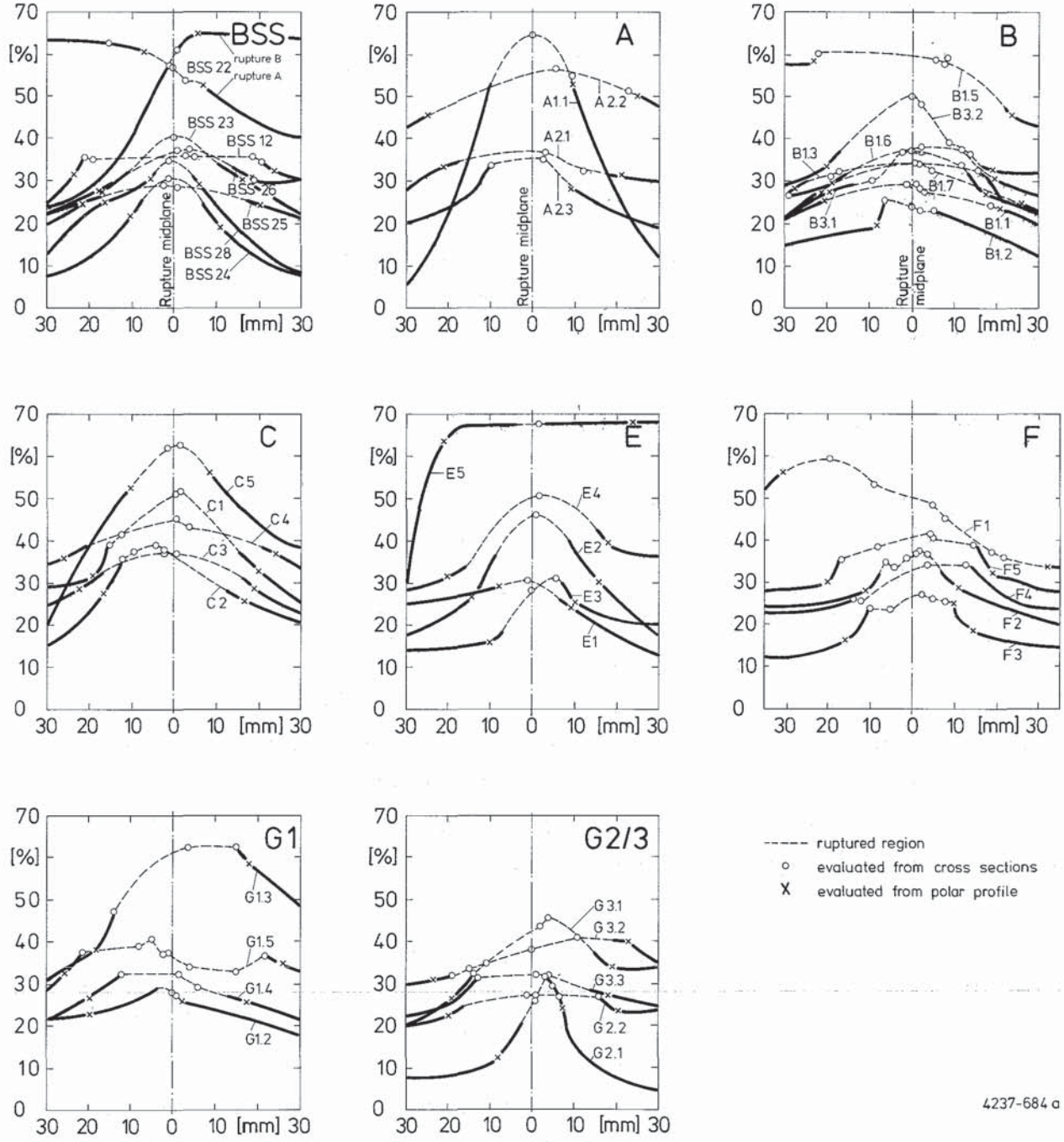

Figure 21: Circumferential elongation profiles of the ruptured regions of nuclear test rods (series A through G2/3) and fuel rod simulators (series BSS).

The deformation behavior of this test may be explained by the atypical test conduct (reactor scram at the onset of ballooning in contrast to the other tests) done on purpose resulting in a cladding temperature decrease during the main part of the deformation and a delayed pressure release through a very small crack in the cladding /20/.

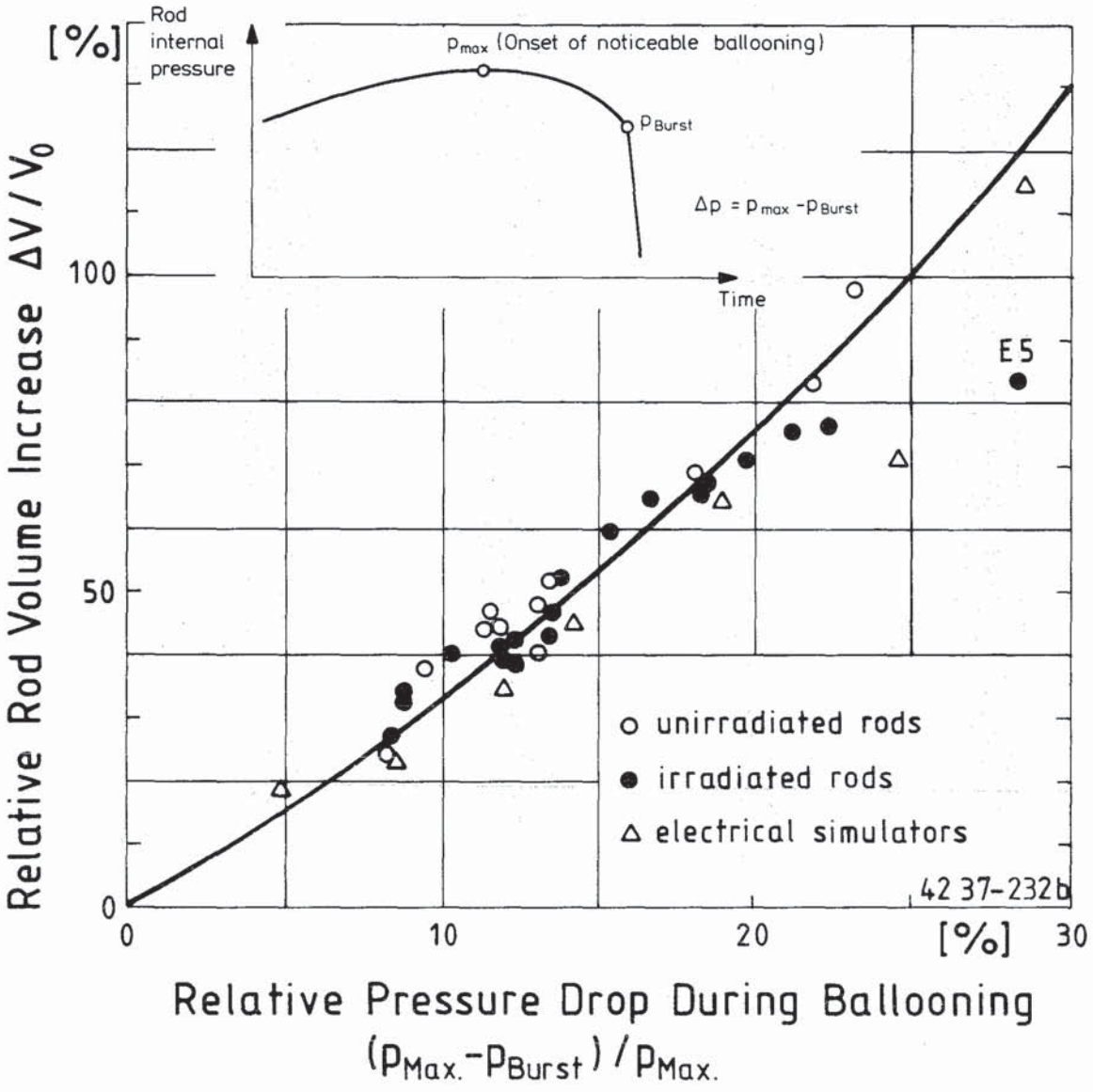

Figure 22: Rod volume increase vs. internal rod pressure drop

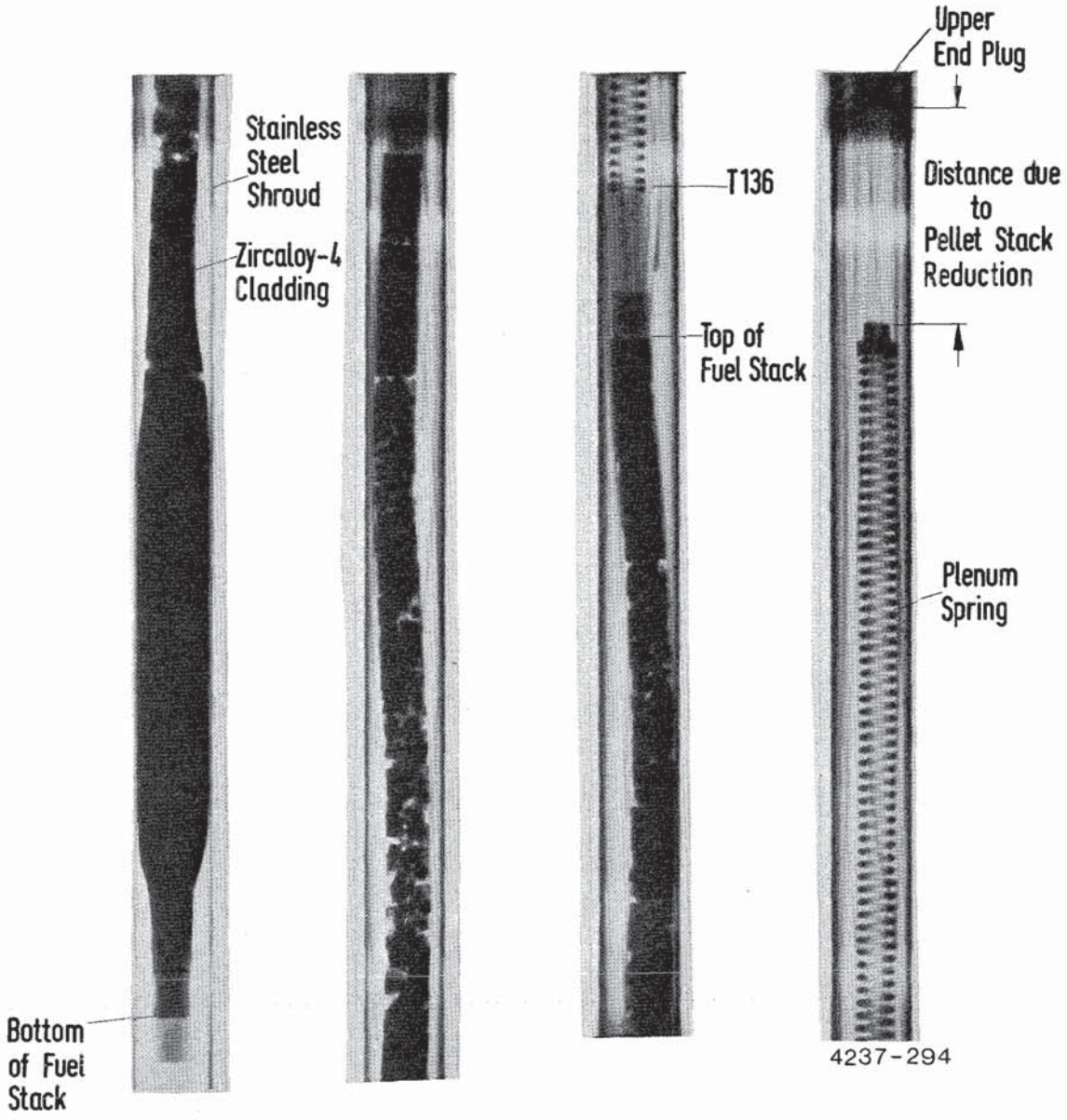

Fig. 23: Posttest neutron radiograph of test-E5 fuel rod

Plotting relative volume increase versus maximum circumferential elongation, (Fig. 24a), a fairly linear relationship was found. Fig. 24a shows data clearly below the linear function and clearly above it but generally following the relationship with the exception of rod A 1.1. The data below the line (C 5, E 2, BSS 28, G 2.1, and BSS 24) exhibit a more localized ballooning (see deformation profiles in Fig. 24b), whereas the data above the line (BSS 22, B 1.5, G 3.2, and BSS 12) result from more extended axial deformation (Fig. 24c). The remainder of the data and the deformation profiles lie between these extremes as shown by the examples of tests F 1 through F 5 (Fig. 24d). Rod A 1.1 was tested with a power profile very different from the profiles in the other tests (peaking factor 1.008 through 1.096) and therefore exhibited a very localized balloon with a small volume increase. This indicates that the empirical correlation is influenced by some of the test conditions, e.g. the axial power profile.

4.4. Circumferential distribution of local strain

The results from various experiments indicate a relation between total circumferential elongation (TCE) and the azimuthal distribution of the local wall thinning, i.e. the local radial strain /26/. Usually, the more uniform the local strain around the circumference the larger is the total circumferential elongation. A smaller total elongation is usually connected with a more localized, i.e. less uniform, wall thinning. The azimuthal strain distribution is believed to be mainly caused by azimuthal temperature variations /22,23/, rather than by initial wall thickness variations or other effects.

From the visual inspection of cross sections taken at the location of maximum circumferential elongation no differences in the posttest wall thickness variation between fresh and irradiated rods and rod simulators of the FR2 in-pile test program were apparent (see photographs of Appendix B).

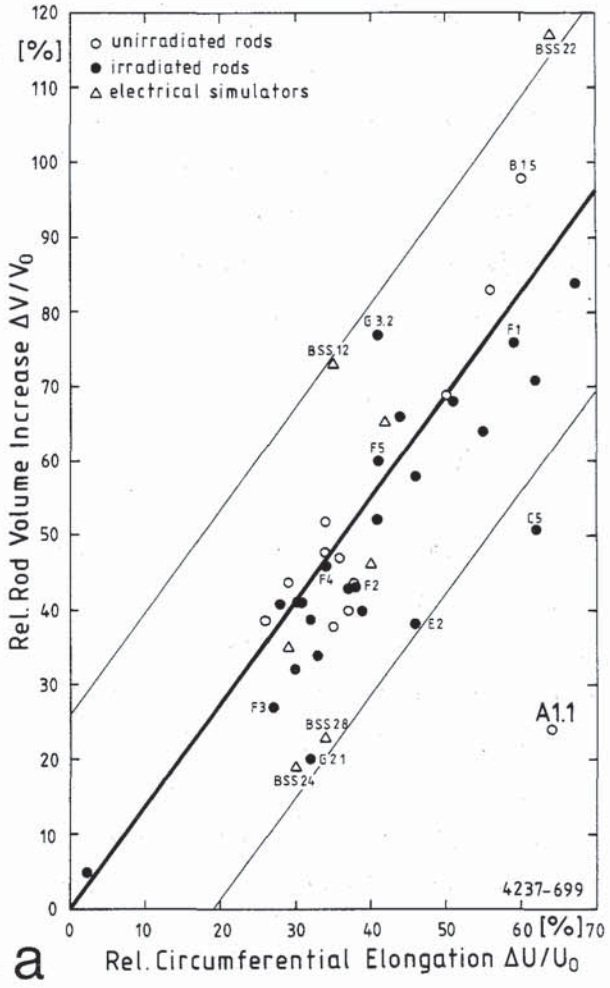

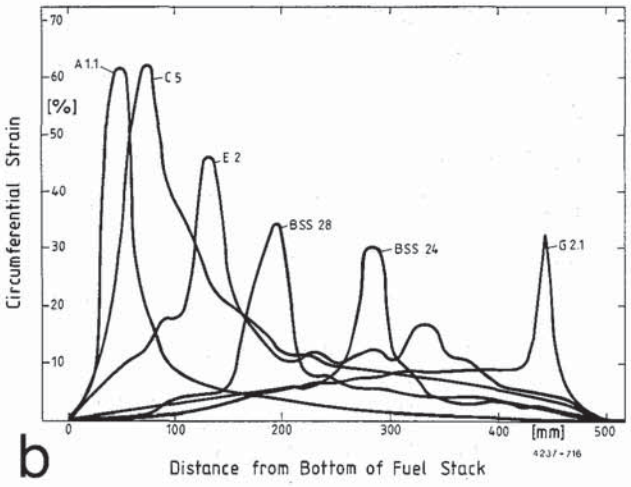

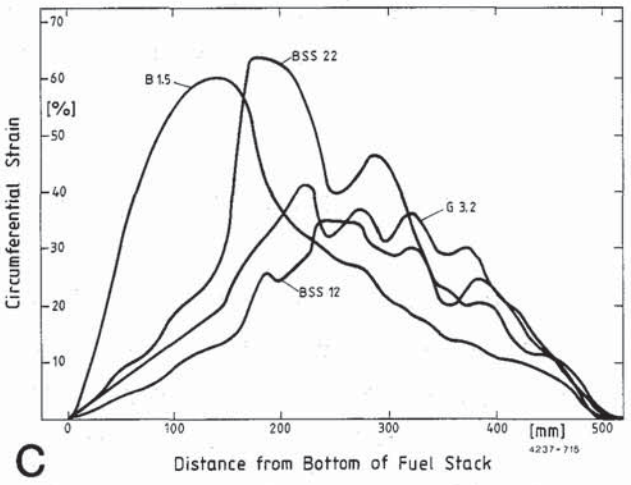

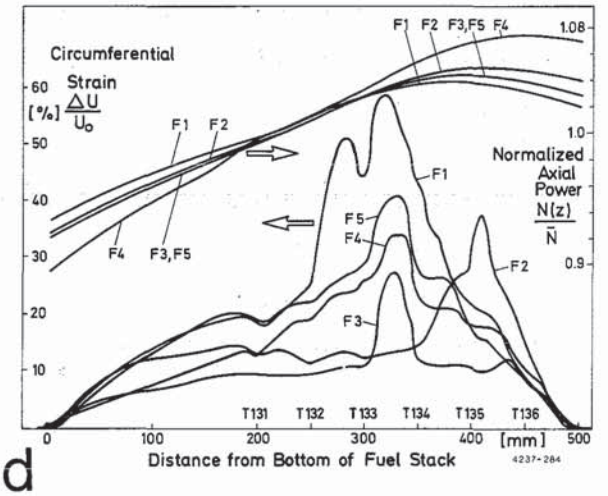

Figure 24: Relative increase of total void volume versus maximum circumferential elongation (24a) and deformation profiles for tests below the average (24b), above the average (24c), and tests F1 through F5 representing the average (24d).

To quantify the circumferential distribution of local strain at the cross section of maximum circumferential elongation a uniformity parameter G was evaluated. With reference to the equation for the standard deviation of a distribution the uniformity parameter G was defined to

$$G = 1 - 2 \cdot \sqrt{\int_0^1 (\varepsilon^*(\psi) - \bar{\varepsilon}^*)^2 \, d\psi}$$

with $\psi = \theta/2\pi$ normalized angular position

θ = tangential angle from the fracture tip, with $\theta = 2\pi$ from fracture tip to fracture tip

$$\varepsilon^*(\psi) = \frac{s_o - s(\psi)}{s_o}$$ local wall thinning

s_o = initial wall thickness

$$\bar{\varepsilon}^* = \int_0^1 \varepsilon^*(\psi) \, d\psi$$ average wall thinning

G is defined between 0 and 1 ($0 \leq G \leq 1$). Small values of G indicate extremely nonuniform, and high values uniform circumferential deformation of the cladding.

The results of G are plotted versus total circumferential elongation (TCE) for some of the rod simulators, of the unirradiated rods, and of the irradiated rods in Fig. 25. No difference is evident between the different types of rods, i.e. the deformation of the cladding circumference was not influenced by the nuclear environment. With G values around 0.6 to 0.7 the distribution seems more uniform than nonuniform.

The possibility was checked of using the Radial-Strain Localization Parameter W by Chung and Kassner /4/ for the description of the uniformity of the cladding circumference. The result of this investigation was that the W parameter (a) is very sensitive on the evaluation of the wall thickness at the fracture tip, (b) is not independent from the total circumferential elongation, i.e. for a given wall thickness at the fracture tip it decreases with increasing TCE.

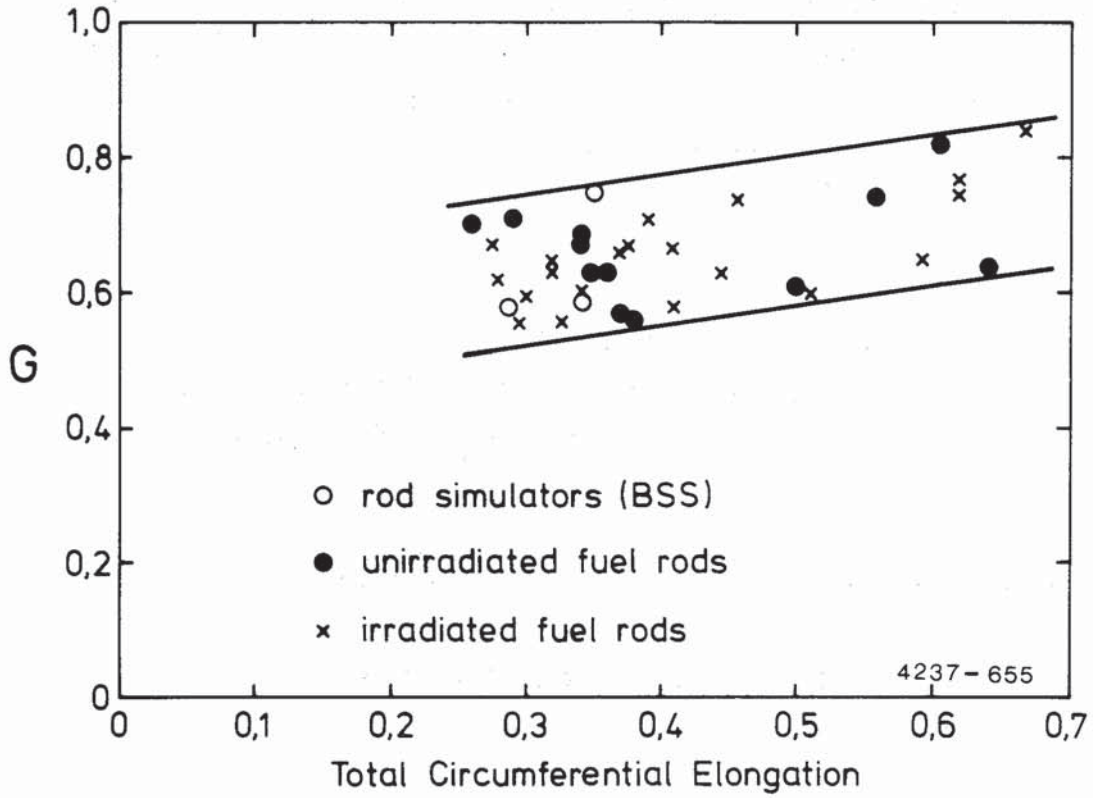

$$G = 1 - 2\sqrt{\int_0^1 (\varepsilon^*(\psi) - \bar{\varepsilon}^*)^2 \, d\psi}$$

$$\varepsilon^*(\psi) = \frac{S_0 - S(\psi)}{S_0} \qquad \bar{\varepsilon}^* = \int_0^1 \varepsilon^*(\psi) \, d\psi$$

Figure 25: Uniformity parameter G as a function of the total circumferential elongation for the FR2 in-pile tests

4.5 Rupture opening dimensions and orientations

All rupture openings of the FR2 in-pile test rods were in the axial direction, because the tangential stress in the cladding material is higher than the axial stress during the ballooning. The rupture opening data, i.e. axial and angular position, rupture length, and maximum width, are given in Table 11, Appendix A.

The length varied between 4 mm (Tests G 1.2 and G 1.5) and 62 mm (Test F 1), the maximum crack width between 0.1 mm (Test E5) and 11 mm (Test G 3.3). An influence of the burst temperature (zircaloy phases α, $\alpha+\beta$, and β) on the burst shape as described in /4/ could not be detected in the results of the FR2 In-pile Tests.

The axial location of the rupture generally occurred in the region of maximum strain, i.e. the burst strain was identical to the maximum circumferential elongation. This is valid for all tests with two exceptions: rod simulators BSS 22 and BSS 26. The rupture of BSS 26 was located about 75 mm below the elevation of maximum strain. This might be explained by greater azimuthal temperature variations of the rupture elevation compared to the position of maximum strain. BSS 22 was the only test rod of the entire program presenting two ruptures, one was located 50 mm above and the other one 10 mm below the elevation of maximum strain. Since it takes internal overpressure for a rupture, the two ruptures must either have occurred simultaneously, or the first rupture was temporarily re-closed before the internal pressure was totally relieved. The closure of the first rupture may have been caused by a fragment of an alumina ring pellet, or - more likely - by contact of the cladding with the shroud. The latter assumption seems more probable regarding the 64% circumferential elongation at the location of the first rupture /12/.

For all rods the orientation of the rupture was compared to the initial wall thickness variations in the rupture plane (see Table 11, Appendix A): In many tests, the rupture occurred near the orientation of minimum initial (as-fabricated) wall thickness. However, the number of test rods that ruptured in the opposite part of the circumference is not negligible. Thus, azimuthal variation in the initial wall thickness is only one parameter which can affect the rupture orientation. The azimuthal temperature distribution during the deformation process is the more important parameter /1, 22, 23/.

4.6. Cladding length change and test rod bending

Cladding length changes for the in-pile tested rods are given in Table 11, Appendix A, and plotted versus burst temperature in Fig. 26 together with the approximations of ORNL out-of-pile results /3/ and KfK REBEKA out-of-pile single rod results.

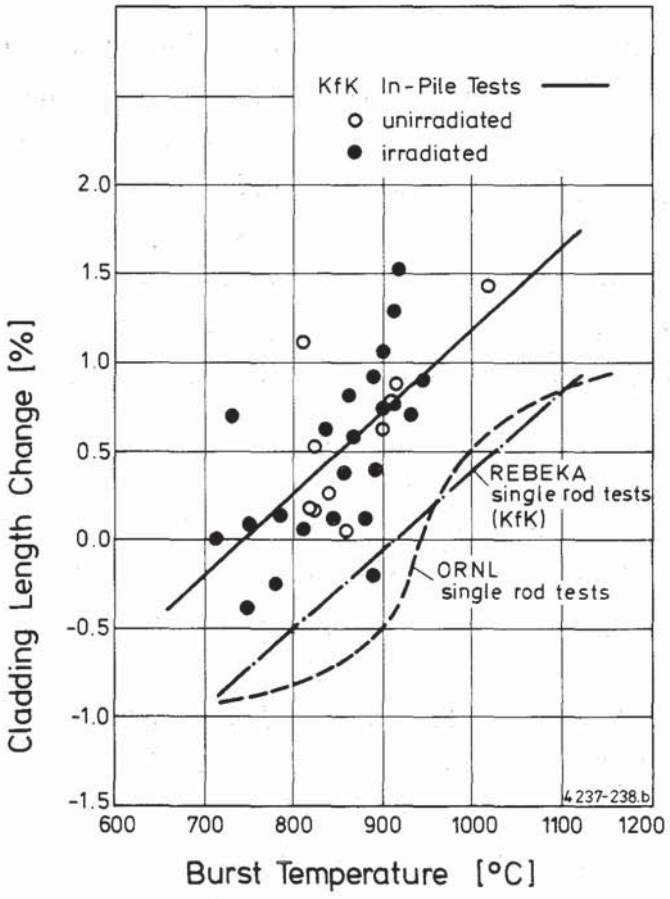

Figure 26: Cladding length change vs. burst temperature

No difference in length change was apparent between the unirradiated and irradiated test rods. Nearly all of the rods increased in length. This indicates that the axial contraction which occurs during ballooning for temperatures below 840°C /4/, due to the anisotropy of α-phase zircaloy, was constrained by the pellet stack and the plenum spring. This constraint possibly contributed to the relatively low circumferential strains of the FR2 test rods in this temperature range.

Test rod bending is defined as the maximum deviation of the rod axis from a straight line drawn between the top and bottom of the rod and is illustrated schematically in Fig. 27. The measurements were made by use of opposing sensors scanning the deformed cladding moving along the rod at several angular positions. The maximum deviation values ranged from 1.0 to 4.6 mm, with an average of 1 to 2 mm, and are given in Table 11, Appendix A. Out-of-pile results /4/ showing significant bending below 840°C (α-phase zircaloy) and negligible values above 840°C, could not be confirmed by the in-pile tests with nuclear rods. In particular, the phenomenon learned from out-of-pile results, that - in the α-phase range of zircaloy - the axial shrinkage of the cladding bowed the rod in such a way that the azimuthal hot spot was forced toward the annular pellets surrounding the heater and the opposite side was lifted away from the heat source was not observed explicitly in the FR2 In-pile tests with nuclear fuel rods.

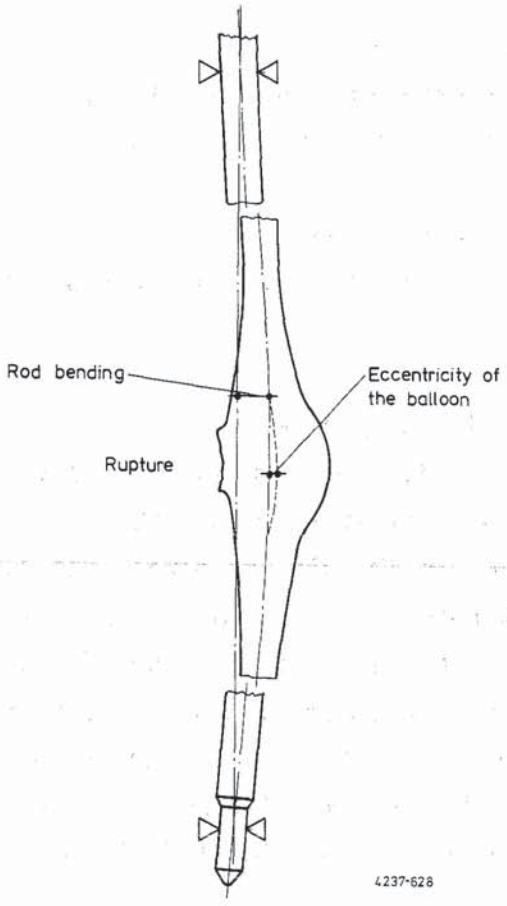

Figure 27: Schematic of rod bending

This may be explained by the fact that a stack of fuel pellets is less rigid than a solid heater rod. Two of the three in-pile tests with electrically heated simulators which burst in the α-phase range resulted in a more asymmetric balloon as found in out-of-pile tests.

The orientation of the rod bending in all in-pile tests was consistent with out-of-pile results /4,23/, i.e. the rupture was on the inside of the bend. In the absolute amount of bending there was no difference between the nuclear rods and the simulators tested in-pile (Table 11, Appendix A). The eccentricity of the balloon (see Fig. 27) was the same order of magnitude as the bending data.

5. Mechanical behavior of the fuel

5.1 Fuel fragmentation

During the LOCA transient, the fuel in the previously unirradiated test rods either did not crack or cracked into only a few large fragments. In most cases only micro-cracks were found in the UO_2 pellets.

The low rod power used to simulate decay heat (40 W/cm) was not sufficient to cause UO_2 fragmentation. Also, the fuel was not preconditioned before testing.

The fuel in the irradiated fuel rods, however, was significantly fragmented. As in commercial fuel rods, pellets in the test rods cracked during operation at power. Crack patterns, i.e., the number of radial, tangential and transversal cracks in the UO_2 and hence, the size and shape of the fuel particles are determined by irradiation parameters. Typical crack patterns after irradiation to the highest burnup of 35000 MWd/t_u and the lowest burnup of 2500 MWd/t_u are shown by cross sections in Fig. 28. The crack patterns are comparable with those from transient-tested rods of the same burnup as can be seen in the same figure. The longitudinal sections of rod C6 (low burnup) and G 1.6 (high burnup), Figure 29, underline this statement.

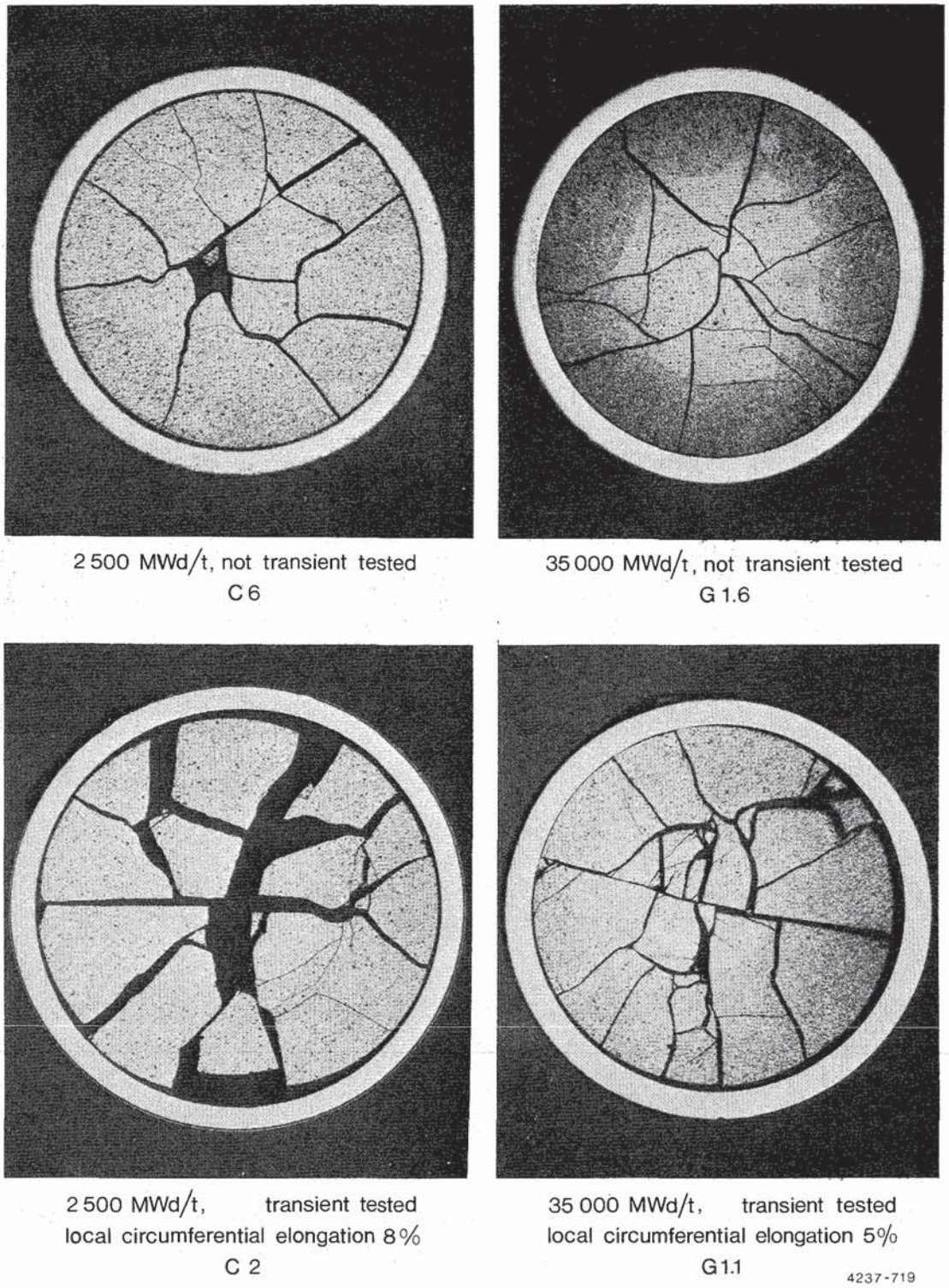

2 500 MWd/t, not transient tested
C 6

35 000 MWd/t, not transient tested
G 1.6

2 500 MWd/t, transient tested
local circumferential elongation 8 %
C 2

35 000 MWd/t, transient tested
local circumferential elongation 5 %
G 1.1

4237-719

Figure 28: Cross sections of high and low burnup rods show comparable crack patterns between rods with and without transient test

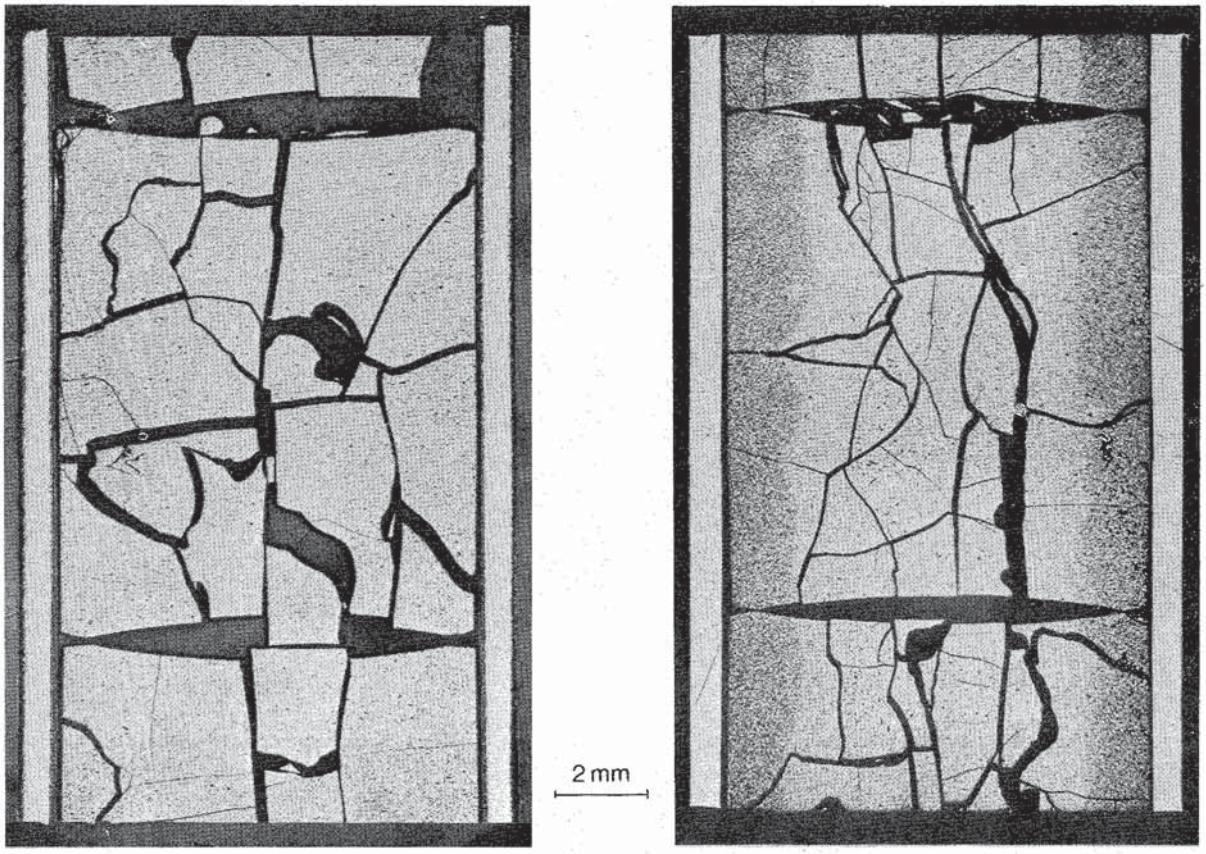

Figure 29: Longitudinal sections of low burnup rod C6 (2500 MWd/t_u) and high burnup rod G 1.6 (35000 MWd/t_u)

Fuel fragments after transient testing were found as loose particles, not sintered together or bonded to the cladding. In the irradiated but not transient tested rods occasionally some particles would adhere slightly to the cladding but could be easily removed.

Fuel fragments of the reference rods G 1.6 (35000 MWd/t_u) and C 6 (2500 MWd/t_u) that were irradiated and not transient tested are shown in Fig.30.

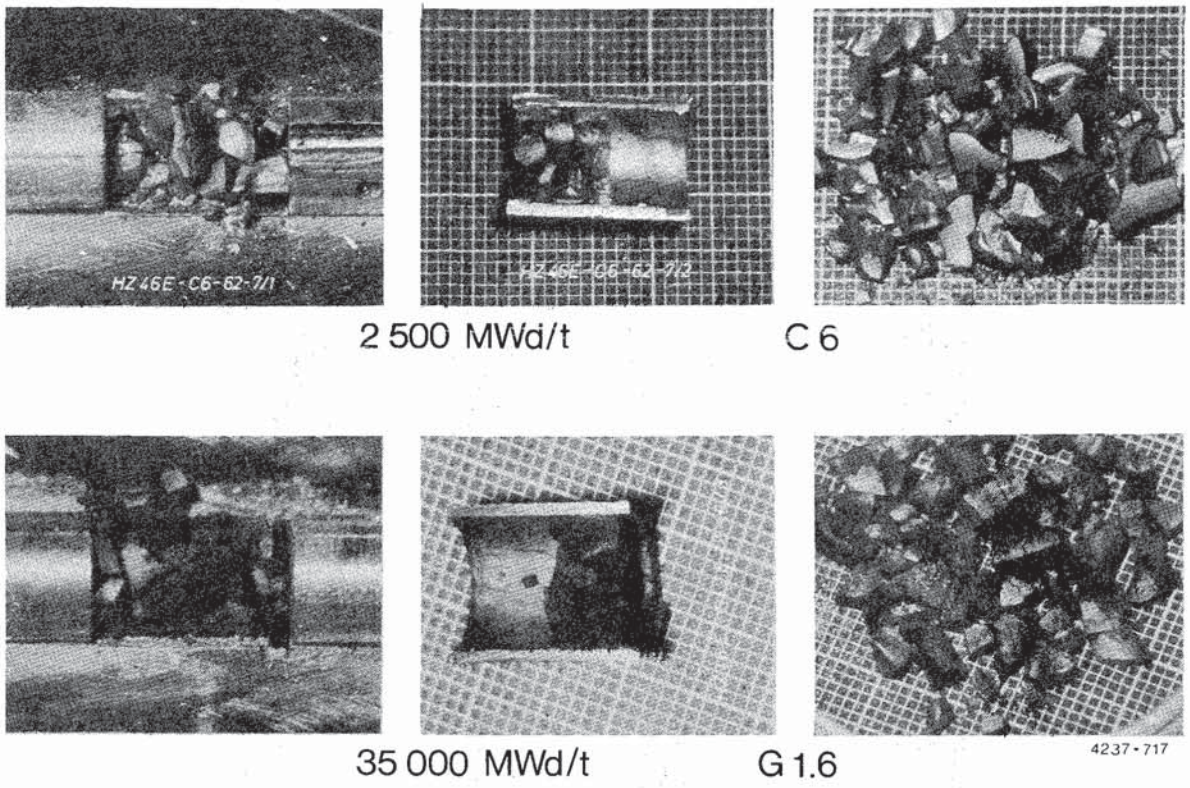

Figure 30: Fuel pellet fragments from G 1.6 fuel rod (irradiated to 35000 MWd/t, not transient-tested) and C 6 fuel rod (irradiated to 2500 MWd/t, not transient tested)

5.2 Fuel relocation during the transient testing

During the steady state operation the fuel pellet fragments of the preirradiated rods were held in place by the cladding. When the cladding ballooned away from the fuel, the fuel slumped outward and downward such that the fragments filled the additional space in the rod provided by the radial deformation of the cladding. As a consequence, the pellets lost their shape in the ballooned sections, and the pellet stack length was significantly reduced for rods with major deformations. This phenomenon is illustrated for Test F1 by the neutron radiography (Fig.31).

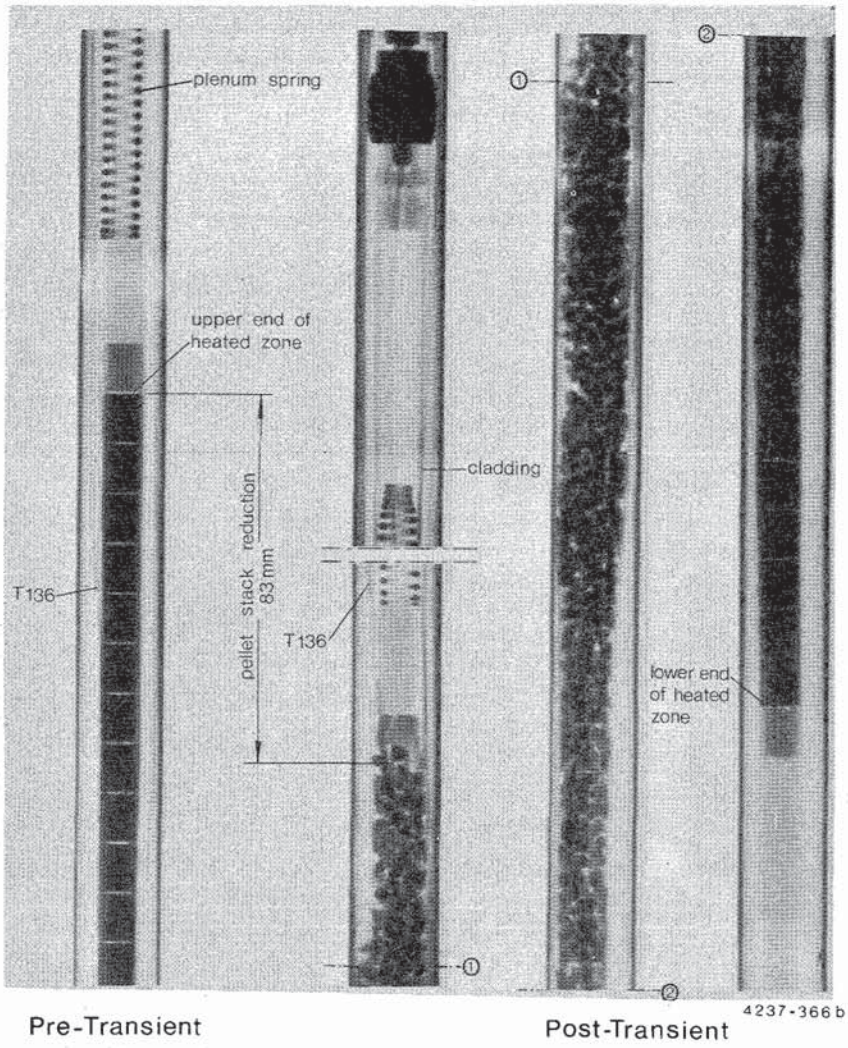

Figure 31: Neutron radiographs of rod F1 (burnup 20 000 MWd/t_u). Comparison between status pre-transient and post-transient

The pellet stack reductions of the test rods are listed in Table 11, Appendix A. They were between 3 and 83 mm.

In Fig. 32 the percentage reduction of the initially 50 cm high pellet stack is plotted vs. the relative rod volume increase.* The data points are rather well approximated by a linear function, indicating that it takes a minimum volume increase of around 18 % to initiate stack reduction.

---

* based on the total rod internal volume consisting of fission gas plenum, pressure transducer with connected tubing, gap and dishing volumes.

An important question was, whether this type of fuel relocation occurs before the burst and thus may affect the deformation, or after the burst when the deformation process is essentially terminated. For this purpose two tests, E3 and E4, were performed with a special thermocouple instrumentation.

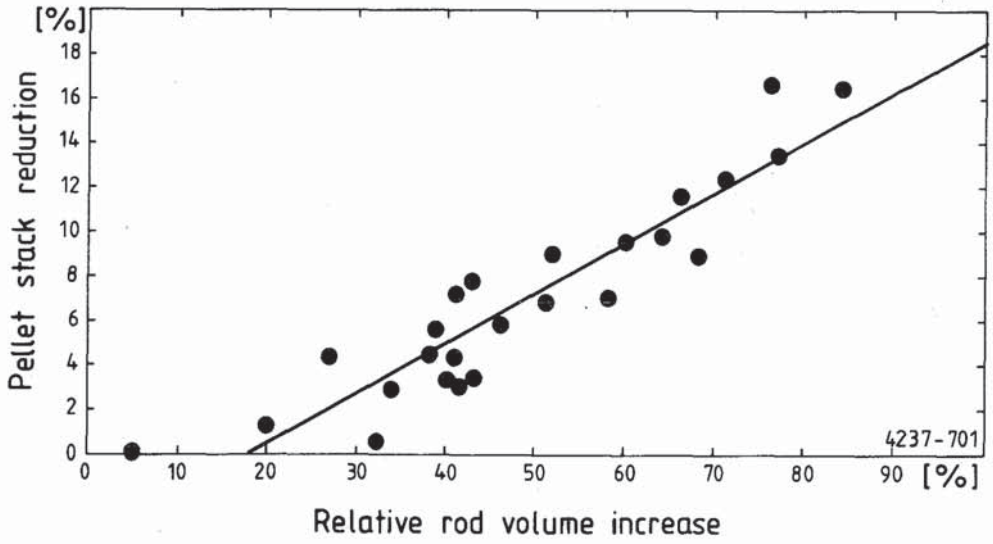

Figure 32: Pellet stack reduction vs. rod volume increase for the preirradiated rods.

In both tests, three thermocouples were welded to the cladding at the elevation of the upper end of the fuel stack to monitor the collapse of the pellet column. Fig. 33 presents the thermocouple instrumentation and the cladding temperature and internal pressure histories of Test E4. Those of Test E3 looked similar. At the time of burst, the three lower thermocouples (T 131, T 133, T 135) behaved as usual, i.e., moderate temperature reduction indicated the increase of gap width and flow of relatively cold plenum gas past the TC locations. The severe temperature drop of the upper thermocouples (T 137, T 138, T 139) at burst time and the relatively slow temperature increase after the burst, however, clearly indicated fuel movement. The fuel stack height reduction was about 50 mm in Test E4, as evaluated from posttest neutron radiographs.

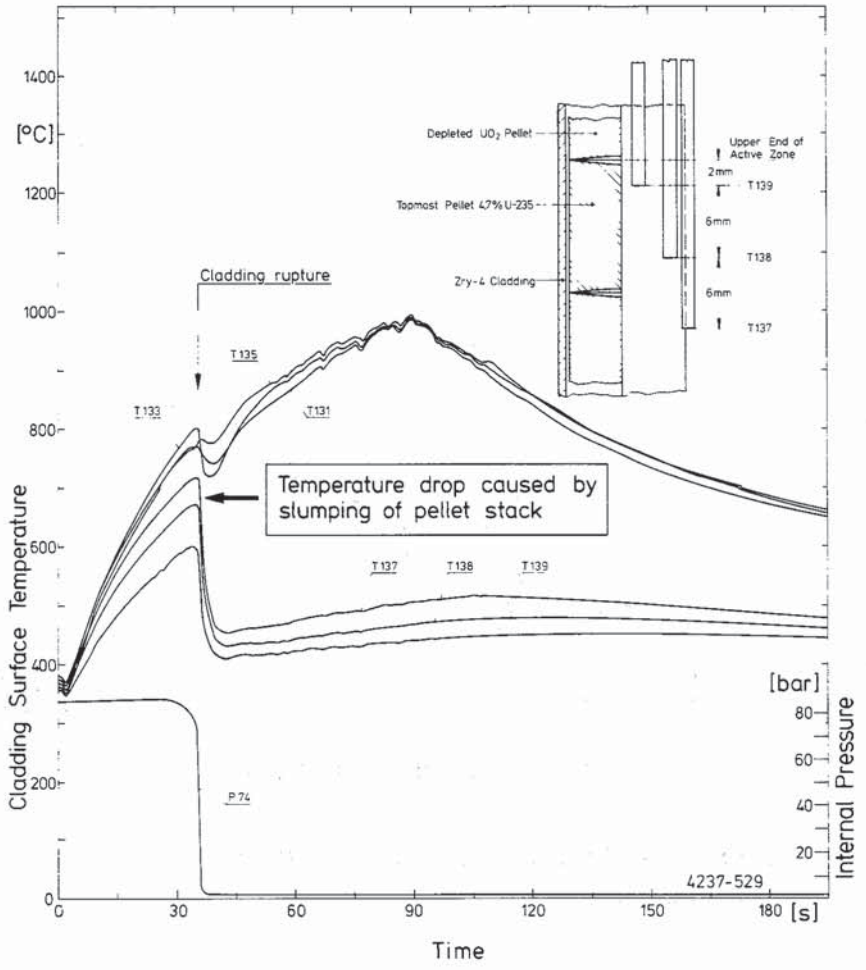

Figure 33: Test E4 temperature and internal pressure histories

The results from the two tests demonstrated that the fuel movement happened at or immediately after the burst, so that the deformation was not affected by the fuel fragmentation. From Test E5 with the objective of freezing a balloon before burst (section 4.3) it was learned that the fuel column collapsed without a burst, only by ballooning.

The fuel movement in the deformed rods causes changes of the axial distribution of the heat source which is of interest for the determination of the thermal conditions after the deformation process, e.g., the assessment of the long-term coolability. By measuring the fuel weight of the rod sections used for particle size analysis (section 5.3) the local fuel mass of these selected samples was determined. The results are listed in Table 14, Appendix A. In Fig. 34 the local fuel mass per unit rod internal volume is plotted vs. the average total circumferential elongation (TCE) of the individual sample.

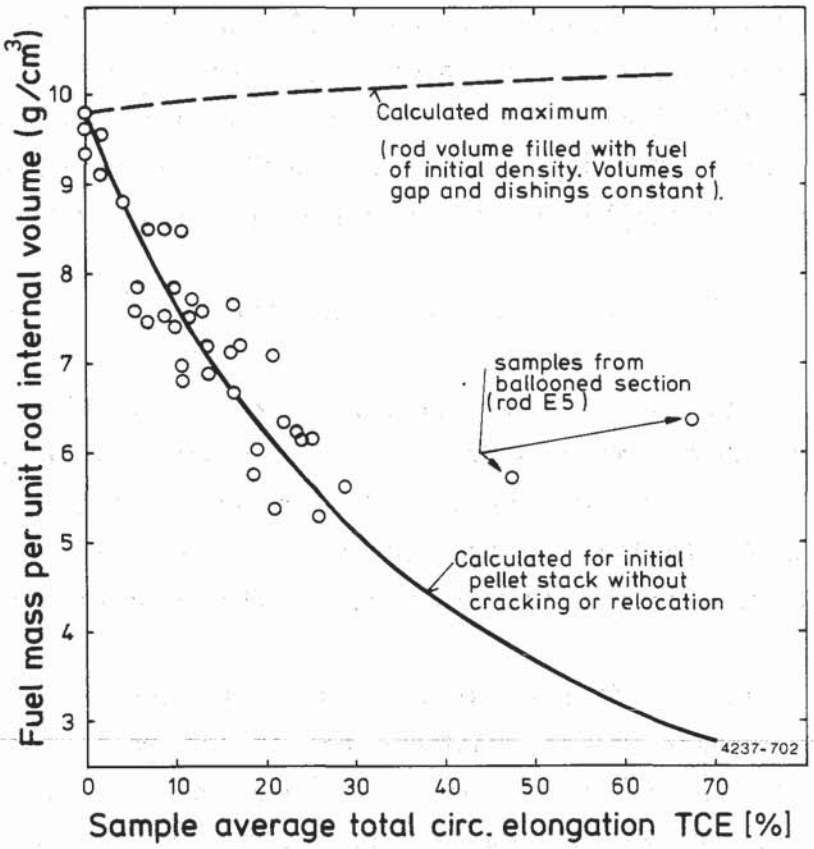

Figure 34: Fuel mass per unit volume of deformed cladding tube after relocation during LOCA burst test

The diagram shows for most of the samples a decrease of fuel mass per unit rod volume corresponding to the increase of TCE, i.e. corresponding to the volume increase. This means that for these samples the fuel mass per unit rod length remained constant. These samples were taken from rod regions with minor deformation. Two samples (of rod E5) were taken from the ballooned section; they show essentially more fuel mass per unit volume, but the absolute value is still less than the initial one. The fuel mass per unit rod length and per unit rod surface area (Table 14), however, are higher than in the undeformed rod.

5.3 Fuel particle size analysis

With the main objective of quantifying a possible additional fuel cracking during the transient tests, up to three fuel samples were taken from nearly each preirradiated rod and submitted to sieve analyses, which provided a particle size distribution for each sample. As an example seven such distributions (the samples of test series F) are shown in Fig. 35.

From the body of all distributions the following statements were derived:

- Within each test series the particle size distribution of the reference rod, which was irradiated but not exposed to a transient, either lies within the range of distributions of the transient tested rods or shows the tendency towards smaller particles. This indicates, that no additional cracking took place during the transient tests.

- Although there is some data scatter, all distributions look very similar: The two largest weight fractions are at the mesh widths 2 and 3.15 mm. Thus, 65 through 90 wt. % of each sample are particles between the sizes of 2 and 4 mm. The calculated average particle size is 2.78 mm.

- Looking for an influence of burnup on particle size distribution for the series C (2500 MWd/t_u burnup) and series E (8000 MWd/t_u), a tendency towards larger particles than in the other series was found (see Fig.36).

From this it may be concluded, that the process of essential cracking during irradiation in the FR2 reactor was terminated between 8000 and 20 000 MWd/t_u burnup.

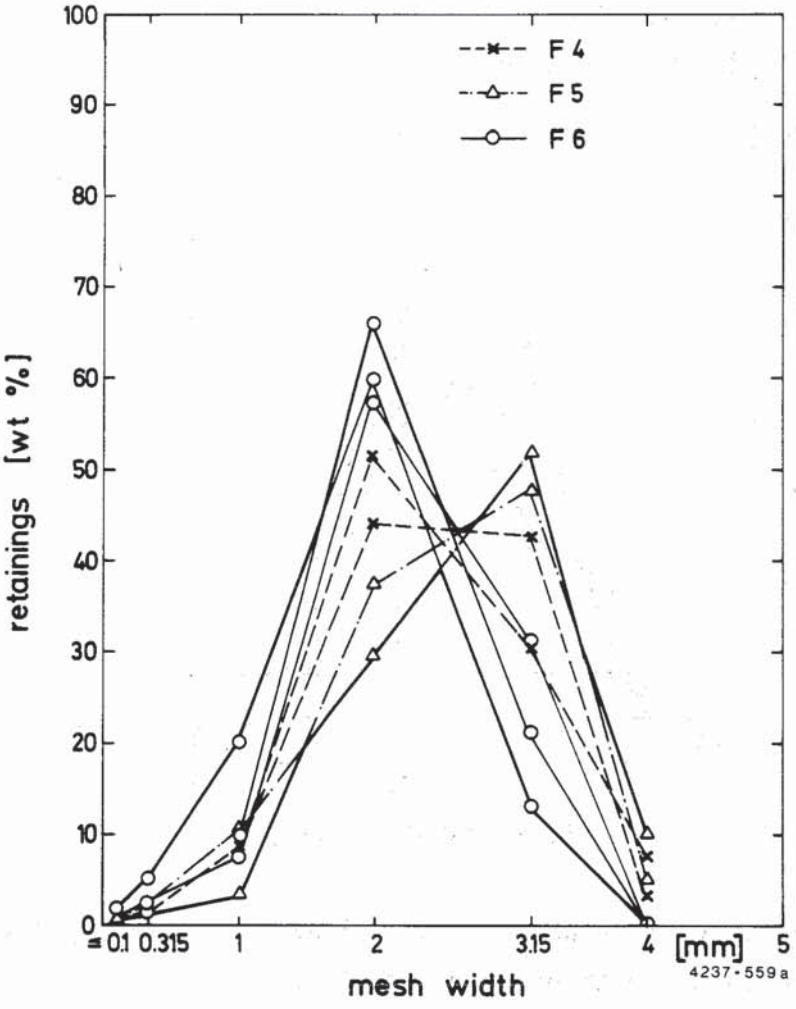

Figure 35: Fuel particle size distribution for test series F (20 000 MWd/t)

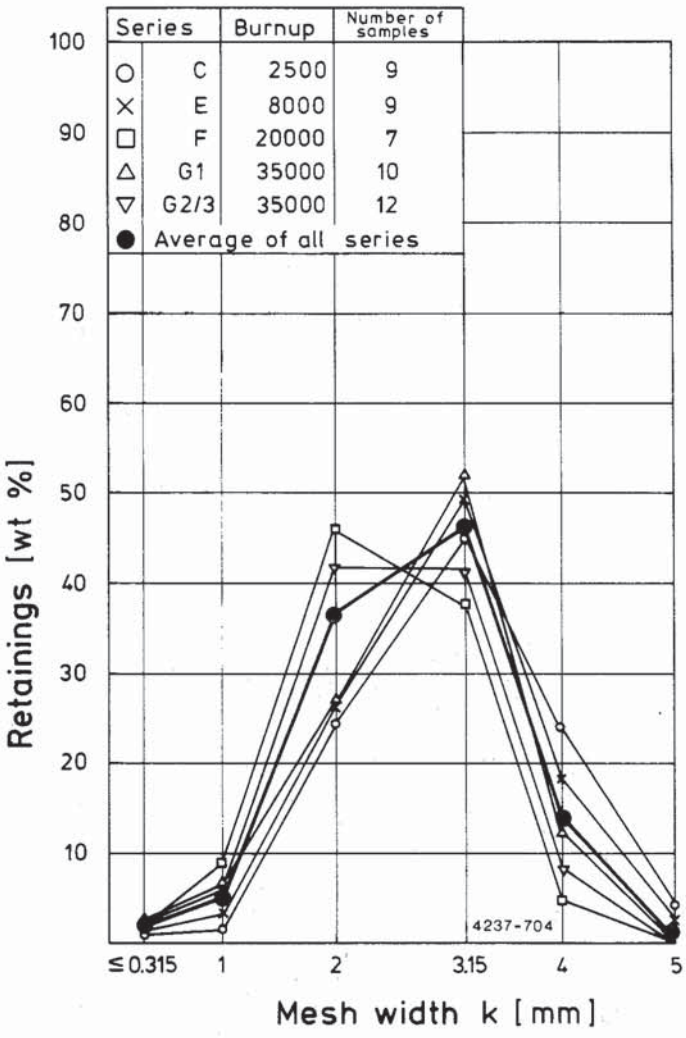

Figure 36: Results from sieve analyses of all samples. Average values per series and average of all series.

6. Cladding microstructure, oxidation, and microhardness

6.1 Cladding microstructure and microstructural evaluation of cladding temperature

The cladding microstructure of all tested rods was mainly determined by the local peak temperatures reached during the transient. Coarse-grained microstructures were observed for the temperature region around the α- to (α + β)-phase boundary and within the single-phase β-range, whereas grain growth was limited for two-phase microstructures. Even for highly strained positions of the tubes the grains were equiaxed due to grain boundary deformation or subsequent recrystallization after the burst.

The appearance of the Zircaloy-4 microstructure was evaluated to estimate the local maximum cladding temperature reached during the in-pile LOCA transients and to quantify azimuthal temperature differences. Within the (α + β) - phase region, the approximation T_{max} [°C] = 820 + 150 · $f_{\beta,max}$ was used to correlate the volume fraction of the prior β-phase ($f_{\beta,max}$) with the corresponding peak temperature. Recrystallization and grain growth indicated temperatures in the high α- and low β-phase regions. The temperatures determined from the microstructures are judged to be reliable within about ± 15 K for the high (α + β) - phase range, where the microstructure is most temperature sensitive, and within about ± 30 K of uncertainty for the low (α + β) - phase temperature range /28, 29/.

From the direct comparison of temperature measurement and microstructural evaluation at positions close to thermocouple welds, no significant difference between the two TC attachment versions A and B (see section 3.3) could be detected. For the average of all rods the absolute values of measurement and microstructural result compared rather well. A comparison of both methods for the burst region is given in Table 15, Appendix A. The accuracy of the temperature measurement based on the comparison of measurement and microstructural evaluation is described in detail in Appendix C.

6.2 Cladding inner and outer oxidation

Compared to the light gray surface of the slightly oxidized cladding of the fuel rods after preirradiation, the appearance after the transients was lighter or darker gray for all nuclear rods and rod simulators. Some of the preirradiated rods (and as an exception one of the simulators) showed patches of very light or even white oxide, observed essentially within the fuel section, especially near the rupture zone but occasionally also along the lower weld seam. Although no correlation with the parameters of the transients was obvious, the behavior must have resulted from slight precorrosion during the preirradiation, leading to defective scales, which were influencing the subsequent oxidation during the transient. This localized breakaway behavior has often been observed but is still not fully explained in the literature /30/. A SEM study revealed the spalling of thin flakes of the white patches of thick oxide which indicated its defective microstructure. Similarly, cracked oxide and spalling was also observed due to largest deformations close to the burst opening. This could account for the small patch of white oxide observed for one of the simulators.

Apart from this localized behavior the oxide layers on the cladding outer surface were dense, adherent, and axially cracked due to cladding deformation. After cladding burst, the continued oxidation formed crack-free, smooth oxide sublayers. In Fig. 37, the local oxide layer thickness of samples from all test series is plotted versus the pertinent maximum cladding temperature. The ZrO_2 layer thickness varied between about 2 and 8 μm for both fresh and irradiated rods, and for rod simulators. This amount of oxidation at the outer cladding surface is comparable to out-of-pile results. Local values of up to about 40 μm in connection with white oxide and results up to about 15 μm for seriously cracked oxide at excessively strained positions were excluded from the plot. With the exception of the early occurrence of localized breakaway behavior, no modification of the steam oxidation at the outer cladding surface in comparison to out-of-pile conditions could be detected /31, 32/. The observed oxidation did not influence the circumferential strain.

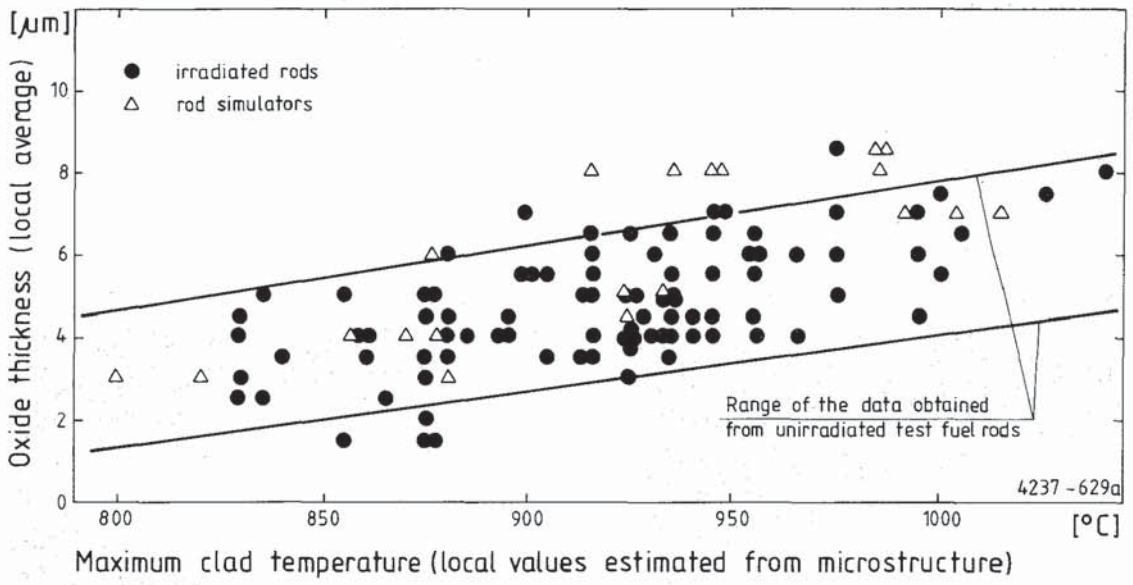

Figure 37: Steam oxidation of the cladding outer surface

The oxidation of the inner surface was primarily caused by steam access after the burst. Close to the burst opening, the thickness of the inner oxide layer was slightly less than the thickness of the outer layer, for fresh rods, simulators and lower burnup rods. However, for irradiated rods of higher burnup (series F and G), the inner oxide layer was significantly thicker than the outer layer (Fig.38). This result can be explained by assuming the growth of a less protective interior scale under an atmosphere of steam, evolved hydrogen, residual fill gas, and volatile fission products. Decisive for this behavior seems to be the sufficient pre-corrosion during the higher burnup preirradiation, which can predetermine the subsequent oxidation in a similar manner as described for the external cladding surface. So, this behavior is not interpreted as a direct influence of in-pile conditions.

The oxide layers were found to decrease in thickness with increasing distance from the burst. Essentially no oxide was found on the inner surface more than about 100 mm from the burst location.

A slight oxidation reaction only was indicated there, and farther away from the burst, by either a thin seam of α-Zr(O) or modification of the border of the bulk ($\alpha + \beta$) - or β- Zircaloy microstructure. This behavior is interpreted by steam consumption near the burst location.

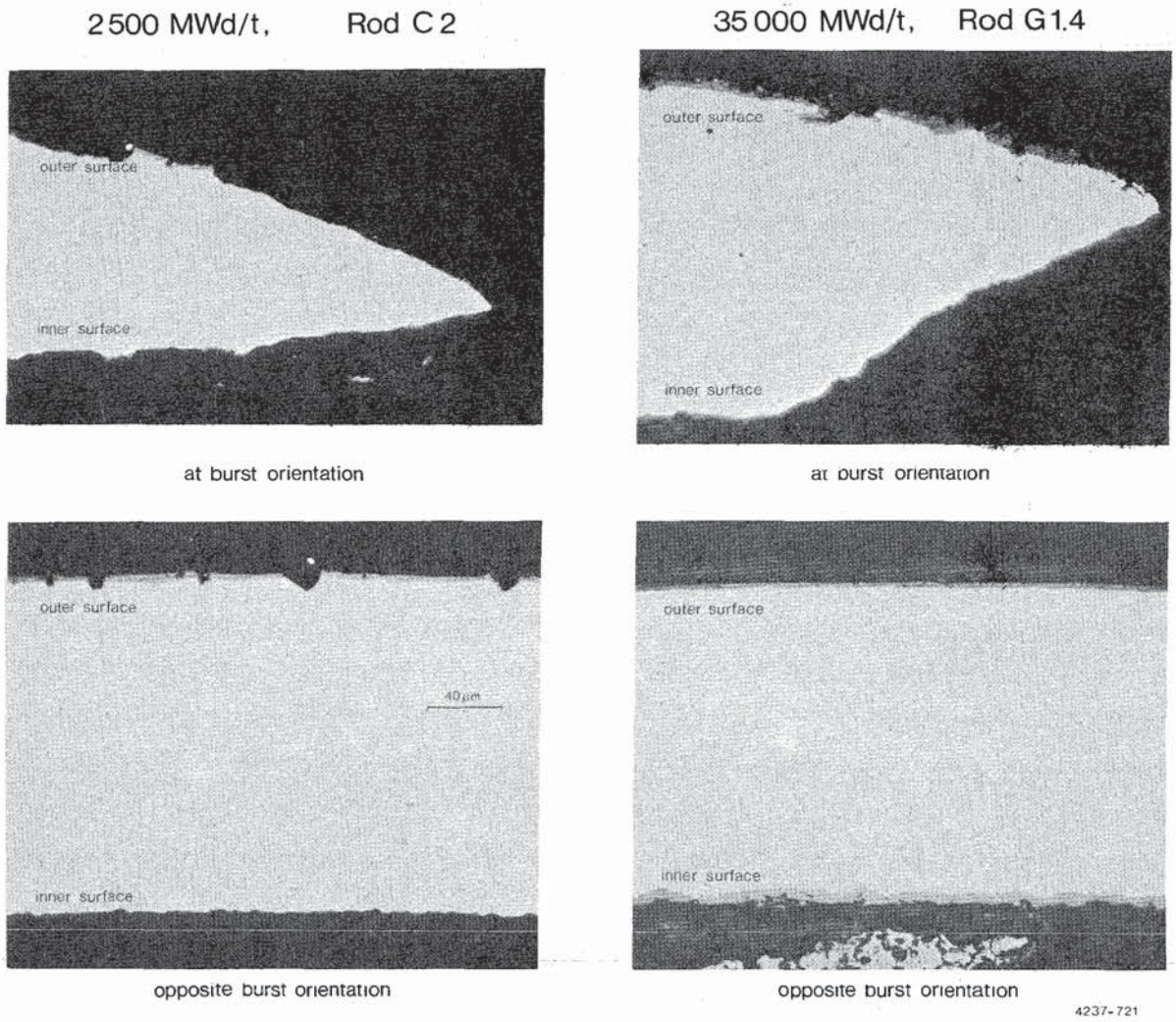

Figure 38: Inner and outer oxide layer at burst elevations of low burnup rod C2 and high burnup rod G 1.4 (with increased oxide thickness)

6.3 Cladding microhardness

Microhardness profiles (Vickers method, 25 g load) could essentially not be correlated with the various factors as oxidation, strain, and subsequent recovery or recrystallization, and peak temperature or microstructure. The average values of the series of all LOCA-tested fuel rods and simulators form a broad common scatter band around the initial hardness of the as-manufactured tubing. After preirradiation a common scatter band of substantially higher hardness level was observed, which is due to irradiation damage. Complete recovery of this damage is indicated during the transient by the preirradiated test rods (Fig. 39).

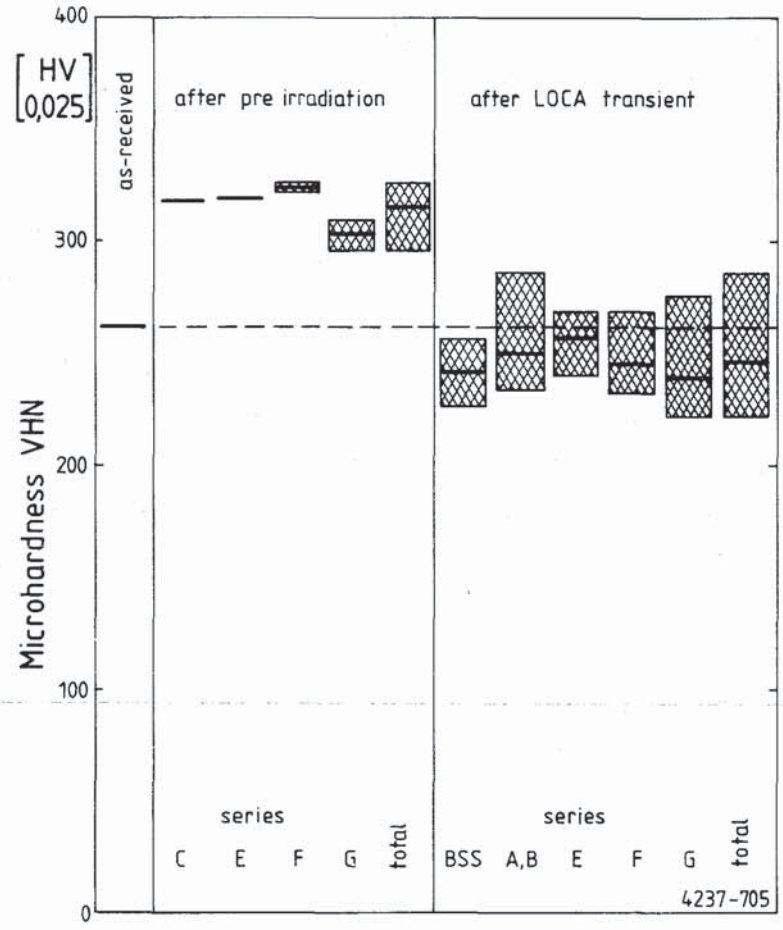

Figure 39: Cladding microhardness VHN for as-received, unirradiated, transient tested (BSS, A, B), and preirradiated and transient tested specimens (E, F, G)

7. Chemical behavior of the fuel and fission products and fission gas release

7.1 Chemical interaction of the fuel and fission products with the zircaloy cladding

Chemical interactions between the UO_2 fuel and the zircaloy were not pronounced. This was because the cladding is generally detached from the fuel during the heatup phase of a LOCA (due to the rod internal overpressure) so that the oxygen of the fuel can be transported from the UO_2 to the zircaloy via the gas phase only, and reactions going via the gas phase are considerably slower than the reactions under conditions of solid contact between fuel and cladding material /33, 34/. In addition, the time at temperature is short for a LOCA transient. Thus, the fuel caused little or no internal cladding oxidation during the transient. The resulting thin oxygen-stabilized α - Zr(O) or oxygen-modified layer had no influence on the burst strain of the cladding.

Also, the volatile fission products, e.g. iodine, did not influence the burst behavior even of the high burnup fuel rods. In all cases the cladding failed in a ductile mode. The fact that no fission product-induced low ductility cladding failure occurred is probably because the fission product concentration at the inner cladding surface was too low. Laboratory experiments demonstrated the cladding failure as a reduction in burst strain for temperatures up to about 850°C /35/. The iodine concentration, in which the cladding failure mode changed from ductile to brittle (critical iodine concentration), depended strongly on temperature /36/. Comparing the critical iodine concentrations determined from out-of-pile tests with the iodine supply in a fuel rod after a burnup of 35 000 MWd/t_u, it is apparent that an influence of iodine on the burst strain can actually be expected to occur only at temperatures $\leq$ 700°C. At higher temperatures, the iodine supply in the fuel rod is lower than the critical iodine concentration required for iodine-induced stress-corrosion cracking of zircaloy cladding /36, 37/.

The many incipient cracks detected at the inner cladding surface of in-pile tested fuel rods confirm that the iodine concentration was not sufficient at the inner surface to cause crack propagation.

Figure 40 shows results of metallographic posttest examinations of fuel rods with burnup of 20 000 and 35 000 MWd/t_u, respectively. On the inner cladding surface, incipient cracks are apparent similar to those observed in the out-of-pile experiments in which the iodine concentration was too low to cause low ductility cladding failure. At axial cladding positions where little or no plastic deformation occurred or in test rods with low burnup fuel, no crack formation on the inner cladding surface was evident (Fig. 40).

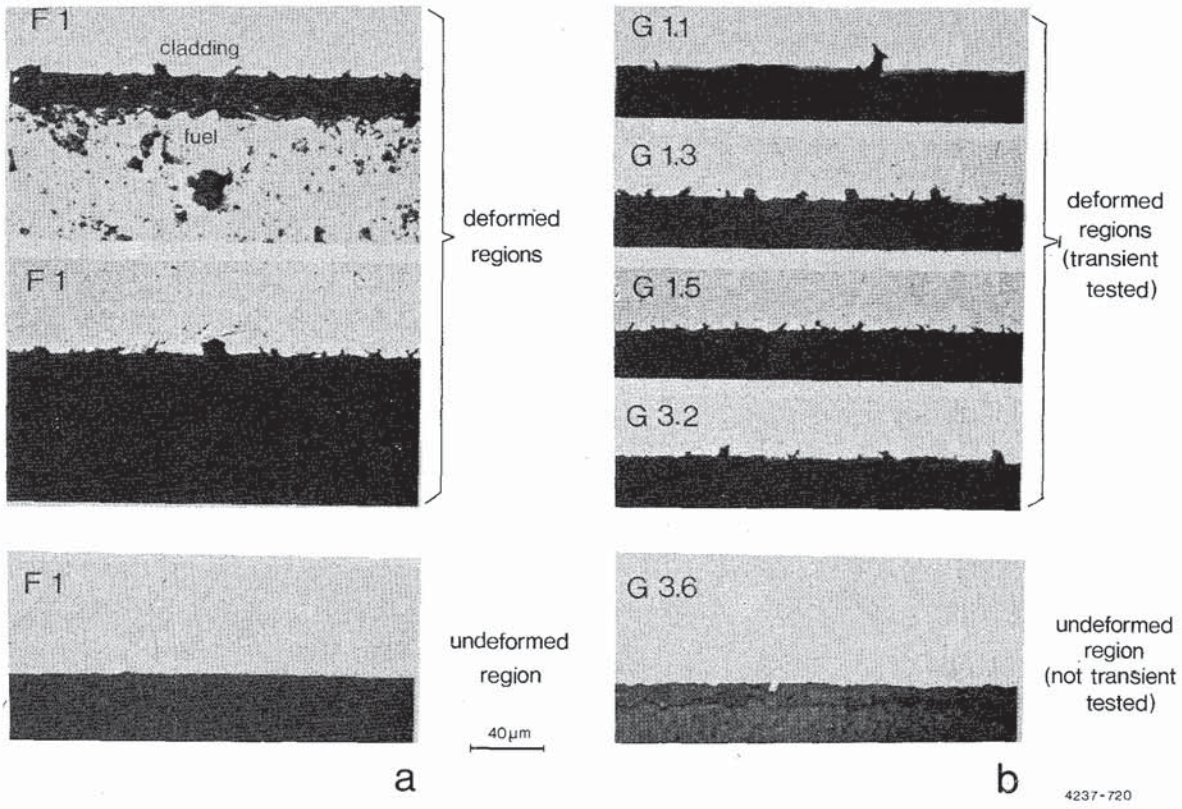

Figure 40: Fuel cladding interfaces of a 20 000 MWd/t_u burnup fuel rod (F1) which failed during an in-pile LOCA transient at 890°C (40a) and of 35 000 MWd/t_u burnup fuel rods which failed during in-pile transients at temperatures ≥ 780°C (40b)

In general, the probability of an iodine-induced low-ductility cladding failure during a LOCA is very small because burst temperatures < 700°C are rather unlikely for commercial PWR fuel rods under LOCA conditions as this would require unrealistically high internal pressures.

7.2 Fuel swelling and fission gas release

The swelling of the fuel was evaluated by measurements of the density in carbon tetrachloride before and after irradiation. During preirradiation the fuel density had increased up to about 3 % burnup. This was due to a volume-averaged maximum swelling rate of about 1 % per 1 at.% burnup and an irradiation-induced densification to about 2 % residual porosity. There was no noticeable swelling during the transient tests.

The fission gas release during the transient could not be measured directly because the test rods ruptured. The release values were deduced from measurements of the retained fission gas /5, 11/.

The fission gas release during preirradiation had increased from < 0.3 % at 0.9 % burnup to 2.7 - 7.8 % at 3.7 - 3.8 % burnup. Most of the retained fission gas was in the matrix.

The fission gas release during the transient tests was insignificant. It was small because only a fraction of the gas accumulated in grain boundaries could escape via cracks in the fuel. The fission gas release during a LOCA is generally small and depends on the fission gas distribution in the fuel which is determined by the steady state irradiation conditions.

8. Results from posttest calculations with the SSYST computer code

Four in-pile tests (A 1.1, A 2.3, B 1.7, and F 4) were posttest calculated using the SSYST-2 computer code /38/. The SSYST code is a modular program system that allows the analysis of a LWR fuel rod during a loss-of-coolant accident /39/. The calculations as a supplementary study on the deformation behavior of the test rods were made in part to investigate the possibilities of the SSYST code using specific thermohydraulic and geometrical test conditions (superheated stagnant steam, flow reversal in the test section) different from reactor conditions. For this reason, some modifications in the modelling of the tests were necessary.

So the heat flux of the test rod surface was calculated by STATI-3, a heat conduction code /40/, on the basis of RELAP-4 calculations for the first six seconds of the transient when convective heat transfer was essential. The heat flux data were input to the SSYST code in form of heat transfer coefficients.

It was learned that the calculated cladding temperatures showed better agreement with the measurements when the thermocouple leads were modelled as additional mass of the cladding, since this additional mass was also to be heated up during the transient, especially at the higher rod elevations where all TC leads were concentrated. Thus the upper end of the rod with six thermocouples experienced a slower temperature rise due to the increased heat capacity compared to the lower elevations with less TC material. The influence of the TC leads on the heatup rate is demonstrated with Fig. 41.

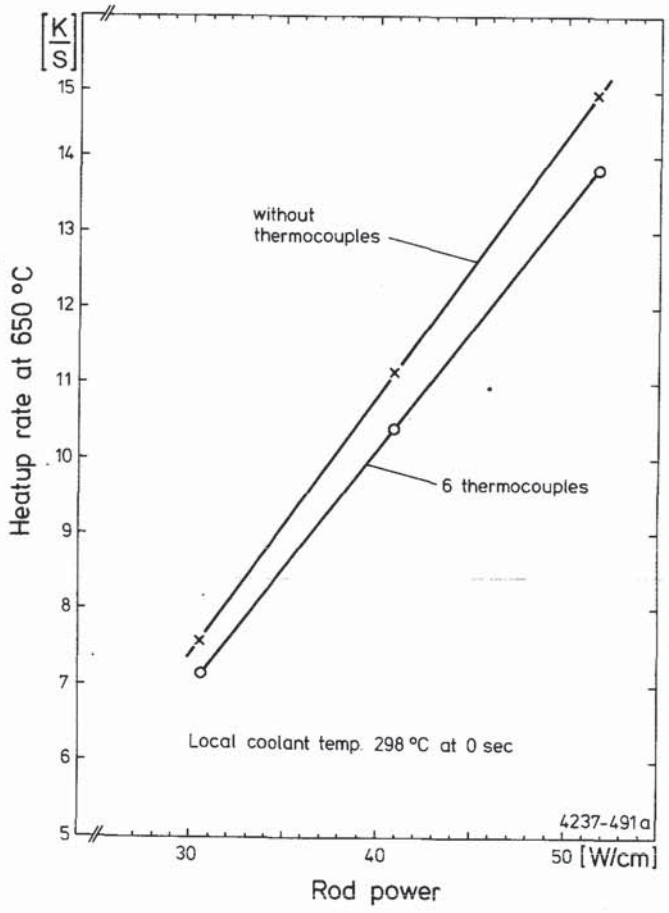

Figure 41: Influence of thermocouple leads on the heatup rate of the cladding, STATI 3 calculation

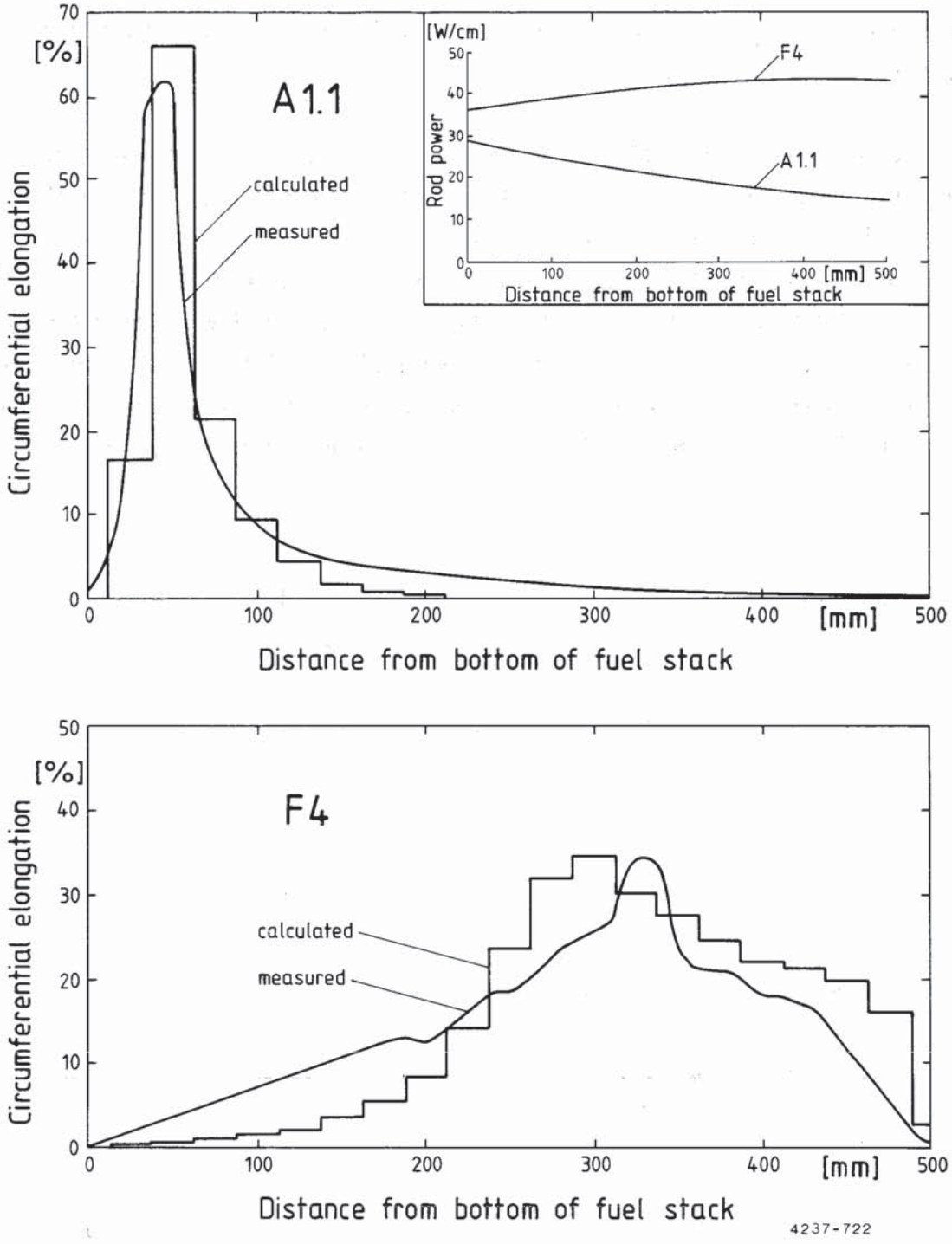

Figure 42: SSYST calculations using the two-dimensional heat transfer model for Tests A 1.1 and F 4 to demonstrate the influence of the axial power profile on the cladding deformation. Comparison with the measured deformation profile.

At upper rod elevations, for instance, with six TC leads passing the rod the heatup rate was reduced by a factor of 1.06 at 40 W/cm.

The strong influence of the power profile on the rod deformation is demonstrated in Fig. 42. The strain profiles of test A 1.1 (peaking factor 1.4) and test F 4 (peaking factor 1.07) are compared in this figure. The power profiles depicted in the same figure were evaluated from measurements, i.e. neutron flux and burnup profiles in connection with the averaged rod powers. Test A 1.1 exhibited an extremely localized balloon influenced by the axial constraint of the cladding by the lower end plug. Figure 42 presents the calculational results obtained with the two-dimensional heat transfer model. The shortcoming of the one-dimensional model in comparison with the 2D model is illustrated for Test A 1.1 in Fig. 43.

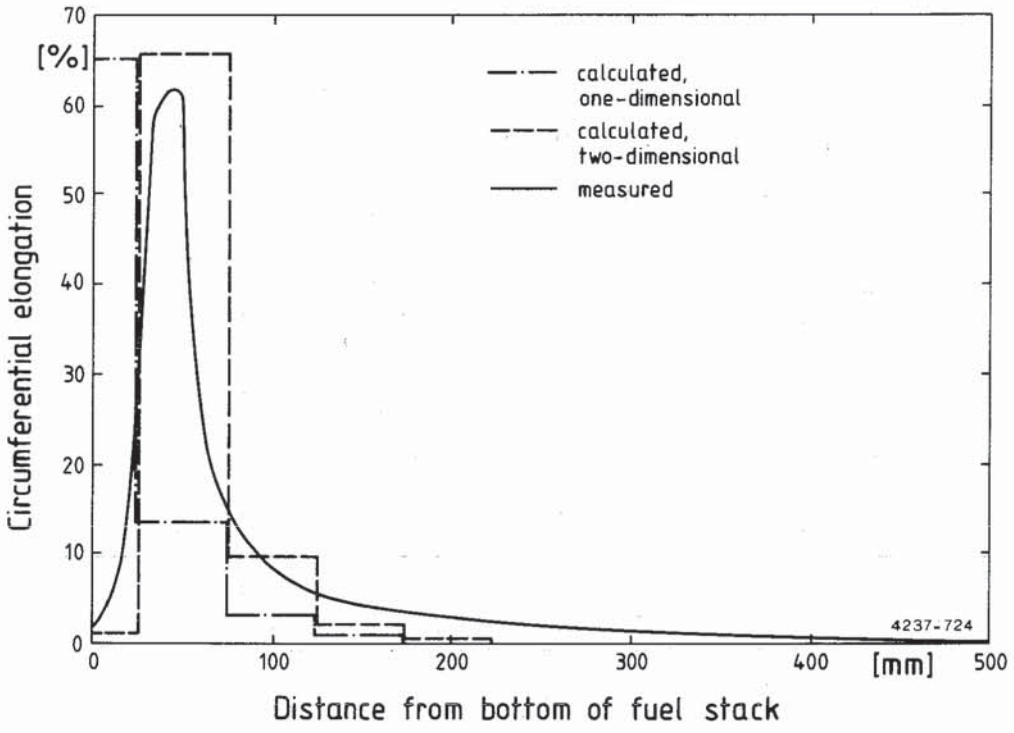

Figure 43: Comparison of one-dimensional and two-dimensional calculations for Test A 1.1 using SSYST computer code

In this figure the number of the axial nodes was decreased. As a consequence, the two-dimensional model results in a different step curve compared to the calculations with a higher number of axial nodes in Figure 42. The one-dimensional heat transfer calculation did not take into account the heat transfer in the axial direction. Particularly at the ends of the active zone and for steep power gradients along the heated length the heat transfer had to be calculated in both directions, radial and axial, to improve the calculated deformation at the ends of the rod.

The improvement in the calculation using the two-dimensional heat transfer model for the cladding strain as a function of time is also illustrated in Fig. 44 for Test A 1.1. The calculated strain curves are to be compared to the burst point in this figure.

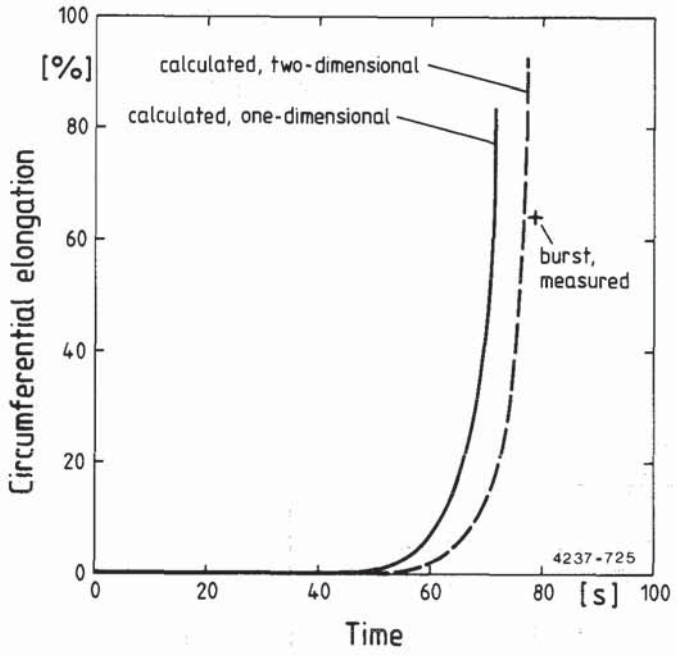

Figure 44: Cladding circumferential elongation vs. time for Test A 1.1; Comparison of one-dimensional and two-dimensional calculations with respect to the time of burst

A similar improvement in the calculations could be reached by linking the axial nodes mechanically, via the moment of flexion. Figure 45 compares one-dimensional calculations of Test A 1.1 with and without a mechanical linkage of the axial nodes. From this comparison it was learned that the influence of edge constraint, that is apparent in the measured deformation profile of Test A 1.1, could be better modelled with the linkage of the axial nodes. For the purpose of the edge effect the number of axial nodes need to be increased at the end of the rod.

The similarity between the calculational results using the node linkage (Fig. 45) and the two-dimensional model (Fig. 43) was accidental. The effect of the thermal linkage of the nodes (two-dimensional heat transfer) extended axially from the end farther into the rod than that of the mechanical linkage model.

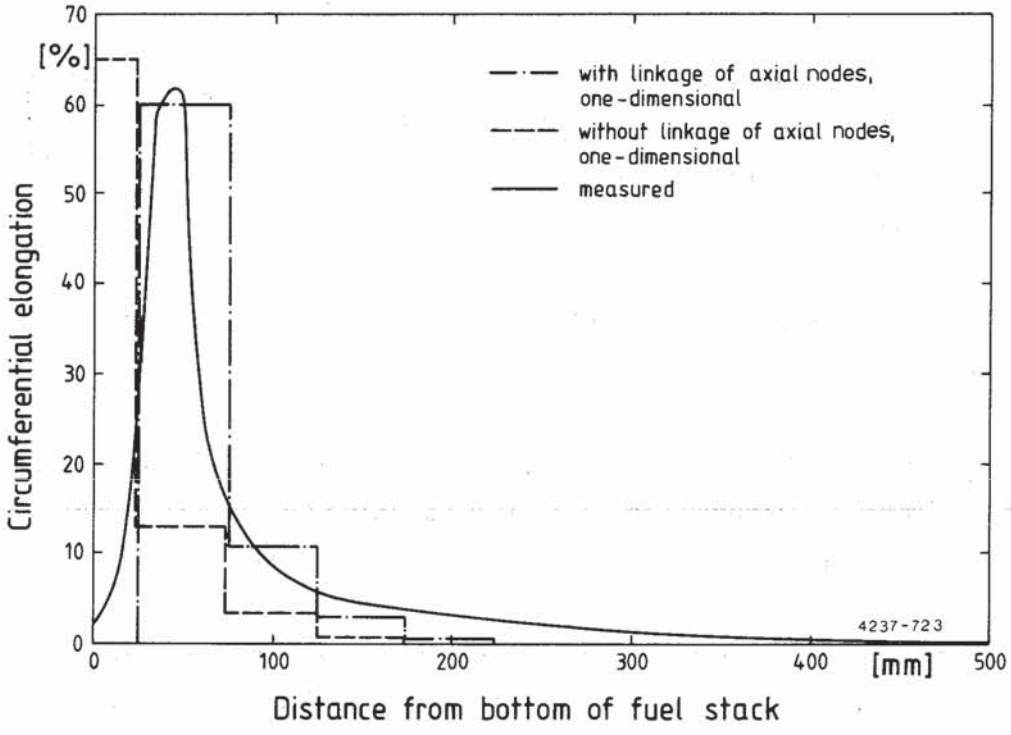

Figure 45: Comparison of SSYST calculations for Test A 1.1 with and without mechanical linkage of axial nodes.

9. Summary of results, conclusion, and discussion

The important results of the FR2 In-pile tests can be summarized as follows:

- All ballooned rods showed some circumferential strain extending over the entire heated length. The deformation profile was influenced by the axial power profile and locally by the thermocouple welding points.

- With two exceptions the test rods burst at the location of maximum total circumferential elongation (TCE), which was located at or near the peak power position.

- The burst data of the tests with nuclear fuel rods (burst temperature, burst pressure, and burst strain) were similar to the results obtained with own tests using electrically heated simulators and those from various out-of-pile experiments. No influence of burnup on the burst data was detected.

- The tests with previously irradiated rods resulted in fragmented fuel pellets in the rod sections with major deformation. The pellet fragments relocated outward and downward, filling the space in the fuel rod created by the balloon.

- Fuel pellet fragmentation did not affect the cladding deformation process.

- Microstructural evaluation of the maximum cladding temperature indicated azimuthal temperature differences between 0 and about 100 K. Microstructure essentially confirmed the temperature measurements.

- Steam oxidation of the cladding outer surface was comparable to out-of-pile results with the exception of occasional observations of localized excessive oxide growth for the preirradiated rods.

- Inner oxide layers of considerable thickness were only observed near the burst position and were caused by steam access via the rupture

opening and steam consumption in its vicinity. In the fresh and the low burnup rods, the thickness of the inner oxide layer was slightly less than that of the outer layer. However, in the high burnup rods, the inner oxide layer was significantly thicker than the outer layer. This is interpreted by the growth of defective scales during preirradiation to high burnup.

- No influence of fission products on cladding burst strain was detected.

- Fission gas release during the LOCA transient was negligible. It was caused primarily by microcrack formation in the fuel. Fuel swelling was negligible, too.

From these results it is concluded that there is no influence of a nuclear environment on the mechanisms of fuel rod failure during a LOCA.

This conclusion is strictly valid only within the boundary conditions of the FR2 tests. Specific limitations are discussed below:

1) The test rods were irradiated in the FR2 research reactor at linear heat generation rates typical for power reactors (PWR), but with lower cladding and fuel surface temperatures, and lower coolant pressure. However, the appearance of the cracked fuel (number, size, and form of the fuel fragments) was reactor-typical. Because of the lower coolant pressure, the cladding did not creep down onto the fuel. For nominal gap size, the fuel-cladding gap was therefore too wide so that the gap closure occurred later. To compensate for this, some test rods were fabricated with a smaller gap. However, no effect of gap width on the deformation and burst data was found. This confirms analytical results, that gap size is of relatively small importance during the heatup phase of a LOCA. Therefore, the test rods irradiated in the FR2 reactor may be regarded as sufficiently typical of power reactor rods.

2) The FR2 tests simulated the second heatup phase of a LOCA without the preceding blowdown or subsequent reflooding phases. For the typical cold-leg break LOCA as defined by licensing requirements (early DNB and no rewetting during blowdown), the blowdown phase is of minor importance with respect to fuel failure by ballooning and rupture.

During the heatup to the first cladding temperature peak, in the blowdown phase, coolant pressure is still relatively high, so that internal overpressure does not occur. At the end of the blowdown phase, when the rod internal pressure clearly exceeds the coolant pressure, cladding temperature is relatively low. Thus, the probability of fuel rod failure is much lower during the blowdown phase than during the subsequent second heatup phase, provided that internal test rod pressures are not chosen unrealistically high for fuel behavior tests.

3) Comparison of out-of-pile tests with and without reflooding /14/ had shown that the cooling effect of two-phase flow during reflooding increased azimuthal cladding temperature differencess and thus reduced cladding deformation. The FR2 tests were performed without reflooding. However, azimuthal temperature variations of up to 80 K for the nuclear rods and up to 100 K for the electrically heated simulators, respectively, were determined from microstructural examination of the cladding. Therefore, substantial azimuthal temperature differences may develop across nuclear rods during heatup even without convective heat transfer caused by reflooding.

In summary, the limitations of the FR2 tests did not affect the conclusion drawn from the test results, that there is no influence of a nuclear environment on the mechanisms of fuel rod failure during a LOCA, initiated by a guillotine break of a main coolant inlet pipe in a reactor.

10. References

/1/ F. Erbacher, H.J. Neitzel, and K. Wiehr,
"Deformation Mechanism of Zircaloy Fuel Cladding in a LOCA and Interaction with the Emergency Core Cooling",
Trans. Am. Nucl. Soc., 31:336-339 (1979)

/2/ A.A. Bauer et al., "Evaluating Strength and Ductility of Irradiated Zircaloy", Quarterly Progress Report
January - March, 1978,
NUREG / CR-0085, BMI-2000 (1978)

/3/ R.H. Chapman, J.M. Cathcart, and D.O. Hobson, "Status of Zircaloy Deformation and Oxidation Research at Oak Ridge National Laboratory", presented at Specialists Meeting on the Behavior of Water Reactor Fuel Elements under Accident Conditions, September 13-16, 1976, Spatind, Norway.
USERDA Report CONF - 760997-2, NTIS (1976)

/4/ H.M. Chung and T.F. Kassner, "Deformation Characteristics of Zircaloy Cladding in Vacuum under Steam and Transient-Heating Conditions; Summary Report", ANL-77-31,
NUREG/CR-0344 (1978)

/5/ E.H. Karb et al., "KfK In-Pile Tests on LWR Fuel Rod Behavior During the Heatup Phase of a LOCA",
KfK 3028 (1980)

/6/ E. Karb, "In-Pile Tests at Karlsruhe of LWR Fuel-Rod Behavior During the Heatup Phase of a LOCA",
Nuclear Safety, 21-1, 26 (1980)

/7/ M. Fischer and M.F. Osborne, "LWR Fuel-Behavior Research in the Federal Republic of Germany, Nuclear Safety,
19(2): 176-188 (1978)

/8/ L. Sepold, E. Karb, "In-Pile Tests on LWR Fuel Rod Behavior under LOCA Conditions in the Karlsruhe FR2 Reactor", Proceedings of CSNI Specialist Meeting on Safety Aspects of Fuel Behavior in Off-Normal and Accident Conditions, Helsinki, Finland (1980) 361-371

/9/ L. Sepold, E.H. Karb, "Ergebnisse der FR2-In-Pile-Experimente zum LWR-Brennstabverhalten unter LOCA-Bedingungen", in Tagungsbericht der Jahrestagung Kerntechnik 81, Deutsches Atomforum e.V., Bonn (1981), 243-247

/10/ E.H. Karb et al., "Results of the FR2 In-Pile Tests on LWR Fuel Rod Behavior", Proceedings of the Topical Meeting on Reactor Safety Aspects of Fuel Behavior, ANS, Sun Valley (1981) vol. 2, 133-144

/11/ E.H. Karb et al., "LWR Fuel Rod Behavior During Reactor Tests Under Loss-of-Coolant Conditions: Results of the FR2 In-Pile Tests", Journal of Nuclear Materials 107 (1982) 55-77

/12/ M. Prüßmann, E.H. Karb, L. Sepold, "FR2-In-Pile-Versuche zum LWR-Brennstabverhalten mit elektrisch beheizten Brennstabsimulatoren", KfK 3255 (1982)

/13/ W. Leiling, "Hülltemperaturmessung mit Thermoelementen an vorbestrahlten LWR-Brennstab-Prüflingen", KfK 3100 (1981)

/14/ K. Wiehr, F.J. Erbacher and H.J. Neitzel, "Influence of Thermohydraulics on Fuel Rod Behavior in a LOCA", Proceedings of the CSNI Specialist Meeting on Safety Aspects of Fuel Behavior in Off-normal and Accident Conditions, Helsinki, Finland (1980) 59-73

/15/ L. Sepold, E.H. Karb and M. Prüßmann, "Ergebnisse der In-Pile-Experimente zum LWR-Brennstabverhalten beim LOCA mit nicht vorbestrahlten Brennstäben", KfK 3098 (1981)

/16/ E. Karb, M. Prüßmann and L. Sepold, "In-Pile Experimente zum Brennstabverhalten beim Kühlmittelverlust-Störfall, Bericht über die Versuchsserie F", KfK 2956 (1980)

/17/ M. Prüßmann, E.H. Karb and L. Sepold, "In-Pile Experimente zum Brennstabverhalten beim Kühlmittelverlust-Störfall, Bericht über die Versuchsserie G1" KfK 3061 (1980)

/18/ L. Sepold, E.H. Karb, M. Prüßmann, "In-Pile-Experimente zum Brennstabverhalten beim Kühlmittelverlust-Störfall, Bericht über die Versuchsserie G 2/3", KfK 3099 (1981)

/19/ M. Prüßmann, E.H. Karb, L. Sepold, "In-Pile-Experimente zum Brennstabverhalten beim Kühlmittelverlust-Störfall, Bericht über die Versuchsserie C", KfK 3195 (1982)

/20/ L. Sepold, E.H. Karb, M. Prüßmann, "In-Pile-Experimente zum Brennstabverhalten beim Kühlmittelverlust-Störfall, Bericht über die Versuchsserie E", KfK 3345 (1982)

/21/ R.H. Chapman, "Multirod Burst Test Program Progress", Report for January - March 1978, NUREG / CR-0225, ORNL / NUREG / TM-217 (1978)

/22/ F. Erbacher, "Verhalten der Brennelemente beim Kühlmittelverlust-Störfall und Wechselwirkung mit der Kernnotkühlung", KfK 2691 (1978)

/23/ F. Erbacher, H.J. Neitzel, K. Wiehr, "Studies on Zircaloy Fuel Clad Ballooning in a LOCA, Results of Burst Tests with Indirectly Heated Fuel Rod Simulators", Proceedings of the Fourth International Conference on Zirconium in the Nuclear Industry, ASTM, June 26-29, 1978 Stratford-on-Avon, England, ASTM-STP 681

/24/ J.M. Broughton, R.K. McCardell, and P.E. MacDonald, "Comparison of the Cladding Deformation measured during the Power Burst Facility Loss-of-Coolant Accident In-Pile Experiments with Recent Oak Ridge National Laboratory Out-of-Pile Results", presented at the Enlarged Halden Program Group Meeting on Water Reactor Fuel Performance, Hanklo, Norway, June 14-19, 1981

/25/ J.M. Broughton, R.K. McCardell and P.E.MacDonald, "Comparison of the Cladding Deformation Measured During the Power Burst Facility Loss-of-Coolant Accident In-Pile Experiments with Recent Oak Ridge National Laboratory Out-of-Pile Results", Proceedings of Topical Meeting on Reactor Safety Aspects of Fuel Behavior, Sun Valley, Idaho (1981) vol. 2, 145-162

/26/ F.J. Erbacher, "LWR Fuel Cladding Deformation in a LOCA and its Interaction with the Emergency Core Cooling", Proceedings of Topical Meeting on Reactor Safety Aspects of Fuel Behavior, Sun Valley, Idaho (1981) vol. 2, 100-113

/27/ D.O. Hobson, P.L. Rittenhouse, "Deformation and Rupture Behavior of Light-Water Reactor Fuel Cladding", ORNL-4727 (1971)

/28/ P. Hofmann et al., "In-Pile-Experimente zum Brennstabverhalten beim Kühlmittelverlust-Störfall. Ergebnisse der zerstörenden Nachuntersuchungen der Versuchsserie F (22 000 MWd/t_U)", KfK 3288 (1982)

/29/ P. Hofmann et al., "In-Pile-Experimente zum Brennstabverhalten beim Kühlmittelverlust-Störfall. Ergebnisse der zerstörenden Nachuntersuchungen der Versuchsserie G (35 000 MWd/t_u)", KfK 3433 (to be published in 1983)

/30/ G. Schanz, S. Leistikow, "ZrO_2-Scale Degradation during Zircaloy 4 High Temperature Steam Exposure. Microstructural Mechanism and Consequences for PWR Safety Analysis", Proceedings of Topical Meeting on Reactor Safety Aspects of Fuel Behavior, Sun Valley, Idaho (1981), vol. 2, 342-353

/31/ S. Leistikow, G. Schanz, and H.v. Berg, "Kinetik und Morphologie der isothermen Dampf-Oxidation von Zircaloy-4 bei 700-1300 °C", KfK 2587 (1978)

/32/ S. Leistikow, G. Schanz, and H.v. Berg, "Untersuchungen zur temperatur-transienten Dampfoxidation von Zircaloy-4-Hüllmaterial unter hypothetischen DWR-Kühlmittelverlust-Störfallbedingungen", KfK 2810 (1979)

/33/ P. Hofmann, C. Politis, "The Kinetics of the UO_2/Zircaloy reactions at high temperatures", J. of Nucl. Mat., 87 (1979) 375-397

/34/ P. Hofmann, D. Kerwin, "Preliminary Results of UO_2/Zircaloy Experiments under Severe Fuel Damage Conditions", RES Mechanica, 5 (1982) 293-308

/35/ P. Hofmann, "Influence of iodine on the burst strain of Zircaloy-4 cladding tubes under simulated reactor accident conditions", J. of Nucl. Mat., 87 (1979) 49-69

/36/ P. Hofmann, J. Spino, "Determination of the critical iodine concentration for SCC failure of Zircaloy-4 tubing between 500 and 900°C",
J. of Nucl. Mat., 107 (1982) 297-310

/37/ P. Hofmann, J. Spino, " Can one expect low ductility failure of Zircaloy-4 tubing due to iodine-induced SCC in a LOCA transient?", Proceedings of Topical Meeting on Reactor Safety Aspects of Fuel Behavior,
Sun Valley, Idaho (1981) , vol. 2, 410-421

/38/ K. Wagner, A. Scherer, "Nachrechnung einiger FR2-In-Pile-Versuche mit SSYST-2
KfK 3144 (to be published in 1983)

/39/ R. Meyder, "SSYST-2, Eingabebeschreibung und Handhabung",
KfK 2966 (1980)

/40/ K. Wagner, "STATI - Ein eindimensionales instationäres Wärmeleitungsprogramm (FORTRAN) für Zylindergeometrie",
KfK 3348 (in preparation)

Appendix A

Data Tables

Contents:

Table 8: Pretest fuel rod dimensions

Test	Rod No.	Fuel rod length	Active zone			Void volumes				Cladding dimensions							Pellet OD		Cold diametral gap
										OD		ID		Wall thickness					
			length	weight	fuel density	plenum	dishing	gap	total[a]	mean	stand. dev.	mean	stand. dev.	W_{max}	W_{min}	eccentricity [b]	mean	stand. dev.	
		mm	mm	g	g/cm³	cm³	cm³	cm³	cm³	mm	µm	mm	µm	mm	mm	%	mm	µm	mm
A1.1	15	973,02	497,80	330,5	10,45	16,086	0,780	1,552	30,642	10,758	3,13	9,303	3,87	0,744	0,711	2,1	9,112	2,05	0,191
A1.2	14	972,93	498,07	330,5	10,45	15,997	0,782	1,495	30,524	10,753	2,89	9,294	3,96	0,746	0,714	2,2	9,112	2,14	0,182
A2.1	16	972,86	497,79	330,0	10,43	15,997	0,750	1,469	30,466	10,748	1,95	9,291	2,68	0,746	0,710	2,5	9,110	1,43	0,181
A2.2	17	972,98	496,97	329,5	10,43	16,080	0,745	1,466	30,541	10,750	2,50	9,287	3,55	0,749	0,714	2,5	9,108	1,37	0,179
A2.3	18	972,90	496,94	329,5	10,43	16,070	0,768	1,508	30,596	10,751	2,42	9,292	2,53	0,747	0,711	2,3	9,108	1,01	0,184
B1.1	20	972,87	497,84	330,0	10,43	16,030	0,741	1,560	30,581	10,737	1,97	9,299	3,20	0,742	0,695	3,3	9,109	1,55	0,190
B1.2	21	972,84	497,45	330,0	10,43	16,070	0,750	1,567	30,637	10,733	3,02	9,299	4,52	0,740	0,692	3,5	9,108	2,68	0,191
B1.3	22	972,90	497,96	330,0	10,44	16,015	0,750	1,535	30,550	10,746	3,36	9,295	3,67	0,751	0,703	3,6	9,108	2,07	0,187
B1.4	23	972,88	498,13	330,0	10,42	16,078	0,754	1,511	30,593	10,750	2,56	9,294	3,47	0,753	0,703	3,5	9,110	1,93	0,184
B1.5	24	972,89	496,90	329,0	10,44	16,144	0,750	1,582	30,726	10,757	3,11	9,301	4,21	0,750	0,706	3,0	9,108	1,45	0,193
B1.6	25	972,94	497,48	329,0	10,46	16,031	0,750	1,509	30,540	10,746	2,42	9,291	3,39	0,741	0,714	1,9	9,107	1,49	0,184
B1.7	30	972,89	498,08	329,5	10,41	16,029	0,763	1,568	30,610	10,751	2,56	9,298	4,27	0,734	0,721	1,0	9,107	1,42	0,191
B3.1	1	972,94	499,40	333,5	10,42	15,927	0,782	1,270	30,229	10,746	2,96	9,298	4,43	0,740	0,704	2,5	9,144	1,12	0,154
B3.2	2	972,97	499,20	334,0	10,42	15,950	0,782	1,311	30,293	10,747	2,25	9,303	3,56	0,740	0,703	2,6	9,144	0,76	0,159
C1	56	972,92	497,70	330,0	10,47	16,015	0,745	1,543	30,562	10,760	2,13	9,295	3,35	0,746	0,718	2,2	9,107	1,39	0,188
C2	57	972,90	497,85	330,0	10,45	16,024	0,754	1,532	30,560	10,759	2,52	9,297	4,10	0,746	0,715	1,8	9,107	1,73	0,190
C3	59	972,85	497,00	329,5	10,42	16,147	0,741	1,616	30,754	10,758	2,29	9,309	4,01	0,736	0,712	1,5	9,112	1,88	0,197
C4	60	972,80	497,50	330,0	10,44	16,108	0,759	1,617	30,734	10,755	3,29	9,308	5,42	0,733	0,712	1,4	9,111	1,97	0,197
C5	63	972,92	497,10	329,5	10,42	16,033	0,741	1,582	30,606	10,753	2,54	9,299	3,96	0,735	0,718	1,4	9,106	1,18	0,193
C6	62	972,91	498,30	330,5	10,45	16,167	0,764	1,640	30,821	10,759	2,39	9,306	3,80	0,736	0,717	1,4	9,106	1,08	0,200
E1	44	972,06	496,66	329,0	10,42	16,103	0,750	1,531	30,634	10,739	2,63	9,292	4,29	0,739	0,705	2,3	9,105	1,23	0,187
E2	45	972,81	496,70	329,0	10,43	16,144	0,750	1,606	30,750	10,745	3,86	9,301	5,52	0,740	0,705	2,3	9,105	1,47	0,196
E3	46	972,95	497,05	329,0	10,43	16,104	0,745	1,656	30,755	10,755	3,54	9,307	4,24	0,740	0,709	2,3	9,105	1,33	0,202
E4	47	973,00	497,35	329,0	10,42	16,099	0,750	1,641	30,740	10,752	2,69	9,306	4,22	0,739	0,707	2,2	9,106	0,98	0,200
E5	48	972,92	496,82	328,5	10,42	16,120	0,754	1,615	30,739	10,746	2,65	9,303	3,49	0,738	0,704	2,3	9,106	1,52	0,197
E6	49	972,87	497,20	329,5	10,45	16,099	0,759	1,664	30,772	10,756	3,52	9,306	5,31	0,731	0,719	0,8	9,103	1,31	0,203
F1	37	972,87	497,84	329,5	10,44	16,101	0,758	1,708	30,817	10,765	2,63	9,314	4,36	0,753	0,700	3,7	9,106	1,30	0,208
F2	38	972,86	497,35	329,5	10,44	16,151	0,745	1,674	30,820	10,763	2,81	9,310	4,43	0,754	0,700	3,9	9,106	1,09	0,204
F3	39	972,86	497,20	329,5	10,44	16,107	0,753	1,624	30,734	10,756	3,75	9,304	4,99	0,753	0,700	3,7	9,106	1,13	0,198
F4	40	972,97	497,26	329,5	10,44	16,110	0,750	1,599	30,709	10,755	3,48	9,301	5,11	0,744	0,711	2,5	9,106	1,24	0,195
F5	43	972,87	498,45	330,5	10,45	16,031	0,750	1,644	30,675	10,751	2,58	9,306	4,34	0,739	0,706	2,2	9,106	0,95	0,200
F6	41	972,98	497,32	329,5	10,45	16,120	0,752	1,624	30,746	10,758	3,68	9,303	5,60	0,745	0,714	2,1	9,105	1,32	0,198
G1.1	3	972,95	498,70	333,0	10,42	16,018	0,773	1,302	30,343	10,748	2,14	9,303	3,29	0,738	0,707	2,2	9,145	2,54	0,158
G1.2	4	972,98	499,40	334,0	10,42	15,950	0,753	1,271	30,224	10,747	2,82	9,303	4,15	0,740	0,705	2,2	9,149	3,25	0,154
G1.3	5	973,04	500,30	335,0	10,43	15,895	0,757	1,306	30,208	10,749	2,42	9,306	3,97	0,739	0,706	2,2	9,148	2,54	0,158
G1.4	7	972,94	500,30	335,0	10,43	15,879	0,777	1,239	30,145	10,752	2,92	9,295	4,06	0,742	0,715	2,1	9,145	2,64	0,150
G1.5	9	972,91	500,00	334,5	10,44	15,897	0,775	1,272	30,194	10,758	3,47	9,299	4,38	0,740	0,716	1,9	9,145	2,28	0,154
G1.6	8	973,03	500,30	335,0	10,45	15,850	0,770	1,264	30,134	10,756	3,36	9,296	3,75	0,740	0,718	1,5	9,143	1,13	0,153
G2.1	35	972,88	498,20	330,0	10,45	16,074	0,753	1,636	30,713	10,756	3,15	9,308	4,39	0,756	0,691	4,4	9,109	1,45	0,199
G2.2	36	972,91	497,94	329,5	10,44	16,042	0,768	1,593	30,653	10,744	3,44	9,301	4,64	0,755	0,689	4,6	9,107	1,14	0,194
G3.1	12	972,89	499,90	334,5	10,44	15,900	0,755	1,197	30,102	10,746	2,40	9,292	2,80	0,746	0,708	2,6	9,147	3,28	0,145
G3.2	11	972,95	502,80	336,0	10,45	15,728	0,768	1,196[c]	29,942	10,742	3,34	9,300[c]	—	0,725	0,718	—	9,156	4,06	0,150[c]
G3.3	10	972,93	500,40	335,5	10,45	15,769	0,763	1,173	29,955	10,746	2,90	9,293	3,35	0,745	0,708	2,6	9,151	4,40	0,142
G3.6	6	973,01	499,45	334,0	10,43	15,940	0,760	1,279	30,229	10,747	2,49	9,301	4,44	0,743	0,704	2,8	9,146	2,52	0,155

(a) Total = plenum, dishing, and gap volumes plus volumes of tubing and pressure transducer (12.25 cm³)

(b) Eccentricity = $\frac{W_{max}-W_{min}}{W_{max}+W_{min}}$, evaluated for elevation of rupture plane

(c) Nominal data

Table 9: Irradiation histories

Series	Accumulated exposure time	Average rod power per cycle	Accumulated burnup	Shutdowns during irradiation
—	d	W/cm	MWd/t_u	—
C	37,2	394,0	2410	0
	19,6	371,9	1249	
E	56,4	357,8	3508	12
	96,3	322,3	5714	
	132,9	347,3	7895	
	37,3	360,1	2309	
	79,4	423,7	5377	
	122,2	384,6	8206	
	164,3	373,5	10909	
F	194,5	368,9	12825	32
	237,5	344,4	15371	
	274,7	345	17577	
	315,5	301,9	19695	
	337,8	250	20653	
	45	424,2	3255	
	89,3	424,2	6458	
	134,1	377	9337	
	179,3	373	12212	
	216,8	489,5	15342	
	259,1	401,5	18237	
	301,7	364,8	20888	
G1	343,8	347,3	23380	53
	374	318,7	25022	
	417	307,7	27278	
	454,2	293,1	29137	
	495	277,4	31066	
	538,4	320,5	33439	
	572,4	271	35010	
	595,7	247,7	35993	
	44,0	360,1	2718	
	89,0	331,0	5272	
	126,3	387,0	7750	
	168,7	456,9	11072	
	211,2	438,2	14268	
	253,3	400,9	17163	
	283,5	211,5	18269	
G2/3	326,5	408,5	21275	62
	363,6	303,6	23210	
	404,4	261,1	25040	
	447,8	266,9	27028	
	481,8	243,6	28446	
	505,1	215,6	29306	
	535,5	208,0	30391	
	573,2	184,3	31584	
	609,2	180,7	32701	
	650,3	184,2	34001	

Table 10: In-pile test rod power data

Test	Local rod power derived from temperature rise at thermocouple location						at rupture midplane	Power derived from enthalpy balance	Flux profile $\frac{\varnothing_{max}}{\varnothing}$	Elevation of max.	Power profile $\frac{N_{max}}{N}$	Elevation of max.
	T131	T132	T133	T134	T135	T136						
	W/cm	W/cm	W/cm	W/cm	W/cm	W/cm	W/cm	W/cm		mm [c]		mm [c]
A1.1	31,2	29,0	25,6	24,4	19,2	—	31	—	1,406	0	1.406	0
A1.2	—	35,5	44,7	46,3	—	—	42	42,5	1,055	400	1,055	400
A2.1	71,0	66,0	66,0	71,0	74,0	—	71	54,0	1,012	300	1,012	300
A2.2	48,1	48,1	48,1	47,8	50,9	—	48	40,6	1,031	50	1,031	50
A2.3	50,9	46,9	47,8	46,3	47,8	41,6	51	42,8	1,017	50	1,017	50
B1.1	58,6	56,5	64,8	65,4	52,4	51,2	65	40,1	1,010	100	1,010	100
B1.2	38,5	37,0	39,2	35,5	38,5	35,5	36	39,1	1,011	100	1,011	100
B1.3	49,3	49,3	49,3	46,3	50,3	45,3	49	39,3	1,010	300	1,010	300
B1.4	42,2	38,2	40,1	38,5	38,5	39,2	40	41,7	1,023	100	1,023	100
B1.5	39,2	37,0	37,0	35,5	35,5	35,5	39	41,4	1,013	25	1,013	25
B1.6	36,0	36,0	36,0	36,0	35,2	33,6	36	40,8	1,011	50	1,011	50
B1.7	38,7	43,7	44,5	38,3	—	—	(43)	56,7	1,025	25	1,025	25
B3.1	40,4	41,6	41,0	41,6	40,4	39,2	42	39,7	1,008	250	1,008	250
B3.2	48,1	48,1	48,4	47,2	45,3	45,6	48	40,6	1,009	300	1,009	300
C1	49,5	47,2	44,5	43,7	44,2	44,5	50	45,0	1,009	125	1,009	125
C2	45,5	45,2	43,7	41,3	39,3	37,8	46	47,1	1,033	0	1,033	0
C3	47,2	44,8	43,4	42,5	42,2	42,2	47	47,1	1,035	0	1,035	0
C4	43,9	43,0	42,2	39,2	37,6	37,8	44	47,8	1,034	25	1,034	25
C5	35,8	36,1	34,4	36,1	—	33,7	36	40,9	1,032	25	1,032	25
E1	45,1	45,1	46,0	44,3	41,7	34,3	45	38,0	1,047	0	1,047	0
E2	42,8	43,7	43,5	40,8	31,6	33,2	43	42,8	1,045	0	1,045	0
E3	40,0	—	41,3	—	40,8	—	41	37,0	1,040	0	1,040	0
E4	42,5	—	44,0	—	40,8	—	43	38,3	1,046	0	1,046	0
E5	42,2	42,2	44,0	41,3	40,8	37,0	42	40,2	1,044	0	1,044	0
F1	49,7	43,2	46,3	43,2	39,5	40,1	43	41,2	1,029	25	1,037	375
F2	35,5	34,0	36,0	37,9	37,6	37,0	38	40,4	1,017	25	1,051	400
F3	43,8	41,9	41,6	42,2	41,6	41,3	42	36,0	1,021	25	1,047	400
F4	43,2	45,3	44,7	45,3	44,7	44,7	45	41,0	1,009	325	1,075	450
F5	43,2	43,2	42,2	41,6	40,7	40,7	42	36,3	1,020	25	1,047	400
G1.1	44,6	44,6	44,4	40,6	40,3	39,4	42	39,8	1,010	100	1,096	500
G1.2[b]	50,0	42,0	47,0	45,5	48,5	46,5	47	45,4	1,025	50	1,077	500
G1.3	38,5	38,5	38,5	38,5	37,5	37,8	39	37,5	1,017	50	1,090	500
G1.4	27,7	27,4	27,7	30,0	29,7	28,2	28	23,1	1,013	75	1,096	500
G1.5[a]	41,0	41,0	42,2	41,0	38,2	41,0	41	38,5	1,012	100	1,096	500
G2.1	53,9	54,2	49,0	54,9	51,5	48,4	49	56,5	1,012	100	1,052	450
G2.2	49,8	46,6	46,6	46,6	46,0	47,5	47	54,4	1,026	50	1,037	450
G3.1	43,7	43,7	45,1	43,7	45,1	40,7	45	52,4	1,026	50	1,036	450
G3.2	53,9	52,4	49,8	55,6	57,1	53,0	54	51,2	1,027	50	1,036	450
G3.3	35,7	—	—	37,9	—	32,7	37	54,9	1,023	50	1,042	450

[a] Temperature rise at 600°C
[b] Temperature rise at 450°C
[c] Distance from bottom of fuel stack

Table 11: Dimensional results of the posttest examinations

Test	Rupture opening				Balloon		Maximum rod bending		Rod	Pellet
	Elevation of midplane	Length	Max. width	Orientation to min. wall thickness [b]	Eccentri-city	Orientation to rupture [b]	Elevation	Max. bending	length change	stack reduction
	mm [a]	mm	mm	degrees	mm	degrees	mm [a]	mm	%	mm
A 1.1	40	19	1,3	72	—	—	—	—	1,11	—
A 1.2	—	—	—	—	—	—	—	—	0,93	—
A 2.1	237	35	9,0	120	0,1	130	270	1,28	0,19	—
A 2.2	145	50	5,5	24	0,1	165	300	3,00	0,04	—
A 2.3	144	19	4,5	63	0,4	145	450	1,10	1,43	—
B 1.1	290	41	9,5	6	0,1	140	130	1,80	0,63	—
B 1.2	338	11	1,8	60	0,3	0	450	1,80	0,89	—
B 1.3	280	36	8,5	63	0,0	—	210	1,08	—	—
B 1.4	—	—	—	—	—	—	—	—	—	—
B 1.5	159	45	3,9	130	0,2	90	420	2,40	0,78	—
B 1.6	290	28	9,5	10	0,5	150	190	1,00	0,17	—
B 1.7	258	49	9,6	45	0,4	159	500	1,72	0,26	—
B 3.1	239	27	9,8	117	0,2	140	170	1,42	0,53	—
B 3.2	242	33	8,2	40	0,2	168	150	1,74	0,77	—
C 1	168	31	6,9	57	0,3	165	470	2,20	0,74	44
C 2	90	25	7,6	63	0,4	165	460	1,95	0,90	16
C 3	158	33	10,5	49	1,3	175	130	2,50	-0,38	39
C 4	186	42	9,0	165	0,4	170	280	1,90	0,08	58
C 5	70	18	2,1	104	0,2	8	480	3,70	1,52	34
E 1	170	13	3,4	24	0,4	47	390	3,10	1,28	22
E 2	130	17	7,5	7	1,3	175	350	5,40	0,0	22
E 3	315	14	6,0	94	0,2	40	380	2,72	0,80	15
E 4	112	31	4,3	8	1,0	135	400	3,10	-0,24	49
E 5	65	6	~ 0,1	50	0,3	18	430	5,10	0,38	82
F 1	342	62	6,1	7	1,0	175	390	3,40	-0,20	83
F 2	410	14	2,6	71	0,1	15	460	1,90	0,40	17
F 3	331	20	6,0	93	0,3	130	360	1,80	0,70	22
F 4	324	28	9,0	35	0,7	175	350	4,60	0,62	29
F 5	325	31	8,0	53	0,5	167	360	1,50	0,12	48
G 1.1	—	—	—	—	—	—	450	1,30	0,80	1
G 1.2	299	4	0,4	42	0,2	2	500	1,70	0,70	3
G 1.3	322	27	2,6	98	0,2	136	490	1,40	0,92	62
G 1.4	317	25	10,0	31	0,6	153	340	2,30	0,14	14
G 1.5	347	44	7,2	108	0,0	0	400	2,30	—	45
G 2.1	445	6	1,5	136	0,2	127	470	1,70	0,58	6
G 2.2	279	33	10,9	10	0,2	152	220	1,30	0,12	36
G 3.1	281	29	7,2	156	0,6	180	260	1,80	1,06	35
G 3.2	212	39	9,7	126	0,3	180	190	1,70	—	67
G 3.3	298	27	11,0	48	0,6	154	270	2,40	0,08	28
BSS12	259	42	8,5	—	0,8	175	490	3,20	—	—
BSS21	—	—	—	—	—	—	—	—	—	—
BSS22 [c]	219	13	0,8	12	0,5	160	250	1,80	—	—
BSS23	295	23	7,8	40	0,5	176	500	1,00	—	—
BSS24	285	14	3,2	163	0,3	160	340	2,30	—	—
BSS25	266	33	9,6	144	0,3	165	200	2,50	—	—
BSS26	204	28	9,0	60	0,4	130	470	3,60	—	—
BSS28	192	8	1,2	50	1,2	10	350	2,40	—	—

[a] Distance from bottom of fuel stack
[b] Smallest angle
[c] Rupture "A"

Table 12: Circumferential elongation of the ruptured regions and vicinity

Test	Rupture opening		Circumferential elongation															
			at max. elongation		in the ruptured region										close to the ruptured region			
	Elevation of midplane	Length	ε	Distance from rupture midplane	ε	Elevation	ε	Elevation	ε	Elevation	ε	Elevation	ε	Elevation	lower end	upper end	ε	Elevation	ε	Elevation
	mm (a)	mm	%	mm	%	mm (a)	%	mm (a)	%	mm (a)	%	mm (a)	%	mm (a)	%	%	%	mm (a)	%	mm (a)
A1.1	40	19	64,0	—	—	—	—	—	—	—	—	—	—	—	53,0	53,0	—	—	—	—
A1.2	—	—	—	—	—	—	—	—	—	—	—	—	—	—	—	—	—	—	—	—
A2.1	237	35	36,2	+ 2,9	31,8	249	23,3	196[b]	23,8	199[b]	25,4	278[b]	—	—	34,0	31,5	33,5	216	31,0	258
A2.2	145	50	56,3	+ 5,6	54,6	154	51,0	168	—	—	—	—	—	—	45,0	50,0	—	—	—	—
A2.3	144	19	34,7	+ 2,4	33,2	134	—	—	—	—	—	—	—	—	33,2	28,0	—	—	—	—
B1.1	290	41	29,0	+ 1,0	29,0	289	28,4	292	27,5	293	24,5	309	—	—	25,5	23,5	—	—	—	—
B1.2	338	11	25,7	- 6,0	24,0	338	21,3	339	23,2	340	20,4	341	—	—	25,7	23,4	19,9	330	—	—
B1.3	280	36	34,2	+ 1,0	26,5	251	32,1	296	—	—	—	—	—	—	29,0	31,0	—	—	—	—
B1.4	—	—	—	—	—	—	—	—	—	—	—	—	—	—	—	—	—	—	—	—
B1.5	159	45	60,4	- 22,1	58,6	165	57,4	167	59,2	168	—	—	—	—	59,0	47,5	58,0	136	45,1	183
B1.6	290	28	38,0	+ 2,5	37,4	302	—	—	—	—	—	—	—	—	32,5	35,0	27,5	269	30,8	309
B1.7	258	49	34,1	+ 2,0	30,9	239	32,4	241	32,4	263	—	—	—	—	30,0	25,0	28,5	230	24,0	285
B3.1	239	27	36,9	+ 0,1	30,3	230	36,9	237	33,6	251	—	—	—	—	29,0	32,0	28,3	219	26,9	256
B3.2	242	33	49,9	+ 0,3	48,1	245	39,2	251	36,2	256	—	—	—	—	37,5	33,5	33,4	222	32,5	261
C1	168	31	51,2	+ 1,5	38,5	153	41,1	156	50,3	170	—	—	—	—	38,5	37,0	31,3	149	32,3	188
C2	90	25	38,8	- 4,0	35,2	78	37,0	81	37,3	88	—	—	—	—	35,2	28,0	27,1	74	25,8	107
C3	158	33	36,7	- 2,0	36,4	159	—	—	—	—	—	—	—	—	32,5	31,0	28,6	136	28,4	177
C4	186	42	44,4	+ 1,0	42,7	190	—	—	—	—	—	—	—	—	38,0	38,0	35,4	160	36,5	210
C5	70	18	62,2	+ 2,3	61,3	69	—	—	—	—	—	—	—	—	52,0	56,0	52,0	60	55,7	79
E1	170	13	30,4	- 1,0	—	—	—	—	—	—	—	—	—	—	29,5	26,0	29,0	162	23,8	179
E2	130	17	46,0	+ 1,0	—	—	—	—	—	—	—	—	—	—	37,0	41,0	27,2	116	30,1	146
E3	315	14	30,9	+ 6,0	28,2	315	—	—	—	—	—	—	—	—	18,0	30,0	16,0	304	25,0	325
E4	112	31	55,5	+ 2,0	—	—	—	—	—	—	—	—	—	—	34,0	43,0	31,6	93	39,2	131
E5	65	6	67,4[c]	+ 24,0	66,4	134[b]	—	—	—	—	—	—	—	—	67,0	67,0	63,3	44	67,4	89
F1	342	62	59,0	- 19,4	52,9	333	48,4	347	44,9	350	37,2	361	36,0	364	56,0	34,0	55,9	311	33.1	374
F2	410	14	37,5	+ 2,0	34,9	404	33,4	406	35,8	409	36,6	411	36,6	414	33,0	32,5	27,4	399	28,9	421
F3	331	20	27,3	+ 2,5	23,7	321	21,9	323	23,7	326	26,1	336	25,5	339	23,7	26,1	16.5	316	18,2	345
F4	324	28	34,1	+ 3,6	26,7	310	25,8	312	34,1	337	—	—	—	—	26,7	34,1	—	—	—	—
F5	325	31	41,2	+ 4,5	35,3	308	38,3	317	40,6	330	38,9	340	—	—	35,3	38,9	29,9	305	31,9	344
G1.1	—	—	—	—	—	—	—	—	—	—	—	—	—	—	—	—	—	—	—	—
G1.2	299	4	29,5	- 2,3	28,3	299	27,4	300	—	—	—	—	—	—	29,0	27,4	29,5	297	26,1	301
G1.3	322	27	62,3	+ 3,6	46,9	308	62,3	337	—	—	—	—	—	—	46,9	62,3	38,1	304	58,2	340
G1.4	317	25	32,6	+ 1,5	32,3	305	29,4	323	—	—	—	—	—	—	32,3	27,5	26,4	297	25,8	335
G1.5	347	44	40,8	- 5,0	39,1	339	37,0	345	37,6	346	34,3	351	33,2	362	37,3	37,0	32,3	321	35,2	373
G2.1	445	6	31,7	+ 3,1	26,1	446	29,6	450	27,0	452	—	—	—	—	22,0	31,7	13,0	437	24,6	452
G2.2	279	33	28,3	+ 1,3	27,4	278	22,1	293	27,1	295	—	—	—	—	25,0	27,1	23,1	259	23,8	299
G3.1	281	29	45,7	+ 4,0	32,4	267	35,1	270	43,7	283	—	—	—	—	32,4	38,0	26,6	262	33,9	300
G3.2	212	39	41,4	+ 11,0	32,2	193	33,6	197	38,1	212	—	—	—	—	32,2	40,5	31,4	189	40,1	235
G3.3	298	27	32,4	+ 1,2	31,8	285	24,4	287	32,1	302	—	—	—	—	31,8	28,0	26,2	279	27,0	316
BSS12	259	42	35,3	+ 3,0	35,0	238	34,4	240	35,0	264	35,3	278	34,1	280	35,0	34,1	30,5	235	31,9	283
BSS21	—	—	—	—	—	—	—	—	—	—	—	—	—	—	—	—	—	—	—	—
BSS22	219	13	63,8[c]	- 49,0	61,7	204	56,1	219	53,1	222	61,1	164	57,2	162	60,0	52,4	60,2	212	52,2	226
BSS23	293	23	40,1	0,0	—	—	—	—	—	—	—	—	—	—	32,0	33,0	26,7	276	30,0	310
BSS24	285	14	30,3	- 1,0	—	—	—	—	—	—	—	—	—	—	24,0	25,0	21,0	275	17,9	296
BSS25	266	33	28,5	- 2,0	27,9	267	—	—	—	—	—	—	—	—	25,5	25,0	23,8	244	24,2	286
BSS26	204	28	41,9[c]	+ 76,0	36,5	205	36,8	208	29,4	223	—	—	—	—	29,0	33,0	27,0	186	30,4	223
BSS28	192	8	34,4	- 1,0	—	—	—	—	—	—	—	—	—	—	31,5	30,0	30,0	187	28,6	198

(a) Distance from bottom of fuel stack

b) from polar profile

c) outside the ruptured zone

Table 13: Results of sieve analyses

sieve size (mm)	C (2.500 MWd/t_u) retainings weight (g)	weight fraction (%)	cumulative weight % finer than	E (8.000 MWd/t_u) retainings weight (g)	weight fraction (%)	cumulative weight % finer than	F (20.000 MWd/t_u) retainings weight (g)	weight fraction (%)	cumulative weight % finer than
<0,1	—	—	—	—	—	—	0,158	0,15	
0,1	0,296*	0,15	—	0,997*	0,35	—	0,363	0,35	0,15
0,315	1,135	0,56	0,15	1,914	0,67	0,35	1,912	1,84	0,50
1	2,704	1,34	0,71	9,181	3,19	1,01	9,435	9,09	2,34
2	49.584	24,54	2,04	75,154	26,13	4,20	47,853	46,11	11,43
3,15	91,148	45,07	26,56	141,824	49,31	30,34	39,067	37,64	57,54
4	48,543	24,00	71,63	51,931	18,06	79,65	5,002	4,82	95,18
5	8,820	4,36	95,64	6,602	2,30	97,71	—	—	—
total	202,230	100,00		287,603	100,00		103,790	100,00	

* < 0,315

sieve size (mm)	G1 (35.000 MWd/t_u) retainings weight (g)	weight fraction (%)	cumulative weight % finer than	G2/3 (35.000 MWd/t_u) retainings weight (g)	weight fraction (%)	cumulative weight % finer than
<0,1	0,375	0,12	—	0,493	0,17	—
0,1	0,982	0,32	0,12	1,273	0,44	0,17
0,315	6,308	2,06	0,44	5,260	1,81	0,61
1	21,004	6,86	2,50	17,627	6,08	2,42
2	82,126	26,84	9,36	121,340	41,80	8,50
3,15	138,413	51,76	36,20	120,404	41,54	50,30
4	36,817	12,03	87,96	23,484	8,10	91,84
5	—	—	—	—	—	—
total	306,025	100,00		289,881	100,00	

Table 14: Evaluation of the specific fuel mass data from sieve analyses

Test	Sample			Fuel mass per unit				Mean particle size
	No.	weight	length	mean cladding circ.elongation	(prior) length [a]	(after transient) length	area [b]	volume [c]	
—	—	g	cm	%	g/cm	g/cm	g/cm²	g/cm³	mm
C1	2	23,402	3,3	21,9	6,63	7,09	1,72	6,34	3,39
	6	28,710	3.7	20,9		7,76	1,9	7,07	3,44
C2	8	25,071	3,9	9,8	6,63	6,43	1,73	7,44	3,25
C3	1	25,397	3,8	16,5	6,63	6,68	1,70	6,67	2,91
C4	1	28,724	3,95	24,6	6,63	7,27	1,73	6,16	3,06
C5	1	23,572	3,9	10,7	6,63	6,09	1,61	6,81	3,04
C6	24	33,985	5,35	0	6,63	6,35	1,88	9,33	3,08
	25	13,372	2,02	0		6,62	1,96	9,69	2,78
E1	1	26,406	3,8	11,6	6,62	6,95	1,84	7,70	3,09
E2	1	26,961	3,98	11,4	6,62	6,77	1,80	7,58	2,79
E3	1	25,009	3,72	13,75	6,62	6,723	1,75	7,15	3,5
E4	1	28,527	3,99	24,01	6,62	7,15	1,71	6,16	2,94
	4	24,684	3,29	10,7		7,503	2,01	8,48	3,03
E5	6	51,395	5,05	48	6,61	10,18	2,03	5,74	2,96
	8	65,456	4,45	67,5		14,71	2,60	6,36	2,87
E6	8	18,403	2,9	0	6,63	6,35	1,88	9,34	2,85
	9	20,762	3,1	0		6,697	1,98	9,84	2,54
F1	—				6,62				
F2	—				6,62				
F3	—				6,63				
F4	5	22,010	3,04	16,7	6,63	7,24	1,83	7,18	2,45
	6	18,802	3,04	10,7	6,63	6,18	1,65	6,99	2,39
F5	2	18,970	3,22	20,9	6,63	5,89	1,44	5,36	2,54
	7	18,074	3,0	18,6	6,63	6,02	1,50	5,75	2,69
F6	15	6,621	1,01	0	6,63	6,56	1,94	9,64	2,22 [d]
	24	7,059	1,11	0	6,63	6,36	1,88	9,36	1,82 [d]
	25	12,283	1,91	0	6,63	6,43	1,90	9,46	2,09 [d]
G1.1	2	21,708	3,2	1,7	6,68	6,79	1,98	9,56	2,75
	4	20,315	3,15	1,6	6,68	6,45	1,88	9,11	2,71
G1.2	2	37,466	—			[e]			
	5	23,983	3,9	5,6	6,67	6,15	1,72	7,85	2,63
G1.3	2	—			[f]				
	7	20,553	3,05	13,3	6,7	6,74	1,76	7,19	2,63
G1.4	2	26,462	4,02	13,9	6,7	6,58	1,71	6,92	2,63
	6	23,989	4,04	5,5	6,7	5,94	1,67	7,60	2,82
G1.5	8	18,682	3,1	6,7	6,69	6,03	1,67	7,49	2,7
	2	113,041	18,7	25,9	6,69	6,05	1,42	5,27	2,77
G1.6	11	18,441	2,9	0	6,7	6,36	1,88	9,37	2,7
	22	18,851	2,9	0	6,7	6,50	1,93	9,58	2,7
G2.1	2	27,009	4	9,8	6,62	6,76	1,82	7,81	2,41
	4	26,643	4	4,2	6,62	6,66	1,89	8,8	2,39
G2.2	2	25,914	4,05	19,1	6,62	6,4	1,59	6,04	2,48
	6	25,799	4,04	8,8	6,62	6,39	1,74	7,54	2,43
G3.1	2	28,258	3,94	23,3	6,69	7,17	1,72	6,23	2,60
	6	22,301	4,04	12,8	6,69	7,01	1,84	7,56	2,76
G3.2	2	28,561	3,98	28,8	6,68	7,18	1,65	5,62	2,48
	6	30,801	4,03	16,3	6,68	7,64	1,95	7,65	2,92
G3.3	7	25,777	3,6	8,8	6,70	7,16	1,95	8,51	2,69
	8	7,84	1,14	7	6,70	6,88	1,90	8,49	2,49
G3.6	11	18,894	2,9	0	6,69	6,52	1,93	9,64	2,43
	22	22,087	3,33	0	6,69	6,63	1,97	9,77	2,25

[a] As-fabricated

[b] Outside area of cladding

[c] Inner volume of cladding

[d] 1,5 min sieving time (instead of 3 min for other samples)

[e] Not evaluated, loss of fuel during handling

[f] Not evaluated, portions of end pellet in sample

Table 15: Comparison of the maximum cladding temperatures evaluated from thermocouple measurement and zircaloy micro-structure evaluation at the location of the burst tip.

Test	Cladding microstructure at the burst tip		Thermocouple measurement	
	$T_{max.}$ [°C]	$\Delta T_{azimuth., max.}$ [K]	$T_{max.}$ [°C]	extrapol./interpol.
A1.1		—	900	extrapol.
A2.1	820-860	0	900	extrapol.
A2.2	850-890	45	920	extrapol.
A2.3	890-920	20	1020	extrapol.
B1.1	830-880	20	900	interpol.
B1.2	~ 890	40	1000	interpol.
B1.3	820-860	5	905	interpol.
B1.5	840-900	0	930	extrapol.
B1.6	780-820	0	860	interpol.
B3.1	800-860	0	890	interpol.
B3.2	800-860	5	920	interpol.
C1	860-900	10	1020	extrapol.
C2	930-960	0	945	extrapol.
C3	< 800	?	760	extrapol.
C4	860-890	30	917	extrapol.
C5	880-910	20	916	extrapol.
E1	930-960	80	930	extrapol.
E2	880-920	50	970	extrapol.
E3	950-980	50	960	interpol.
E4	930-960	60	1000	extrapol.
E5	950-980	20	930	extrapol.
F1	850-900	50	960	interpol.
F2	850-900	50	970	interpol.
F3	830-880	60	940	interpol.
F4	810-860	25	975	interpol.
F5	800-860	0	950	interpol.
G1.1	—	—	—	
G1.2	880-910	10	920	interpol.
G1.3	840-890	35	940	interpol.
G1.4	800-840	20	910	interpol.
G1.5	860-900	15	850	interpol.
G2.1	940-970	40	900	interpol.
G2.2	800-850	30	890	interpol.
G3.1	850-900	30	900	interpol.
G3.2	840-870	20	840	interpol.
G3.3	850-900	0	930	interpol.
BSS12	860-910	100	850	interpol.
BSS22	860-900	55	860	interpol.
BSS23	—	—	840	interpol.
BSS24	—	—	960	interpol.
BSS25	810-850	60	820	interpol.
BSS26	840-900	50	880	interpol.
BSS28	910-940	60	1000	interpol.

Appendix B

Overall Views of Transverse Metallographic Samples

Test A1.1

Test A 2.1

Test A 2.2

Test A 2.3

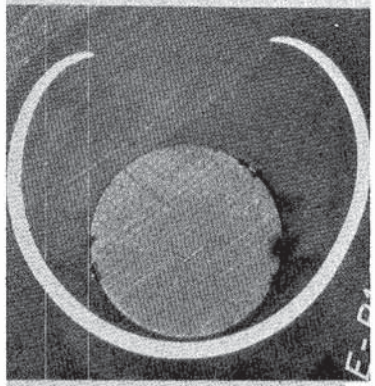

Test B1.1

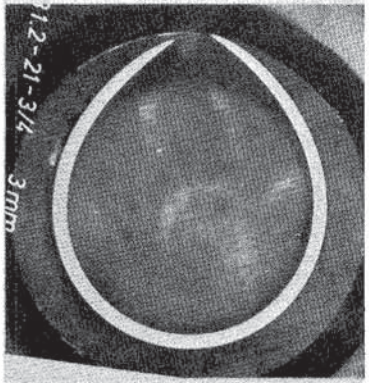

Test B1.2

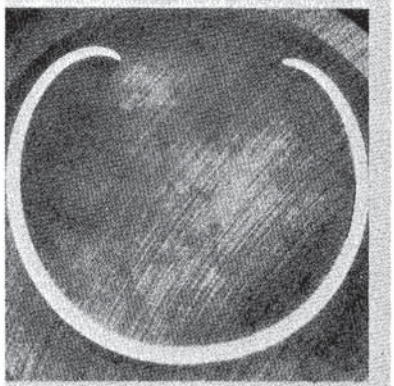

Test B1.3

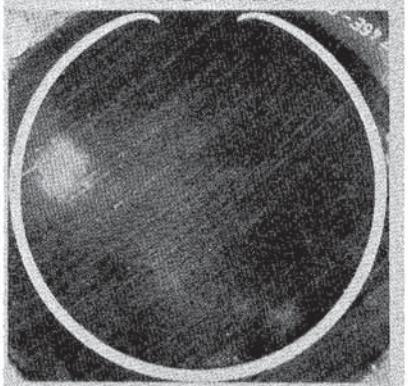

Test B1.5

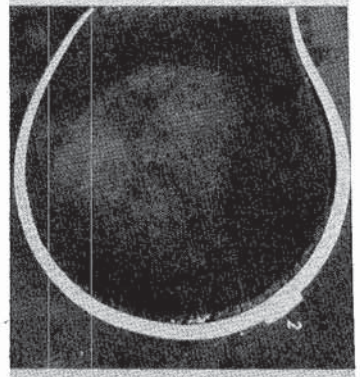

Test B1.6

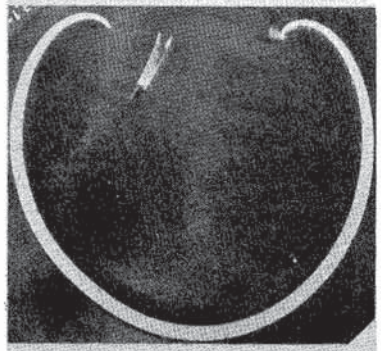

Test B3.1

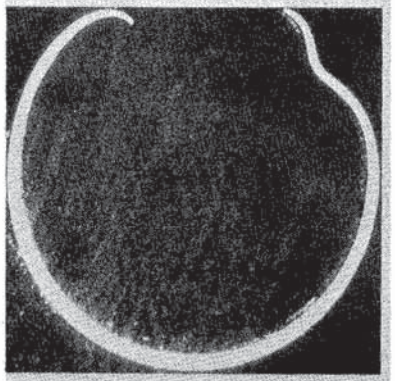

Test B3.2

Inpile Tests in FR2

Cross Sections of the A- and B-Test Rods (Unirradiated)

IT - 1980
PNS 4237-253

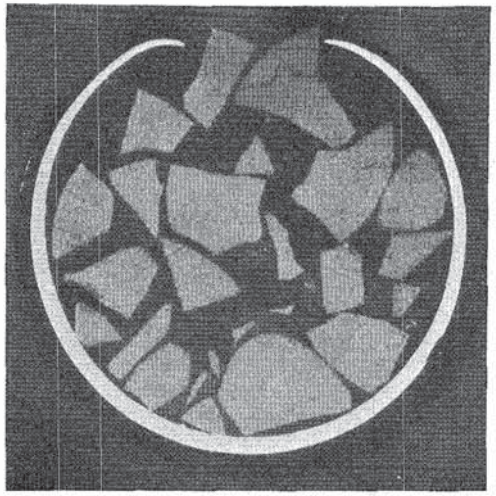

Test C1

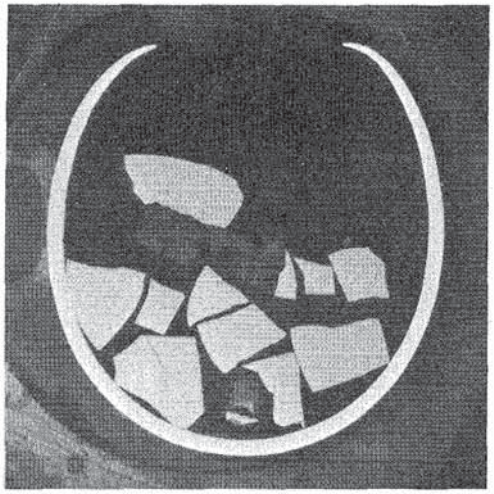

Test C2

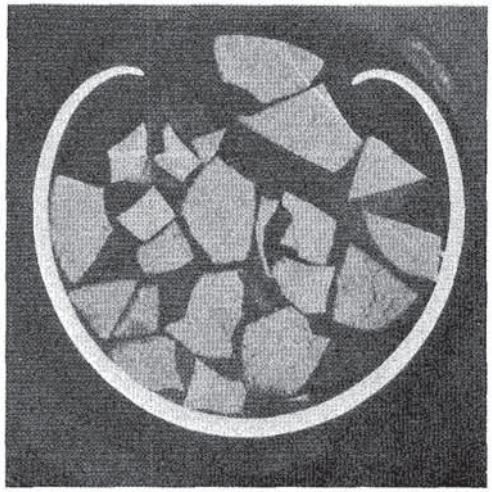

Test C3

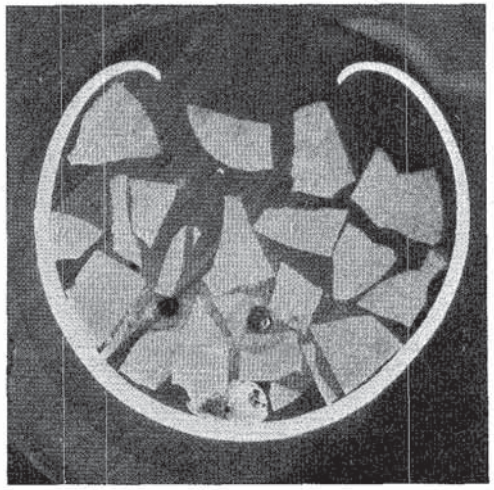

Test C4

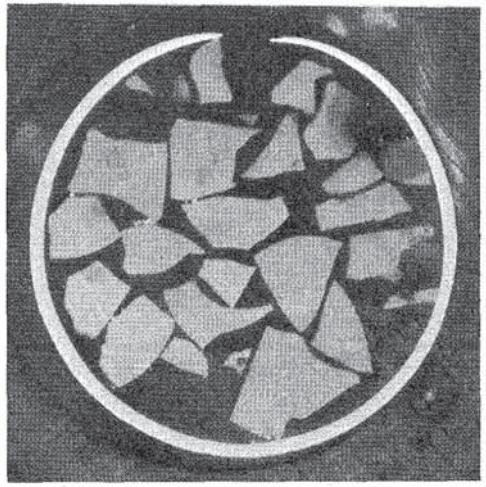

Test C5

FR 2 In-Pile Tests

Cross Sections of the
Test Rods from Series C
(2 500 MWd/t Burnup)

IT 1981
PNS 4237-648

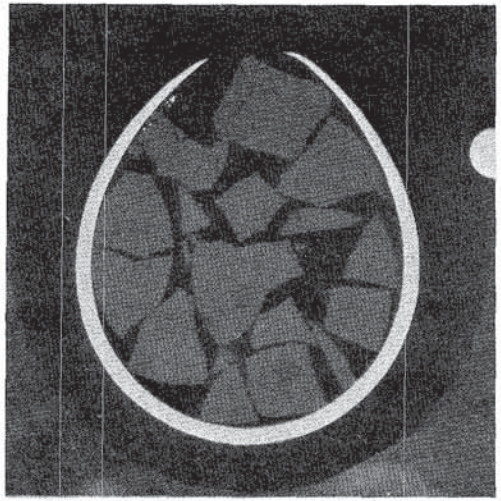

Test E1

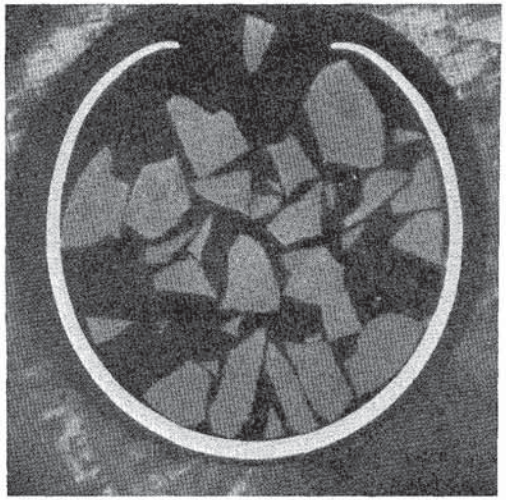

Test E2

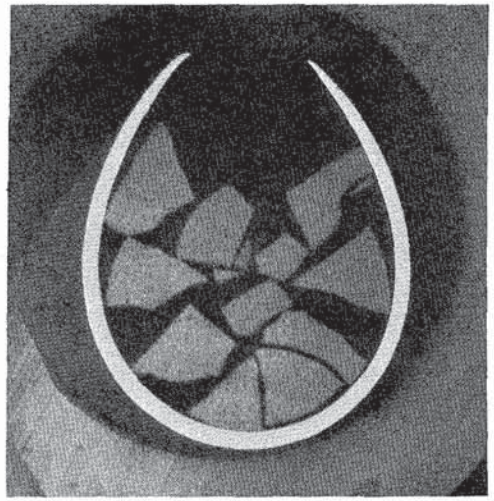

Test E3

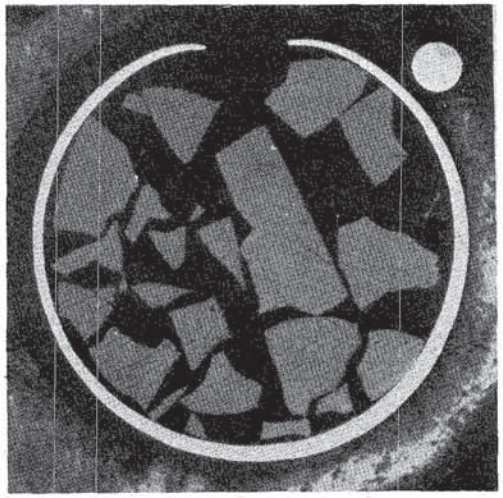

Test E4

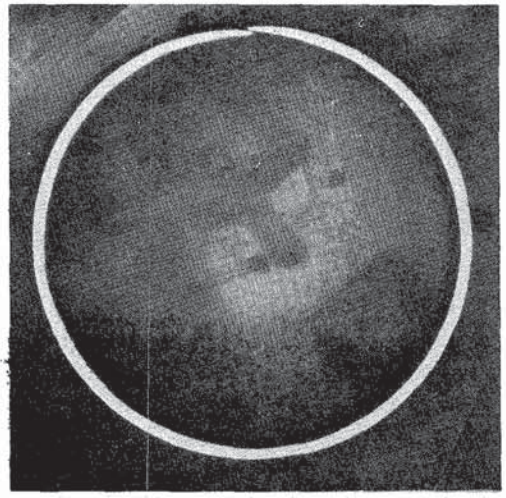

Test E5

FR 2 In-Pile Tests

Cross Sections of the
Test Rods from Series E
(8000 MWd/t Burnup)

4237-706

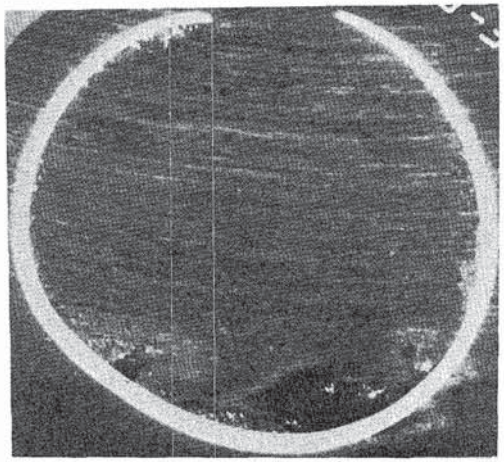

Test F 1

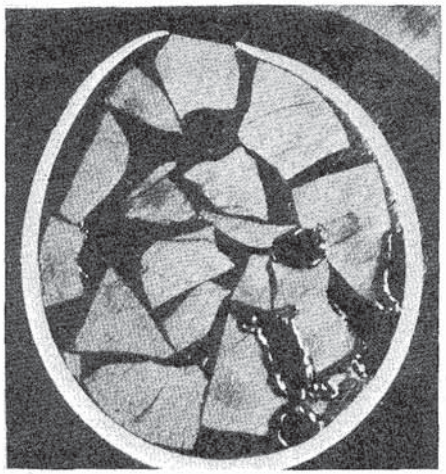

Test F 2

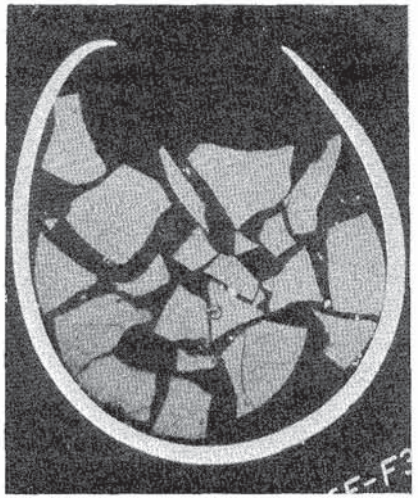

Test F 3

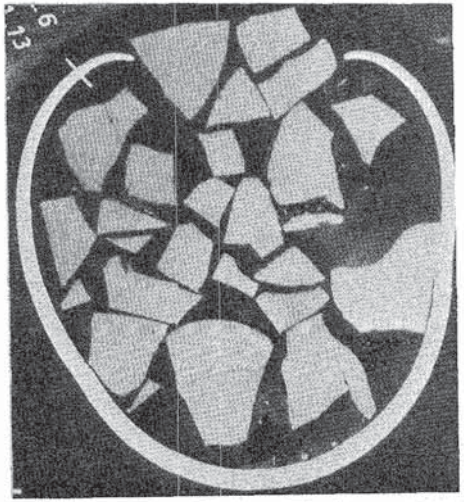

Test F 4

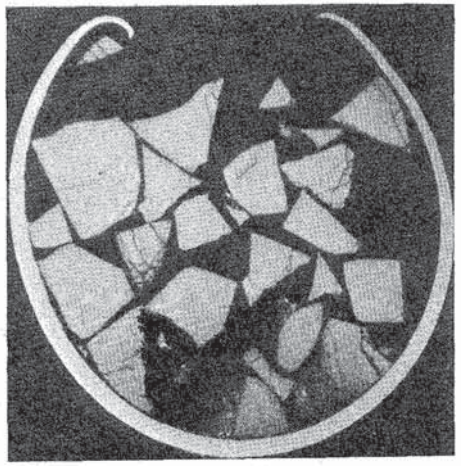

Test F 5

FR2 In-Pile Tests.

Cross Sections of the Test Rods Series F (20000MWd/t Burnup)

IT-80
PNS4237-357

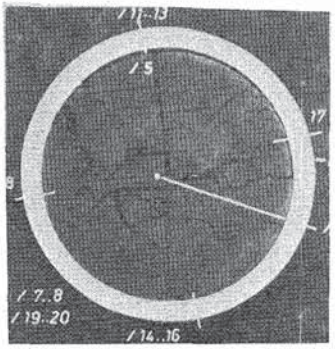

Test G1.1
(No Burst)

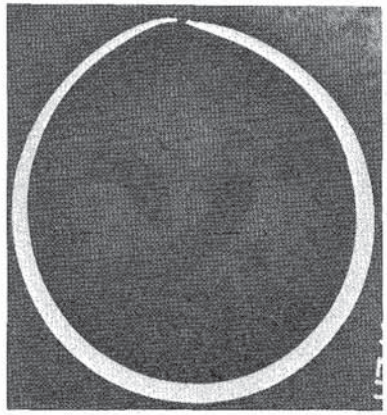

Test G1.2

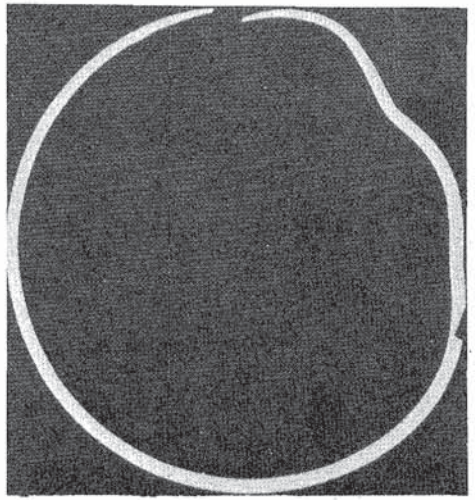

Test G1.3

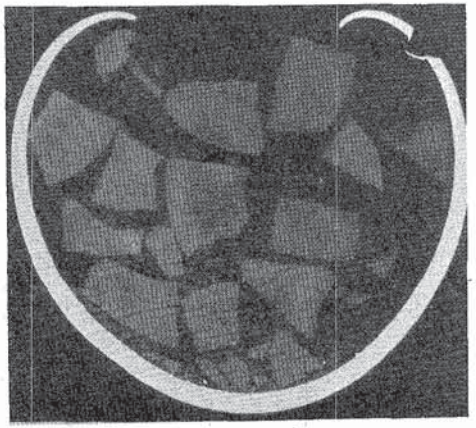

Test G1.4

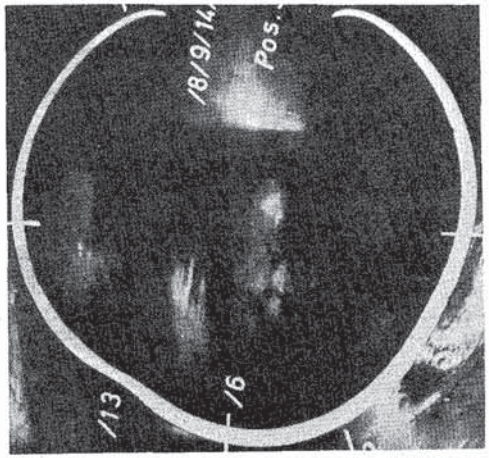

Test G1.5

FR2 In-Pile Tests.

Cross Sections of the Test Rods Series G1 (35 000MWd/t Burnup)

IT-80
PNS4237-358

FR 2 In-Pile Tests

Cross Sections of the Test Rods, Series G 2 / G 3 (35 000 MWd/t Burnup)

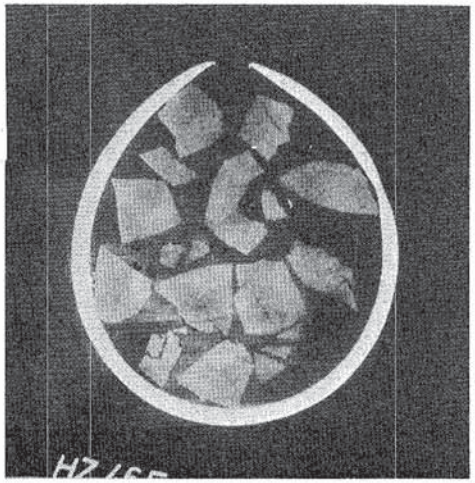

Test G 2.1

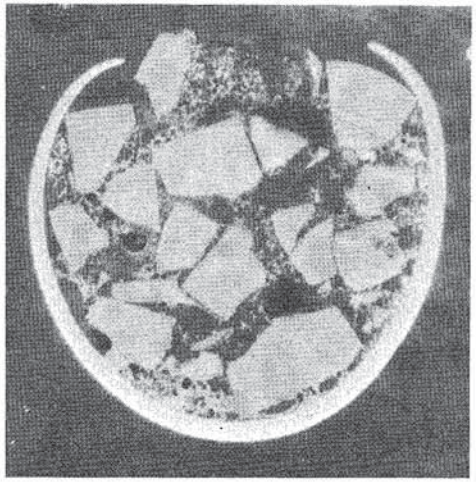

Test G 2.2

Test G 3.1

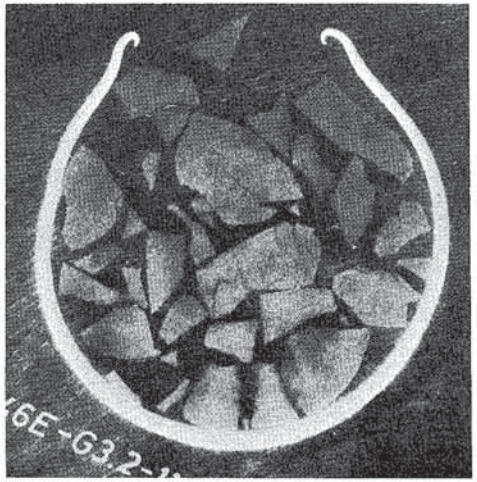

Test G 3.2

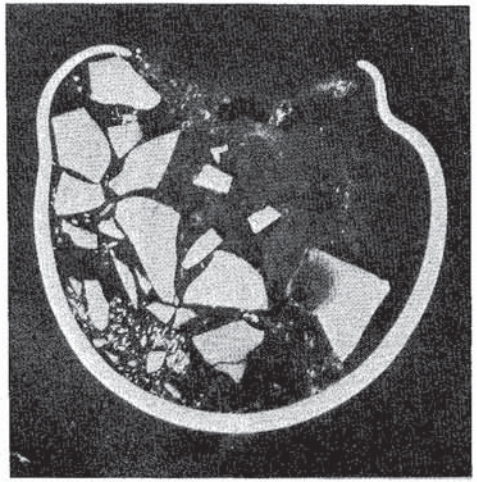

Test G 3.3

IT 1980
PNS 4237-397

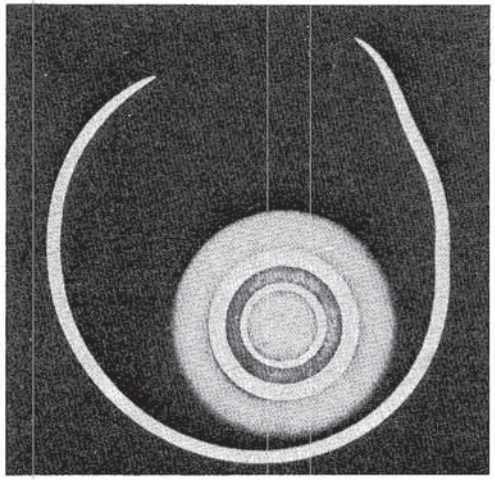

Test BSS 12

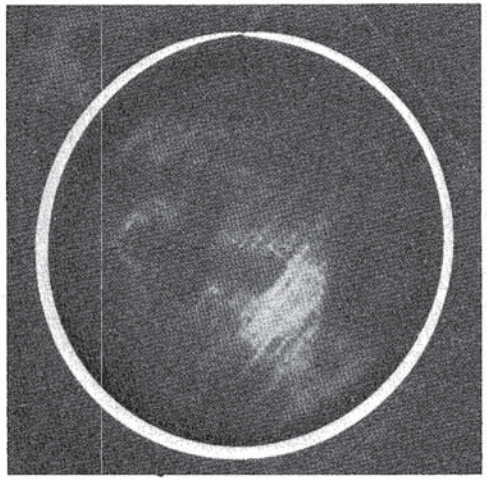

Test BSS 22

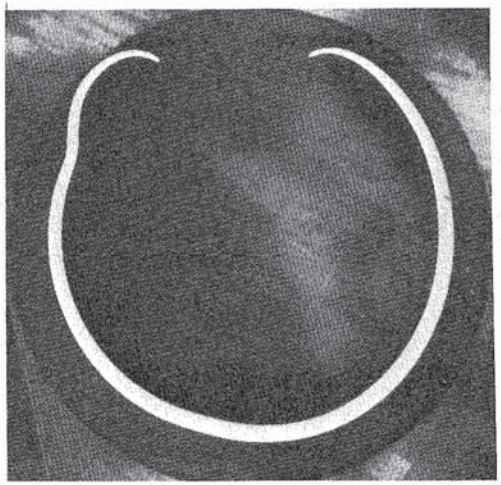

Test BSS 23

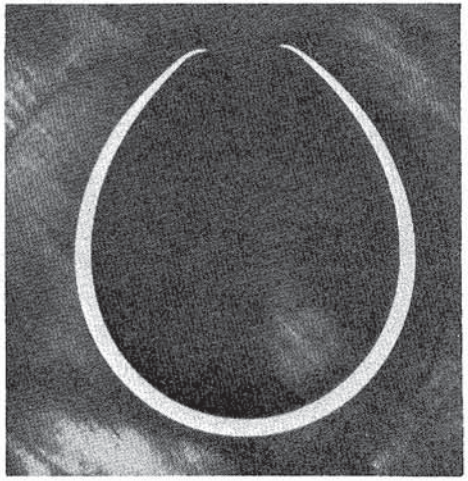

Test BSS 24

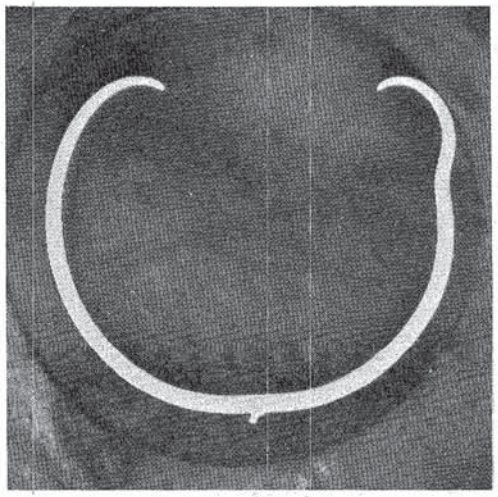

Test BSS 25

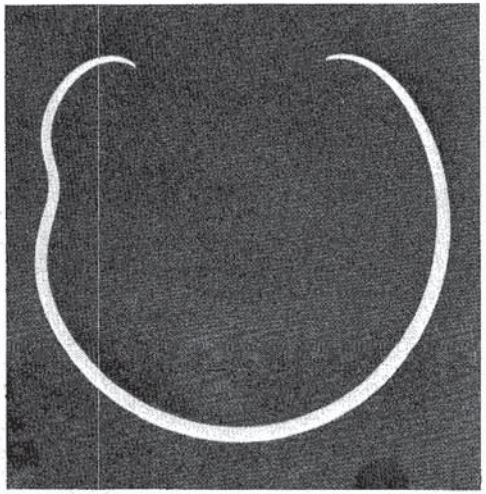

Test BSS 26

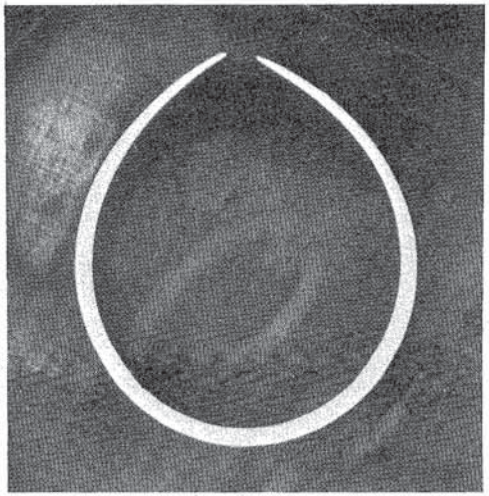

Test BSS 28

FR 2 In-Pile Tests

Cross Sections of the
Test Rods from Series BSS
(electrical simulators)

4237-697

Appendix C

Uncertainties of Cladding Temperature Determination

Appendix C

Uncertainties of Cladding Temperature Determination

C 1. Measurement with Thermocouples

Cladding temperature as a function of time was measured with thermocouples, spot welded onto the cladding surface as described in section 3.3. Usually six thermocouples per test rod were positioned at different axial elevations of the active zone at different azimuthal angles.

C 1.1 Thermocouple response

High quality thermocouples were used with an error tolerance of ± 0,375% (above 400°C) or ± 1,5 K (below 400°C) /13/. The thermal-electric response of each individual thermocouple was checked before it was welded on the cladding. In addition, the electric characteristics were checked after each step during assembling. Thus, the maximum error resulting from the thermocouple properties was below 4 K at 1000°C.

C 1.2 Thermocouple attachment method

A larger source of error was the thermocouple attachment technique. In Version A as well as B (see Fig.5) the thermocouple was in contact with the cladding surface on one side, but exposed the larger fraction of its own surface to the cooler environment. Although there was no forced convection cooling during the transient test, heat conduction and radiation to the shroud, which was 300 to 400 K cooler than the cladding, reduced the thermocouple temperature. In order to evaluate the magnitude of this error, in-pile calibration tests were made with electrically heated fuel rod simulators (BSS), which had a special instrumentation: In the close vicinity of each normal 1 mm O.D. thermocouple - spot-welded to the cladding surface - a second thermocouple of 0,5 mm O.D. was embedded in a groove in the cladding wall.

The readings of these 0,5 mm thermocouples were taken as a good approximation of the real wall temperature. The difference to the readings of the 1 mm O.D. thermocouples was taken as the error caused by the attachment method of the normal thermocouples. As shown in Fig. 6 the error was found to be a function of rod power and was higher for the A version thermocouples than for the B version. For the A version the scatter of the error was rather large. The values of Fig. 6 (mean data) were used as a correction to the thermocouple readings throughout the entire test program, i.e. the thermocouple readings were corrected by the addition of

75 K (± 35 K) for thermocouple version A
10 K (± 10 K) for thermocouple version B

at a linear rod power rate of 40 W/cm for the nuclear rod which corresponded to 50 W/cm for the electrically heated simulator (same heatup rate). It must be noted at this point, that these correction values were determined without deformation of the test rod cladding. When the cladding deforms, the heat flux across the cladding wall changes and this certainly influences the difference between thermocouple readings and true wall temperature, though probably towards smaller corrections.

C 1.3 Determination of burst temperature

Determination of the burst temperature of a rod contains an additional problem. The burst temperature was defined to be the cladding temperature at the time of burst at the location of rupture (= axial center of the rupture opening). This location was generally not at a position where a thermocouple was attached, but was axially and azimuthally displaced. Burst temperature was - in this case - determined by linear interpolation from the readings of the two thermocouples closest to the rupture, or by extrapolation according to the general axial power profile. Although this method is regarded as the best approximation, it raised another source of error:

The two thermocouples used for inter- or extrapolation and the location of the wanted burst temperature were in most cases at three different azimuthal angles. If there are azimuthal temperature variations in the cross-section planes of the thermocouples and of the burst location, then the inter-/extrapolation may lead to an incorrect burst temperature.

There is no systematic procedure to determine the magnitude and direction of this error in any individual case, as there is no information available about the azimuthal temperature distributions at the moment of burst.

The error will not exceed the value of the azimuthal variation in one plane and will - in many cases - be much lower or even zero. Taking the variations determined from the microstructure (see section 6.1) for the moment of maximum temperature as an estimate we can state, that the error may be as high as 80 K in some cases, but in the average probably smaller than 30 K. These numbers are for rods with nuclear fuel. The pertinent data for electrically heated simulators are 100 K maximum and 65 K average.

C 2 Evaluation of Zircaloy microstructure

C 2.1 General

As reported in Section 6.1 the local maximum cladding temperature, reached during the test, was estimated by evaluating the appearance of the post-test Zry microstructure. This was done for each transient tested rod at various locations, of which two groups are of special interest:

a) Locations close to thermocouple welds, for direct comparison of the microstructure method with thermocouple measurement, and
b) rupture locations, where the burst temperature was to be determined.

The temperatures determined from the microstructure are judged to be reliable within about ± 30 K for the low ($\alpha + \beta$)-phase temperature range and within about ± 15 K of uncertainty for the high ($\alpha + \beta$)-phase range, where the microstructure is most temperature sensitive (section 6.1).

C 2.2 Location of thermocouple welds

The comparison of the maximum temperatures from microstructure with the temperatures measured with thermocouples and corrected, gave the following results for location (a), positions close to thermocouples:

Thermocouple attachment version A:
Temperatures T from microstructure were generally lower than thermocouple measured temperatures Θ. The difference
$\Delta = \Theta - T$ averaged over all samples gives
$\overline{\Delta}_A = 44$ K

Thermocouple attachment version B:
Temperatures T were generally higher than Θ
$\overline{\Delta}_B = -24$ K

If the temperatures from microstructure were correct, these results would mean, that the values used for correcting the thermocouple readings (see C 1.2) were approx. 45 K too high for thermocouple version A and approx. 25 K too low for thermocouple version B. In other words, the thermocouples were to be corrected by adding 30 K for version A and 35 K for version B. This, however, is very unlikely with respect to the different attachment principles and with regard to the results of the calibration tests.

C 2.3. Rupture location

The comparison of the maximum temperatures at the rupture positions (location (b)) looks somewhat different:

Thermocouple version A:

$\overline{\Delta}_A = 80$ K

Thermocouple version B:

$\overline{\Delta}_B = 20$ K

Here, the maximum temperatures T from microstructure were lower than the temperatures derived from TC measurements for both thermocouple versions, and the differences $\Delta = \Theta - T$ were 35 to 45 K larger than at locations (a). This can be explained by the following circumstances: Because of a stronger decoupling between cladding and fuel with increasing deformation, the temperature increase after the burst at the rupture position is smaller than at the positions of the thermocouples. From this it must be concluded that temperature determination via evaluation of microstructure or its combination with the data of thermocouple measurement does not help to increase the accuracy of burst temperature determination. From microstructure we obtained information from the rupture location itself but only on maximum temperature; from thermocouples we got information on the temperature at the time of rupture, but from locations in the vicinity of the rupture only, so that inter- or extrapolation was necessary with all the uncertainties described above.

C 3 Summary

- Temperatures at locations of thermocouple attachment were determined by thermocouple measurement with an uncertainty of

  Δ = 39 K = ±4 ± 35 K (thermocouple version A)

  = 14 K = ±4 ± 10 K (thermocouple version B)

  → contribution of attachment method

  → contribution of thermocouple response

- Burst temperatures were determined by inter- or extrapolation with the following uncertainties:

(1) Nuclear rods:

Thermocouple version A:

$\Delta = \pm$ 69 K (max. 119)

$= \pm 4 \pm 35 \pm 30\ (80)$

- 30 (80) → inter-/extrapolation
- 35 → attachment
- 4 → thermocouple response

Thermocouple version B:

$\Delta = \pm$ 44 K (max. 94)

$= \pm 4 \pm 10 \pm 30\ (80)$

(2) Simulators (only thermocouple version B):

$\Delta = \pm$ 79 K (max. 114)

$= \pm 4 \pm 10 \pm 65\ (100)$

- Temperature estimates by microstructure evaluation and temperatures determined by thermocouple measurement showed differences. In the average, microstructure temperatures were

  44 K lower for thermocouple version A
  24 K higher for thermocouple version B.

- Temperature estimates by microstructure did not reduce uncertainties of burst temperature determination.

Acknowledgments

The authors gratefully appreciate the efforts of Messrs. K. Baumgärtner, G. Harbauer, H. Hespeler, W. Knappschneider, W. Legner, W. Leiling, H. Lukitsch, B. Räpple, A. Scherer, and K. Wagner in the successful performance of the research program.

A special acknowledgment is due to A. Fiege, Nuclear Safety Project Management, for his continuous assistance and support and for providing helpful directives to this research program.

The mechanical behavior of the cladding material was studied by C. Petersen and fission gas and fuel swelling investigations were performed by Dr. H. Zimmermann.

The accompanying calculations on the heatup behavior of the nuclearly and electrically heated rods were done by Dr. D. Steiner, IKE Stuttgart (Stuttgart University). The test loop was operated by R. Kettner and F. Schmitt.

The authors would also like to thank the numerous reactor and hot cell personnel for their contributions in performing the tests and the posttest fuel rod examinations.